VOLUME G - DATA MANAGEMENT ANALYSIS

Table of Contents

SECTION 1 - DATA MANAGEMENT ANALYSIS

g. Data Management Analysis

This data requirement element asks for many items related
spcifically to computer systems within the science instrument.
Since the HRC instrument has no internal computer, these
requirements cannot be addressed. Alternatively, this response
will include a set of analyses and proof of concept test results
which, in combination with other analyses, will give insight into
the quality and stability of the electronic systems which convert
the low level detector analog signals to digital science data in
accordance with the Observatory to Science Instrument Interface
Control Document and the Contract End-Item Specification.

The most complete model of the HRC performance was prepared by K.
Flanagan[1], which describes detector models and error models
(gain, offset, noise, and digitizing errors) through the system.
Additionally, memoranda prepared by J. Gomes[2,3,4] address the
effects of electronic noise, digitization effects, and the
capability for data correction through in-flight calibration.
These documents are appended to this response.

Detailed schematics of the complete electronic systems are
provided in the HRC team CDR response to SSE06, "Schematics,
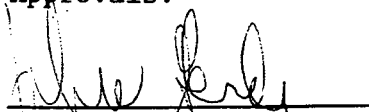Diagrams, and Lists".

[1] Flanagan, K.A. "Modeling of the HRC Readout System", SAO
              Report # SAO-HRC-RPT-92-010, September, 1992.

[2] Gomes, J.   7/29/94 Memorandum "Estimated Hybrid Preamp
              performance w/ low noise plates"

[3] Gomes, J.   4/11/94 Memorandum"Justification for HRC ADC size"

[4] Gomes, J.   3/8/95 Memorandum"On Board Test Pulse Generator

[5] Gomes, J.   10/5/94 Design note : Offset Budget

ADVANCED X-RAY ASTROPHYSICS FACILITY (AXAF)

HIGH RESOLUTION CAMERA (HRC)

Modeling of the HRC Readout System

September 1992

Prepared By: Kathryn Flanagan

Smithsonian Astrophysical Observatory
High Energy Astrophysics Division

Approvals:

John W. Gerdes
Program Manager, HRC

Stephen S. Murray
Principal Investigator, HRC

ADVANCED X-RAY ASTROPHYSICS FACILITY (AXAF) HIGH RESOLUTION CAMERA (HRC)

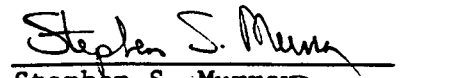## Modeling of the HRC Readout System

September 1992

Prepared By: Kathryn Flanagan

Smithsonian Astrophysical Observatory
High Energy Astrophysics Division

Approvals:

John W. Gerdes
Program Manager, HRC

Stephen S. Murray
Principal Investigator, HRC

ADVANCED X-RAY ASTROPHYSICS FACILITY (AXAF)
HIGH RESOLUTION CAMERA (HRC)

Modeling of the HRC Readout System

September 1992

Smithsonian Institution
Astrophysical Observatory
Cambridge, MA 02138

Contents

1 Introduction

The High Resolution Camera, or HRC, is a microchannel plate detector designed to fly aboard the Advanced X-Ray Astrophysics Facility (AXAF), one of the "Great Observatories" under the auspices of NASA. This instrument, HRC, is the direct descendant of its successful predecessors aboard *Einstein* and ROSAT. The HRC is designed to have 25 μm FWHM resolution or better, and will be used for direct imaging and in combination with transmission gratings for high resolution spectroscopy.

The High Resolution Camera (HRC) consists of two photon counting imaging detectors, one for direct imaging and the other for reading out a transmission grating spectrum. Figure 1 shows a schematic drawing of a detector assembly. The active X-ray detecting element consists of a coated microchannel plate (MCP) and a second MCP for additional electronic gain. X-ray event position, occurrence time, and amplitude are recorded by the Crossed Grid Charge Detector (CGCD). In front of the MCP's, a thin film, the UV/Ion shield, blocks unwanted UV light, low energy electrons, and ions. The HRC has been selected for flight on the Advanced X-Ray Astrophysics Facility (AXAF).

As part of an effort to understand and improve the resolution of the instrument, we have examined in detail the design of the readout system: the crossed grid charge detector (CGCD), and the associated set of preamplifiers and ADCs. The output signals from this readout system are input to a position algorithm to calculate the position of each individual X-ray event. The design parameters of the electronics affect the ultimate resolution of the instrument. By modeling these parameters and their effect on positioning, we formulate design criteria for the electronics that are consistent with the resolution performance goal.

This report is intended to summarize the results of the modeling and their implications on the design criteria for the electronics. Specifically, *the purpose of the present investigation is to establish the sensitivity (with numerical estimates) of the positioning algorithm accuracy to variations in the event processing electronics. In order to do this, there are three parameters (gain, offset and noise) in this model that are independently varied in the preamplifiers and the ADCs.* In order to place this investigation in context, we begin first by discussing the general character of imaging performance (Section 2). Then the detector is described, including the CGCD and processing electronics (Section 3). Next, we discuss the position algorithm and the modeling (Section 4). (The information for Sections 2, 3 and 4 has been obtained, at least in part, from the references listed in Section 7.) Section 5 addresses the results of the modeling, with the derived design criteria given in Table 5. In particular, Section 5.5 summarizes the conclusions of the modeling as applied to the current design. Section 6 summarizes published work giving an analytical estimate of the noise expected with our position algorithm, and measurements (on an HRC prototype) relating to it. Finally, in Section 9, we have included those publications by HRC related to modeling.

This report summarizes the results of the modeling to date, taking as the point of departure the memo dated October 16, 1991. The results of the interim report of February 11, 1992

are included herein and discussed more fully, except for the observations about gaps, which are not treated further. These reports are included for reference in Section 9.

2 Modeling and Imaging Performance

To discuss the particular place of the modeling in understanding the sensitivities of various conditions and parameters in the overall scheme of positioning accuracy, it makes sense to first examine the issue of resolution and image quality and the role of the readout systems electronics. Appendix I contains Figures 2 and 3, and describes the three common characterizations of image quality: spatial resolution, distortion and uniformity of efficiency. We are interested particularly in the resolution, since the other two effects can be calibrated out. As discussed in Appendix I, the resolution is limited by systematic errors, which we can generally correct for, and statistical errors, which we cannot. Systematic terms include the MCP pore structure, non-uniformity of cgcd wires or resistors, etc. Statistical errors include signal variations, thermal noise of the grids, and similar contributions.

The modeling does not attempt to incorporate all contributors to the imaging resolution. It is limited to examining the effects of variations in the event processing electronics. Specifically, the modeling examines the effect of varying the noise, offset and gain of preamps and ADCs on the centroid positioning algorithm. These parameters can affect the positioning in two ways; by imposing an uncertainty (noise) without affecting the centroid, or by shifting the centroid calculated by the positioning algorithm. We are interested in numerically estimating the effects of each of these parameters on the calculated position. More importantly, we wish to identify any that significantly degrade the positioning and whose effect cannot be calibrated out.

3 Detector Description

3.1 General Elements of the Detector

The major elements of the HRC were shown in Figure 1. A CsI-coated MCP at bias angle $0°$ is followed by an uncoated MCP in "chevron" configuration at $13°$. This configuration suppresses ion feedback. A thin window (6000 $\overset{\circ}{A}$ of Parylene-N coated with 300 $\overset{\circ}{A}$ of Aluminum on front and back) acts as a UV filter and ion shield.

There is a 400 μm gap between the MCPs which is electrically biased with a slight retarding potential of 50 to 100 V. This reduces the illuminated area in the second MCP, because fast electrons from the first MCP emerge closer to the channel axis. The MCPs are 100 mm X 100 mm square, with 10 to 12.5 μm diameter pores (depending on the supplier) on 12.5 to 15 μm centers. They are $\sim$1500 μm thick, which corresponds to a range of l:d = 120:1 to 150:1. The MCPs are each run at biases in the range of 1500 to 2000 V, with the voltage drop across the front plate being less than that of the back plate. (The plates are not driven into saturation, in order to optimize the energy resolving power of the detector, *i.e.,* FWHM - -4000V with respect to the back surface of the rear plate, operated at ground.

Behind the rear MCP is the readout, the crossed grid charge collector (CGCD). It consists of two orthogonal planes of wires. This will be described in more detail in a separate section. The whole is contained in a vacuum enclosure, and a plastic scintillator is placed behind the detector as an anticoincidence shield.

3.2 Crossed Grid Charge Detector

As mentioned previously, the readout is a crossed grid charge detector (CGCD), which consists of two orthogonal planes of wires electrically separated from each other. The wires are connected to each other by a chain of discrete thin film resistors (R=10 kΩ). The arrangement is depicted in Figure 4.

Each grid consists of 100 μm diameter gold-plated tungsten alloy wires on 200 μm centers. The two grids are held on a ceramic frame which separates them by 400 μm. At a distance of 1000 μm behind the CGCD is a solid reflector plane which is biased about -50V relative to the grids. The grids are biased about +250V with about 1V difference between them to ensure even charge split. Between each wire is a 10kΩ resistor, and every eighth wire is connected to a low input impedance charge sensitive preamplifier, as shown in Figure 5. Associated with each preamp is an amplifier, or "postamp", and an output or "tap". For the purposes of modeling, the preamp and postamp are treated as a single unit, and simply called the preamp. The readout is 96 mm X 96 mm. Each axis has 61 preamps, 480 resistors and 481 wires (E. Hertz, J. Gomes, private communication).

As illustrated in Figure 6, the cgcd is arranged at a distance behind the rear of the MCP stack so that many grid wires collect the charge. If the electron cloud were narrow, the event position would be digitized to the wire spacing. Instead, we exploit the fact that the charge cloud spreads over several wires to calculate the centroid of the charge cloud with a fine position algorithm. The centroid can be determined to a small fraction of a wire spacing. As illustrated in Figure 7, Chappell and Murray (1989) have shown that the electron cloud has a core/halo type of structure; the core had a measured FWHM of .65 μm to .99 μm, or 3 to 5 wire spacings. The halo is large on the scale of taps. Murray and Chappell (1988) have studied several fine position algorithms, and a 3-tap algorithm (described later) was determined to give the best performance. Some of the charge in the halo is lost in a 3-tap algorithm, which results in "gaps" in the raw image, as shown in Figure 8. This is compensated by using a correction factor in our positioning algorithm, as discussed in Section 4.2.

3.3 Processing Electronics

A block diagram of the image processing electronics is shown in Figure 9. The processor identifies the coarse event position using high speed comparators to determine which of the preamps has received the largest signal (because that is the tap closest to the charge cloud centroid). The signals from three taps (the tap corresponding to the coarse position and the taps to either side) are steered through a multiplexer to precision A/D converters. The

digital outputs of the ADCs are the inputs to the 3-tap position algorithm for determining the fine position.

4 Basis of the Modeling

4.1 Charge Division

The position algorithm is based on charge division between adjacent taps when the charge cloud exiting the rear MCP is collected at the wires. Figure 10 illustrates the basic principal of signal location by resistive charge division for a uniformly distributed resistor. The caption shows the analysis leading to the result: $\frac{Q_B}{Q_A+Q_B} = \frac{x}{L}$. For HRC, the problem is slightly different because discrete resistances are involved. The situation for HRC is depicted in Figure 6, which illustrates several wires, two taps labelled i and $i+1$, and the resistors between the wires. For this case, a charge deposited on a particular wire between taps i and $i+1$ will be resistively divided. The wire position will be given by $X_{fp} = \frac{Q_{i+1}}{Q_{i+1}+Q_i}$, where Q_i and Q_{i+1} are the charges collected at taps i and $i+1$, respectively.

For a 3-tap algorithm, the fine position (*i.e.*, the position relative to tap i) is given by

$$X_{fp} = \frac{Q_{i+1}-Q_{i-1}}{Q_{i-1}+Q_i+Q_{i+1}}$$

4.2 Positioning Algorithm

In the 'three-tap positioning algorithm', three ADCs are engaged in detecting an event (one ADC for each of three taps involved in the charge detection). The center ADC is that associated with the tap collecting the largest charge (*i.e.*, the 'coarse position', X_{cp}). The two taps to either side are involved in determination of the fine position, X_{fp}. The model selects as the coarse position, X_{cp}, that tap at which the greatest charge is collected. The fine position, X_{fp}, is calculated by using the signals from all three taps, as appropriate for charge division:

$$X_{fp} = \frac{S_{i+1}-S_{i-1}}{S_{i-1}+S_i+S_{i+1}}$$

where S_i is the output signal from tap i. It is to be noted that this signal is not the same thing as the charge collected at tap i; it will depend on the gain, offset and noise contributed by the associated preamp and ADC.

A raw position X_{raw} can be calculated as

$$X_{raw}=X_{cp} + X_{fp}$$

(Note the error on the front page of the October 16, 1991 memorandum, which erroneously labels this quantity X_{calc} and then refers to it as "the raw calculated position".) The raw position calculated in this way will correctly predict the centroid position of the charge cloud if *all* of the charge has been collected by the three taps. However, is some of the charge is lost (due to the extended halo structure of the charge cloud, for example), the position is incorrectly calculated. This error manifests itself as gaps in the raw image, as was shown in Figure 8.

To compensate for the loss of charge, we modify the fine position algorithm. A single linear correction factor is selected to multiply all X_{fp} , yielding a final calculated position X_{calc}:

$$X_{calc} = X_{cp} + b * X_{fp}$$

(Since this correction factor produces an image without gaps, the process of applying this correction is called "de-gapping".)

We are interested in knowing how well this position algorithm works, that is, how close the calculated position, X_{calc}, is to the actual input position of the event, X_{act}. Thus, appropriate characterization of the position algorithm will involve terms like $\delta_{calc} = X_{act} - X_{calc}$ or $\delta_{raw} = X_{act} - X_{raw}$. A useful figure of merit is σ, the rms value of δ_{calc} (analogous to distortion as defined in Section 2.4):

$$\sigma = \sqrt{\frac{(X_{act} - X_{calc})^2}{N_o}}$$

where N_o is the number of events.

Likewise, we can use the rms value of δ_{raw} to characterize the raw results.

In addition to the rms value, we will be interested in the mean values of δ_{calc} and δ_{raw}. All of these characterizations will be illustrated in the 'baseline' case described later and summarized in Table 4.

4.3   Assumptions and Limitations of the Modeling

In the discussion which follows, I have employed Jon Chappell's program, 'cgcd.c', as modified on 10/24/91. Certain assumptions of that program and their effect on the modeling results have not yet been examined. In particular, three points may be important:

- A continuous charge division is assumed, when in fact there are eight wires between taps with discrete resistors between wires.

- The tap at which the maximum charge is collected is used to define the coarse position. In fact, this might be better defined according to the tap having the maximum signal (voltage), so that gain variations among taps might affect the positioning results.

- The pore size and other elements contributing to the FWHM resolution are not treated here. The input positions are considered known perfectly. (This is the equivalent of having an infinitesimally small pore size.) Thus, the modeling accounts for the contribution by the electronics (preamps and ADCs), but this will not be the dominant contributor to resolution.

- The noise is modeled as a random number multiplied by the noise parameter, and randomly assigned a positive or negative sign. Other models should probably be considered.

In all of the cases below, I have used a Lorentz distribution charge cloud of full-width-at-half-maximum equal to $\Gamma = 2.35 * \sigma_L$ where σ_L=0.2 tap. The results are not expected to depend strongly on the type of charge cloud distribution. (Note that the memo of October 16, 1991 erroneously reports a Gaussian distribution, not a Lorentz distribution.) The distribution of input events is a *uniform* distribution, averaging 10 events per bin, 256 bins per tap. The correction factor is selected as described in the memo of October 16, 1991. (Methods for choosing the correction factor from raw lab data are not discussed here.) It should be noted that the figure of merit and numerical estimates for position accuracy will depend on the choice of correction factor.

5 Results of the Modeling

5.1 Baseline Case

In order to provide a basis of comparison, we begin with the case of ideally matched preamplifiers and ADCs with the expected 'default' performance values in the current design. The default values are typical values for the gain, offset and noise parameters of the preamps and ADCs as measured in the laboratory or dictated by their performance ratings. Table 2 lists these default values for gain, offset and noise in the preamps and ADCs. (In the table, the total charge generated for each input event was 1.2×10^7 electrons.) A remark should be made about the preamp noise. The value shown in Table 2 is the measured rms value of the front-end noise, including thermal noise of the grids and any noise introduced by the preamp. Because of the way the model represents noise (discussed in Section 5.2.2.), using this value as a noise parameter will slightly underestimate the effect of the noise.

TABLE 2

Default values of parameters used in the baseline case.

Preamp Noise: 7×10^{-4} Volts (8000 electrons)
Preamp Offset: 0 ($\pm$ 1 mV)
Preamp Gain: 8.7×10^{-8} ($\pm$ .5%) Volts/electron
ADC Noise: default value is 0 digital counts
ADC Offset: default value is 0 digital counts
    (Note: $\pm$ 1mV = 1.6 digital counts)
ADC Gain: 1638.4 ($\pm$ .5%) digital counts/Volt

Figure 11 shows a histogram of counts/bin for each bin. Only the region between taps 4 and 8 has been examined. The locations, in bins, of the taps and half-tap positions are given in Table 3. One bin represents $1/256^{th}$ of the distance between taps, or 6.25 μm. In this representation, the distribution of counts is with respect to X_{raw} as represented in bins in order to illustrate the gaps. (The distribution with respect to X_{act} is, of course, uniform; its histogram would show an average of 10 counts per bin with fluctuations between 9 and 11 due to the way the events at the edges between bins are assigned.) Note the obvious gaps located at half-tap positions. Figure 12 is a blown-up representation of the first gap in Figure 11. It is symmetrically distributed about the 128th bin with width 36 bins.

TABLE 3

Bin positions associated with each tap.

Tap Position	Bin
4	0
4.5	128
5	256
5.5	384
6	512
6.5	640
7	768
7.5	896
8	1024

Figure 13 is a plot of $\delta_{raw} = X_{act} - X_{raw}$ as a function of bin position. In this and similar representations, the bin position is the actual input position X_{act}, not X_{raw} as in the previous example where it is desired to illustrate the gaps. In addition, the average value for each bin is plotted, rather than each individual event. From Figure 13, it is evident that the position algorithm, using only X_{raw} without a linear correction factor, shows errors of up to 115 μm. The greatest discrepancy occurs at the half-tap points. Note the symmetry about each tap

position, and identical behavior from tap to tap. Figure 14 shows the results after applying a single linear correction factor (selected as described in the memo of October 16, where this correction factor is obtained from the correction factors appropriate to the individual events, weighted according to δ^2_{raw}). In Figure 14 the value of X_{act}-X_{calc} is plotted as a function of actual input position. With linear correction, the position algorithm yields calculated positions that are less than 7.4 μm from the true event positions. (Due to the fact that the histogram takes averages over each bin, the plot of Figure 14 shows excursions of $\sim 5\mu$m or less.) The rms value of X_{act}-X_{calc} (without averaging over each bin first) in this case was 2.18 μm. The rms value of X_{act}-X_{raw} was 62.99 μm. Thus, it is clear for this baseline case that a simple linear correction factor allows adequate positioning by the algorithm. For reference, Table 4 shows the various means of characterizing the positioning, using the baseline case as an example. The values obtained by averaging over bins, as represented in Figures 13 and 14, are also given.

The following sections report results for varying a parameter of interest. In each case, the other parameters were fixed at the default values of Table 2.

<div align="center">

TABLE 4

</div>

Various parameters in microns that characterize positioning. The values given are those found for the baseline case described in the text.

Each event considered individually:

rms $(X_{act} - X_{calc})$	=	2.184
rms $(X_{act} - X_{raw})$	=	62.992
mean of $(X_{act} - X_{calc})$	=	-0.021
mean of $(X_{act} - X_{raw})$	=	-0.061
maximum absolute value of $(X_{act} - X_{calc})$	=	7.384
maximum absolute value of $(X_{act} - X_{raw})$	=	115.27
mean absolute value of $(X_{act} - X_{calc})$	=	1.778
mean absolute value of $(X_{act} - X_{raw})$	=	54.042

For comparison, parameters using average values for each bin (see Section 5.2 below):

rms $(X_{act} - X_{calc})$	=	1.819
rms $(X_{act} - X_{raw})$	=	62.986
mean of $(X_{act} - X_{calc})$	=	-0.021
mean of $(X_{act} - X_{raw})$	=	-0.061

5.2 Varying Parameters for All Preamps or ADCs

Figures 15 through 19 show plots of σ (the rms value of X_{act}-X_{calc}) vs the parameter of interest (in this case noise and offset). In each figure, the slope (m) and intercept (b) of

the best-fit line are shown for rapid calculation of how much the figure of merit, σ, changes given a specific change in the parameter (*e.g.,* a factor of two increase in the preamplifier noise). Figures 15, 16 and 17 examine noise. Figures 15 and 16 are for the case in which the noise has been increased equally in all preamps, and Figure 17 is for the case in which noise has been increased equally in all ADCs. Figures 18 and 19 examine offset. Figure 18 is for the case in which the offset has been increased equally in all preamps, and Figure 19 is for the case in which it has been increased equally in all ADCs. *Equal increases in gain for preamps or ADCs has no effect and this case is not shown.* (The effect on gaps is not discussed here, but it should be noted that increasing the offsets in preamps or ADCs results in an increase in the gap width.) The results obtained from Figures 15 through 19 will be discussed in Sections 5.2.2 and 5.2.3 below.

5.2.1 Evaluation Criteria

Since the diameter of a single pore is about 10 to 12.5 μm, any errors in position introduced by the electronics over their reasonable operating range which are less than a few microns can be deemed negligible. The value of 6 μm has been arbitrarily chosen as a reasonable upper limit for positioning error. Thus, if the figure of merit increases above about 6 μm for a reasonable value of noise or offset, for example, this parameter is flagged as a potential problem. *Table 5 summarizes the results in practical terms for these and the remaining modeling results.* The first column gives the parameter being varied. The second column gives the expected tolerance or rated performance characteristic of the component of the electronics. The third column gives the expected value of σ for the tolerance quoted in column 2 (using the estimate given by the best-fit to the data, or the baseline value of σ if the best-fit value would give a smaller value for σ). Column 4 identifies (with the letter Y) those cases which exhibit $\sigma \geq 6$ μm at the expected performance of the electronics. These cases therefore pose a potential problem for the positioning, provided the effect cannot be calibrated out. (Cases marked with N are not problematic at that value of the parameter.) Since the design tolerances or expected performance may change, column 5 has been included, which gives the value of the parameter satisfying σ=6 μm. This provides an easy reference for identifying how far the performance standards of the electronics may depart from their expected values before the positioning becomes degraded to 6 μm. Some quantities in this column are placed in parentheses to indicate that they are extrapolated far outside the range of the data used in the analysis. Thus, they should be taken to indicate only that the parameter of interest does not pose a problem in positioning over any reasonable range.

TABLE 5

Parameters	Expected Tolerance	σ (in μm) at Tolerance	$\sigma \geq 6\mu$m?	Maximum Parameter[1]	Figure
All preamp gain	1%	unchanged	N	N/A	N/A
All preamp offset	±1mV	2.18	N	(782mV)[2]	18
All preamp noise[3]	.07%	2.18	N	.31%	15
All ADC gain	.025%	unchanged	N	N/A	N/A
All ADC offset	10cts	2.22	N	(1,410 counts)	19
All ADC noise[3]	1ct	2.9	N	4.6 counts	17
ADC gain #2	.025%	2.18	N	(23%)	20
ADC offset #2	10cts	2.20	N	N/A	22
ADC noise[3] #2	1ct	2.1	N	30.9 counts	24
ADC gain #3	.025%	2.18	N	1.4% increase	21
ADC offset #3	10cts	15.9	Y	3.6 counts	23
ADC noise[3] #3	1ct	2.1	N	5.9 counts	25
Single-preamp gains	1%	4.64	N	1.4% increase	37
Single-preamp offset	±1mV	3.35	N	2.5mV	43
Single-preamp noise[3]	.07%	2.18	N	1.04%	46

---

[1]The parameter variation for which $\sigma = 6\ \mu$m.

[2]Quantities in parentheses are extrapolated far outside the range of data used to estimate them.

[3]Noise in the electronics is modeled as a random number between -1 and +1 times the noise parameter.

5.2.2   Varying Noise of All Preamps or ADCs

Consider preamplifier noise as assessed in Figure 15. The default value for the noise parameter is $7\text{x}10^{-4}$ volts (8000 electrons) in the preamps. (As discussed below, this slightly underestimates the noise.) The preamp gain is taken to be $8.7\text{x}10^{-8}$ volts/electron, and the charge generated by each event is $1.2\text{x}10^{7}$ electrons, so that the total signal is 1.0 volt. Thus, the default value for the noise parameter represents 0.07% of the signal. The range of variation in Figure 15 is a factor of 10 times the default value, or up to 0.7% of the signal. The slope (m) and intercept (b) of the best-fit line are shown for the noise expressed in volts, or expressed as a percentage of the signal. A wider dynamic range of noise for a wide range of total charge is shown in Figure 16, where the noise is expressed as a percentage of the total signal. In Figure 16, the data have been fit with quadratics and four different total charges are examined: $6\text{x}10^{6}$, $1.2\text{x}10^{7}$, $5.7\text{x}10^{7}$ and $1.15\text{x}10^{8}$ electrons. There is no obvious dependence of σ on the total charge, and the results are virtually indistinguishable for preamp noise below about 2% of the total signal. Thus, the value of σ is taken simply to be a function of the percentage of total signal.

It is important to note that the noise parameter is multiplied by a random number between -1 and +1 to model the noise in the electronics. Other models should be considered, but are not treated here. As stated previously, typical front-end noise including thermal noise of the grids and noise introduced by the preamps is about $7x10^{-4}$ volts. This is not a peak-to-peak estimate of noise, but an rms value. The effective peak-to-peak value would be higher, assuming a Gaussian distribution. Since our noise model is a simple flat distribution, using the default value as the maximum value of this distribution will underestimate the effect of noise. The appropriate noise parameter would thus be higher. For the preamplifier noise, a wide range has been examined. As evaluated by the model, the expected noise of .07% (measured in the laboratory) does not pose a problem for the positioning. As shown in column 5 of Table 5, the noise must remain below 0.31% of the signal in the model in order for σ to remain below 6 μm. Thus, there is no anticipated problem with regard to noise in the preamplifiers. Nevertheless, the effect of noise is underestimated by the model, and since the effect of noise cannot be calibrated out, control of this parameter is indicated.

For the case of noise in the ADCs, as illustrated in Figure 17, the ADCs can be expected to have a digitization error of at most one count. This corresponds to a value of $\sigma = 2.9$ μm, which does not constitute a problem.

5.2.3 Varying Offsets of All Preamps or ADCs

Consider now the case of varying all of the offsets uniformly. The preamps are expected to have a maximum variation of ± 1mV at low signal levels, corresponding to a negligible increase of only .013 μm as indicated in Figure 18. Similarly, the ADCs are expected to have a full-scale error of 10 counts out of 4096. As seen in Figure 19, this variation would affect σ negligibly (less that 0.03 μm). As shown in column 5 of Table 5, the offsets of all the preamps or ADCs would have to be increased beyond reasonable levels to degrade σ to 6 μm. *Consequently, uniformly varied adjustments in the ADC or preamplifier offsets should not increase σ significantly.* Non uniform offsets are treated in Sections 5.3.2 and 5.4.2

5.3 Varying a Single ADC

Figure 20 through 25 represent the effect of varying one of the parameters of interest (gain, offset or noise) for a single ADC. Figures 20, 22 and 24 show the results for the second or middle ADC (corresponding to the tap associated with the coarse position). Figures 21, 23 and 25 illustrate the results for the third ADC. Three cases are considered: varying the gain (Figures 20 and 21), varying the offset (Figures 22 and 23), and varying the noise (Figures 24 and 25).

5.3.1 Varying the Gain of a Single ADC

Consider the effect of varying the gain of one of the ADCs, as illustrated in Figures 20 and 21. Note that when the gain of the second ADC is increased, σ *decreases* to a local minimum. (Figure 20 has been fitted with a quadratic, whereas most of the other plots have

linear fits. A linear plot is generally adequate for the purpose of estimating the sensitivity of σ with respect to the parameter of interest.)

The ADCs are matched to about 1 part in 4000 (or 0.025%). In the case of both the second and third ADCs, this corresponds to a negligible change in σ. The third ADC gain would have to be increased by 1.4% relative to the others in order to degrade the positioning to 6 μm. Thus, *the expected variation in gain of the ADCs does not pose a problem in the positioning.*

5.3.2 Varying the Offset of a Single ADC

Consider Figures 22 and 23, in which the ADC offset is increased over a range of 30 digital counts. The full-scale error for the ADCs is 10 counts out of 4096. This corresponds to a negligible increase (.007 μm) in positioning error for the case of varying the second ADC. (In fact, within the limits of the crude fit over this limited range, there is no projected offset in the second ADC that would pose a problem in the positioning, as indicated by N/A in column 5 of Table 5.) However, an offset of 10 digital counts in the third ADC will result in σ=15.9 μm, which would constitute a problem for the position accuracy. As shown in column 5 of Table 5, the offset of the third ADC must remain below ~4 digital counts to keep σ below 6 μm. It is important to note, however, that an absolute offset of this magnitude can be calibrated out. (It would only pose a problem if this represented the uncertainty in the offset.)

5.3.3 Varying the Noise of a Single ADC

Figures 24 and 25 show the effect of increasing noise. Typical noise in the ADCs (which we consider to be the digitization error) is one count. For the second or third ADC, a noise parameter of 1 count will not noticeably increase σ. The second ADC noise parameter would have to increase to ~31 digital counts before σ=6μm. The third ADC noise parameter is more strictly limited: it would have to be kept below ~6 digital counts to limit σ to 6μm.

5.3.4 Symmetries of Single ADC Variations

Varying a single ADC in general produced symmetric results in plots of δ_{calc} vs input position (where $\delta_{calc} = X_{act} - X_{calc}$), so that at no single tap was the effect different than at any other. This is an advantage arising from the fact that all three ADCs are involved in calculating the position (and obtaining δ and σ), no matter where the initial event arrives. (As shown in the next section, this symmetry is lost when a single preamplifier is varied relative to the other preamplifiers.) There are differences in the plots of σ vs input position depending on whether the second or the third ADC is involved. As illustrated in Figure 26 for the case of a 10-count offset in the second ADC, the characteristic shape of Figure 14 (for the baseline case) is retained when any parameter of the second ADC is varied, or when only the noise is varied for the third ADC. However, as shown in Figure 27, the shape of this curve (as well as its amplitude) changes when the gain or offset of the third ADC is increased. The two cases are distinguishable by gaps as well, which are not discussed in this document.

Thus, the analysis shows that, for all reasonable parameter ranges, *the second ADC will not pose a problem for positioning. Furthermore, gain variations and noise (digitization) within expected limits in one of the "side" ADCs will not present a problem, but offset variations can.*

5.4 Varying a Single Preamplifier

Before beginning the discussion of detailed results concerning variations in gain, offset and noise for a single preamplifier, a remark must be made concerning how the analysis was done. In all prior analysis, the value of σ is calculated from the values of δ_{calc} from each individual event. In the cases pertaining to variations in a single preamp, however, the analysis is done by referring to smaller files which contain information for each bin rather than each event: in other words, average values have been recorded for each bin. By weighting these numbers according to the number of events in each bin, a meaningful figure of merit is recovered. However, by first averaging over bins, the rms value of δ, or σ, will always be reduced (although the mean value of δ can be recovered). The two types of analysis can be compared by examining Table 4, which gives the figures of merit obtained in both fashions. This is also illustrated in Figure 28, where σ is shown for two cases: the top curve (labelled actual rms_calc) shows the case where σ is calculated event-by-event, and the bottom curve shows σ obtained by using the weighted average values in each bin. Also shown in the figure are the slope (labelled m) and intercept (labelled b) of the best-fit lines to the data points. As can be easily seen in the figure, for our purposes it is adequate to use the bin-averaged value for σ, while recognizing that the numerical values may differ slightly from those found by performing the analysis event-by-event. For the case illustrated, the two types of analysis would yield values in columns 3 and 5 of Table 5 which differ by less than 7%.

5.4.1 Varying the Gain of a Single Preamplifier

Figures 29 and 30 show the distribution of $\delta_{raw} = X_{act}\text{-}X_{raw}$ as a function of true input position for a 5% increase in the gain of preamp #6 (Figure 29) and in preamp #5 (Figure 30). It should be noted first of all that Figure 30 can be obtained from Figure 29 simply by sliding the curve to the left one tap. This is a confirmation of what is to be expected: that the particular choice of which tap is "tweaked" is immaterial. The range of taps affected extends to the tweaked tap N and the two side taps N ±1, but not to taps N ±2. Because we have effectively truncated the analysis with only half the range appropriate for taps 4 and 8, it is necessary to sum the two regions together before calculating, for example, the mean value of δ_{raw}.

Figures 31 and 32 show the corresponding plots of $\delta_{calc} = X_{act}\text{-}X_{calc}$ as a function of true input position for a 5% increase in the gain of preamp #6 (Figure 31) and of preamp #5 (Figure 32). Because the same correction factor was not selected in each case, the curves are not identical. However, they do show the expected behavior in that they are similar, but shifted with respect to each other by one tap. The general analysis for variations of a single preamp will therefore restrict itself to a discussion of the case of varying the gain of preamplifier #6. (Similarly, in the discussions concerning offset and noise, we will restrict

ourselves to varying preamplifier #6.) Obviously, the conclusions are applicable to variations in any particular preamplifier, N. Therefore, in the figures the taps are identified according to the "tweaked" preamplifier (at tap N), the two taps to the side (taps N ±1), and the unaffected taps beyond (taps N ±2).

In Figures 29 and 30, it is evident that taps N+2 and N-2, which are unaffected by the perturbation of the preamp corresponding to tap N, show a symmetric distribution of δ_{raw} about 0, ranging smoothly from about -115 μm to +115 μm. The distribution is also symmetric at tap N, but the range is greater, as expected. For taps N+1 and N-1, the distribution is no longer symmetric: δ_{raw} is raised, on average, for tap N+1 and symmetrically depressed for tap N-1. In addition, the range of variation is less. These qualitative observations are reflected in Figures 33 and 34, respectively showing the mean and rms values of X_{act}-X_{raw} as a function of the percentage gain increase in preamplifier #6. As expected, taps N and N ±2 show a mean of 0 in Figure 33, reflecting the symmetry seen in Figure 29. It was noted that X_{act}-X_{raw} was raised for tap N+1, indicating a positive mean value; this is also seen in Figure 31. Tap N-1 was symmetrically depressed, and this is also evident. Figure 34 illustrates the remarks made about the variation in range observed in Figure 29. As remarked, tap N has a greater range than the unperturbed taps N ±2, and this is reflected in the fact that the rms value shown in Figure 34 is greater for tap N. Conversely, taps N ±1 had a smaller range of variation than the unperturbed taps, and this too is evident. It is clear in Figures 33 and 34 that the variation is approximately linear with gain. The data have been plotted with best-fit lines. The slopes are indicated in the figures.

Figures 31 and 32 can be characterized in a similar fashion. Figure 35 shows the mean value of δ_{calc}=X_{act}-X_{calc}. Taps N and N ±2 have zero mean (where the distribution for taps 4 and 8 have first been added together because the full range for each of these taps is not included). This is to be expected: when a linear correction factor (a constant) is applied to the fine positions contributing to X_{raw}, symmetric distributions of X_{act}-X_{raw} (with respect to zero) result in symmetric distributions of X_{act}-X_{calc}. Thus, the mean value of X_{act}-X_{calc} is zero for taps N, N ±2. Tap N+1 still has a positive mean value after correction, and tap N-1 has a negative mean. Again, it is approximately linear with gain and the best-fit line is plotted.

Figure 36 shows the rms value of δ_{calc}. Note that the curve (connecting the raw data points) for tap N+1 overlaps that of tap N-1. This is also true of the curves for tap N+2 and tap N-2. Note that the rms value of X_{act}-X_{calc} in Figure 36 is considerably reduced in scale relative to Figure 34, indicating the efficacy of using a simple linear correction factor. Figure 37 shows the data of Figure 36 plotted with the best-fit lines. The slopes are also indicated. Since the preamplifier gains are matched to better than 1 %, the projected limit on degradation in positioning would be about 4.6 μm for the worst case, taps N+1 or N-1. Thus, we do not expect preamplifier gain variations to pose a problem in positioning. The position accuracy is not projected to degrade to 6 μm until the gain of one preamplifier is increased by 1.4 % relative to the others, as shown in column 5 of Table 5.

5.4.2 Varying the Offset of a Single Preamplifier

Figures 38 and 39 show the effect of introducing an offset into one preamplifier. Figure 38 shows $\delta_{raw} = X_{act} - X_{raw}$ as a function of input position when preamplifier #6 is given a 10 mV offset. Figure 39 is the corresponding plot of $\delta_{calc} = X_{act} - X_{calc}$. Figure 38 shows that δ_{raw} is symmetric about zero for taps N and N$\pm$2. Tap N+1 is raised, and tap N-1 is depressed relative to zero. This is clearly indicated in Figure 40, which is a plot of the mean of δ_{raw} as a function of offset. For each offset, taps N and N$\pm$2 show zero mean, whereas tap N+1 shows a positive mean and tap N-1 a negative mean. The dependence with offset is linear. Figure 41 shows the rms value of δ_{raw}. Since tap N$\pm$2 is unaffected when tap N is "tweaked", the rms values will not change. This is seen in Figure 41, where the N$\pm$2 curve is flat. In Figure 38, δ_{raw} varied through a greater range for tap N than for taps N$\pm$2, and this is reflected as an increased rms value in Figure 41. In Figure 38, taps N$\pm$1 are additionally offset, so the rms value is larger still in Figure 41.

Figures 42 and 43 are plots of the mean and rms values, respectively, of $\delta_{calc} = X_{act} - X_{calc}$. The symmetry about $\delta_{raw} = 0$ in Figure 39 explains the qualitative behavior of Figure 42. In Figure 43, which shows σ (the rms value of δ_{calc}), the data have been fit with quadratics whose parameters are indicated on the plot. Again, the general behavior can be predicted from Figure 39. For example, in Figure 39, δ is very far from zero for taps N$\pm$1, so that the rms value in Figure 43 is much larger than for the other taps. Since taps N$\pm$1 constitute the worst case, it has been used to determine the maximum allowable offset. As shown in column 5 of Table 5, $\sigma = 6$ μm will be reached for an offset of 2.5 mV. Since the preamplifier offsets are expected to agree within 1 mV, this does not pose a problem.

5.4.3 Varying the Noise of a Single Preamplifier

Figures 44, 45 and 46 show the effect of introducing noise into a single preamplifier. In these figures, the noise of preamplifier #6 has been increased ten-fold, to 0.7%. Figure 44 is a histogram of the input event distribution as a function of X_{raw}. Notice in this figure that the first and last taps (taps N$\pm$2) have the least noise, the center tap (tap N) has more noise, and taps N$\pm$1 have the most. This is to be expected from the way tap N enters into the position algorithm (see Section 4.2). Figure 45 is a plot of $\delta_{raw} = X_{act} - X_{raw}$ vs true input position, X_{act}, and Figure 46 shows $\delta_{calc} = X_{act} - X_{calc}$. The noise follows the expected behavior as was seen in Figure 44.

Figure 47 is a plot of σ as a function of noise expressed as percentage of the total charge. As before, the noise was introduced only into preamp #6. To simplify the figure, only curves for taps N, N-1 and N-2 are shown. Quadratics have been fit to the data, and the parameters applicable to tap N-1 are indicated in the figure. Since taps N$\pm$1 constitute the worst case, the parameters indicated on the plot have been used to determine the maximum allowable noise. As shown in column 5 of Table 5, $\sigma = 6$ μm will be reached for noise equal to 1.04% of the total charge. This is much larger than typical values (.07%) found in the laboratory.

5.5 Conclusions of the Modeling

Within the limits imposed by the modeling as outlined previously, we conclude that the current design of the event processing electronics does not pose a problem for the accuracy of the positioning algorithm. We find that the positioning accuracy is largely insensitive to:

1. Uniform variations in gain or offset for preamps and ADCs, and

2. Variations in gain, offset or noise in the second ADC (associated with the coarse position).

The areas which have the most impact on the position accuracy and merit attention have been identified. In particulary:

1. Noise in the preamps should be controlled, since this statistical effect cannot be calibrated out and is underestimated by the model.

2. An offset greater than ∼4 digital counts in the third ADC (*i.e.,* either of the ADCs to the "side" of the second ADC) would need to be calibrated out. (Note that 4 counts is within the full scale error of the ADCs.)

3. The present performance ratings of the preamplifiers assure that they are adequately matched. However, if the preamplifier gains or offsets vary beyond these limits (by a factor of ∼2), then the effect would need to be calibrated out.

6 Algorithm Noise Factor

6.1 Knapp Analysis

The analysis below is a summary of that presented by Knapp, computing the positional uncertainty of a 3-tap algorithm due to electronic noise. Recall (Section 4.2) that for a 3-amplifier system, the position can be given by

$$P = \frac{S_{i+1} - S_{i-1}}{S_{i-1} + S_i + S_{i+1}} = \frac{S_{i+1} - S_{i-1}}{S}$$

The position uncertainty is given by

$$\Delta P = \sigma_e [(\frac{\delta P}{\delta S_{i-1}})^2 + (\frac{\delta P}{\delta S_i})^2 + (\frac{\delta P}{\delta S_{i-1}})^2]^{\frac{1}{2}}$$

where σ_e is the rms value of N_e, the noise electrons of the preamplifier and postamplifier combined. (The combined noise is called the front end noise.) This leads to

$$\Delta P = \frac{\sigma_e}{S^2} [2S^2 + 3(S_{i+1} - S_{i-1})^2]^{\frac{1}{2}}$$

If we deposit charge at a fractional distance m from the amplifier i, between i and $i+1$, then the charge division becomes

$$S_i = (1 - m)S$$
$$S_{i+1} = m\ S$$
$$\text{and } S_{i-1} = 0$$

We obtain

$$\Delta P = \frac{\sigma_e}{S}(2 + 3m^2)^{\frac{1}{2}}$$

For a 3-amplifier system, the spot can extend over two taps with a centroid limit of $\pm\frac{1}{2}$ tap. A plot of $k = (2 + 3m^2)^{\frac{1}{2}}$ is given in Figure 48. It is apparent that k varies from a minimum of $\sqrt{2}$ at $m = 0$ to a maximum of 1.66 at $m = \pm\frac{1}{2}$, the extremes of the centroid range. If no noise contribution from the crossed grid is assumed, the maximum error will occur at $m = \frac{1}{2}$, with

$$\Delta P_{max} = 1.66\frac{\sigma_e}{S}$$

Figure 49 illustrates this range of k, not only for a 3-tap algorithm, but for algorithms involving 2-taps through 6-taps. (The hatched portion in the figure indicates the range between minimum and maximum errors.) It is evident from the figure that increasing the number of taps will increase k, and hence the noise.

Recall that for the general case in which, for example, the 3-amplifier system may be connected with many groups in parallel over a partitioned anode, we have:

$$\Delta l \quad = \frac{N_e k g^{\frac{1}{2}} l}{Sn}$$

$\Delta l \quad$ = uncertainty in location

$l \quad$ = length of anode

$n \quad$ = number of partitions over the length of the anode

$k \quad$ = algorithm noise factor

$g \quad$ = number of amplifier groups connected in parallel

$N_e \quad$ = noise of a single amplifier

$S \quad$ = (total) signal

The general analysis shows three trends:

1. increasing the number of partitions, n, improves the resolution;

2. k increases with increasing number of amplifiers (*i.e.*, a 4-tap algorithm has more noise than a 3-tap algorithm); and

3. if amplifier groups are connected in parallel, g is greater than 1 and Δl is increased.

The algorithm chosen for HRC is a 3-tap algorithm selecting a discrete group (unlike the arrangement for the *Einstein* HRI). The selection of 3 taps was made based on the minimum

number of taps consistent with the expected size of the charge cloud.

For HRC, we have $\frac{l}{n} = 1600$ μm and $g = 1$. If we use typical values of $\sigma_e = 8000$ electrons, $S = 1.2x10^7$ electrons and $k \sim 1.66$, we obtain $\sigma_p = 1.7$ μm. This is in good agreement with the modeling results, for which we found $rms(X_{act} - X_{calc}) = 2.2$ μm after linear correction (which corrects well but imperfectly).

6.2   Application to Experiment

This discussion below summarizes results obtained by Murray and Chappell (1988). Four images of a test mask obtained with the HRC prototype were analyzed in order to determine the spatial resolution. These images were obtained with 3,4,5 and 6-tap algorithms. It was assumed that the image quality was due to two components: the effect of electronic noise (with FWHM Γ_{elec}) and systematic contributions (Γ_{sys}) such as the MCP pore size. The contribution from the electronics was assumed to be equal to an effective value of the noise coefficient, k (as discussed above in the Knapp analysis), times the contribution of a two-tap system

$$\Gamma_{elec} = K_{eff} \cdot \Gamma_{e2}$$

Best-fit values of Γ_{e2} and Γ_{sys} were obtained:

$$\Gamma_{sys} = 22.7 \ \mu m$$
$$\Gamma_{e2} = 11.0 \ \mu m$$

These were found to agree reasonably well with what would be expected based on a 12.5 μm pore size and the measured rms noise.

7   References

- Chappell, J.H. and Murray, S.S., 1989, *SPIE, EUV, X-ray and Gamma-ray Instrumentation for Astronomy and Atomic Physics*, **1159**, 460. Position Modeling for the AXAF High Resolution Camera.

- Fraser, G.W. 1989 *X-ray Detectors in Astronomy*, Cambridge University Press.

- Henry, J.P., Kellogg, E.M., Briel, U.G., Murray, S.S., and Van Speybroeck, L.P., 1977, *SPIE, X-ray Imaging*, **106**, 196.

- Kellogg, E., Henry, P., Murray, S., Van Speybroeck, L., and Bjorkholm, F., 1976, *Rev. Sci. Instrum.*, **47**, 282.

- Knapp, Guenther, 1978, *Rev. Sci. Instrum.*, **49**, 982.

- Lapington, J.S., Kessel, R., and Walton, D.M., 1988, *Nucl. Instrum. Meth in Physics Research*, **A273**, 663.

- Murray, S.S. and Chappel, J.H., 1985, *SPIE, X-ray Instrumentation in Astronomy*, **597**, 274. The Advanced X-ray Astrophysics Facility High Resolution Camera.

- Murray S.S. and Chappell, J.H., 1988, *SPIE, X-ray Instrumentation in Astronomy II*, **982**, 48. The AXAF High Resolution Camera.

- *Preliminary Design Document.* High Resolution Camera on the Advanced X-ray Astrophysics Facility (AXAF), 1988.

- Proposal to National Aeronautics and Space Administration for High Resolution Camera (HRC) on the Advanced X-ray Astrophysics Facility (AXAF). Phase C/D Proposal Revision, 1989

8 Figures
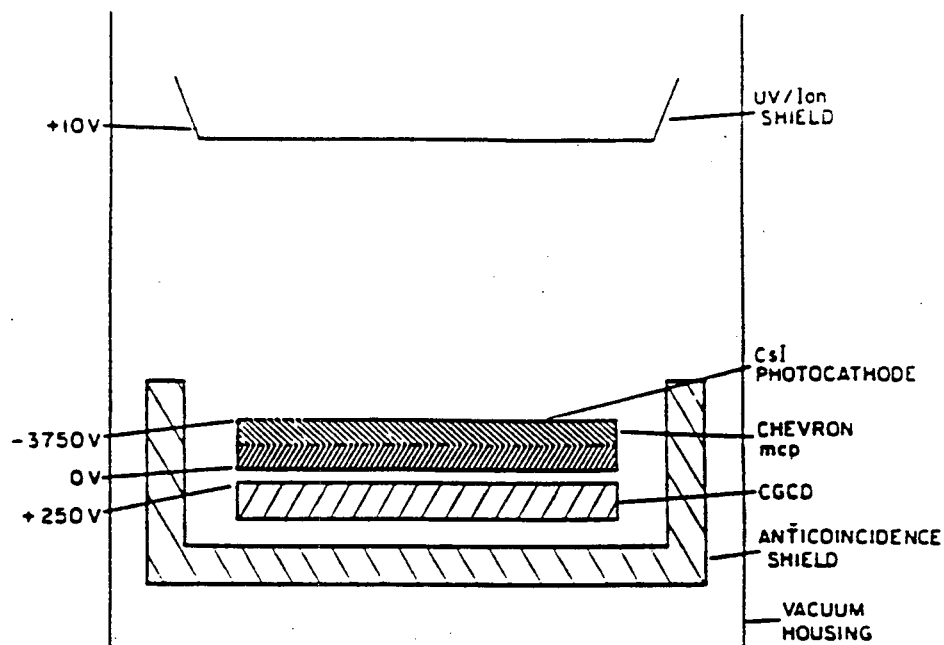
Figure 1 Major elements of HRC. (Murray and Chappell, 1985)
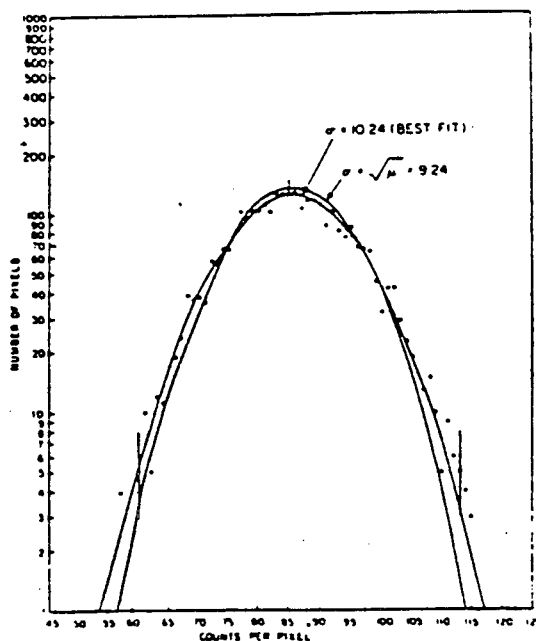
Figure 2 Histogram of the number of pixels containing a given number of counts in a uniformly exposed region. The curves are Gaussian distributions with $N_{TOT}=3146$ and $\mu=85.375$. This analysis is used to estimate the degree of nonuniformity of efficiency. (Henry, *et al.*, 1977)
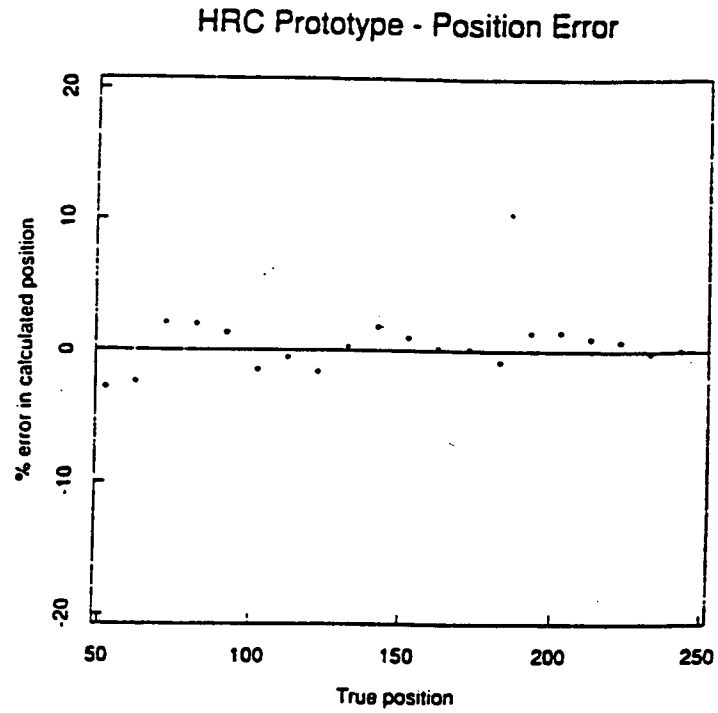
Figure 3 Percent error in measured position versus true
position showing residual errors after large scale "de-gapping"
corrections are made. This data gives a measure of distortion.
(C/D Proposal, 1989)
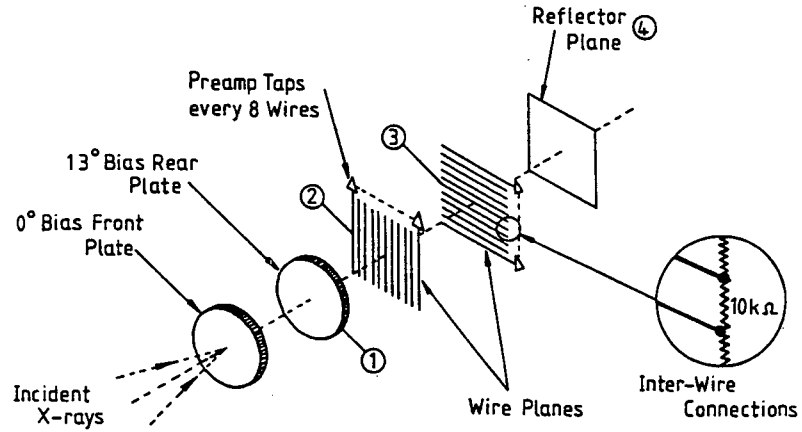
Figure 4 Exploded view of detector components showing basic arrangement of CGCD. (Fraser, 1989)
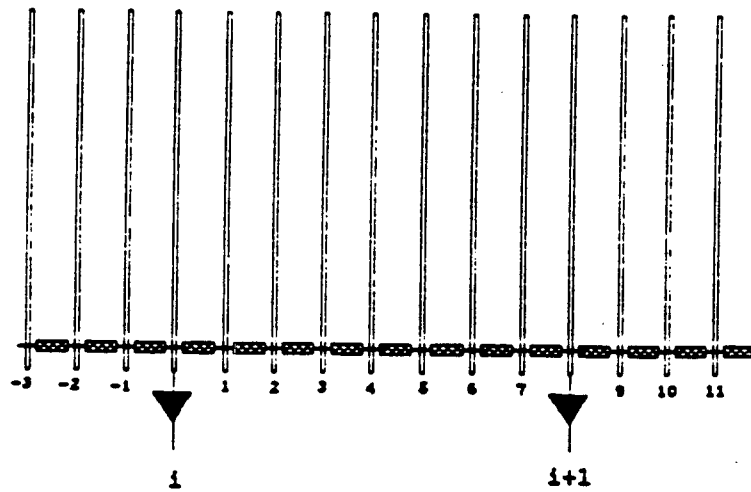
Figure 5 Schematic diagram of CGCD in one dimension. (Murray and Chappell, 1985)
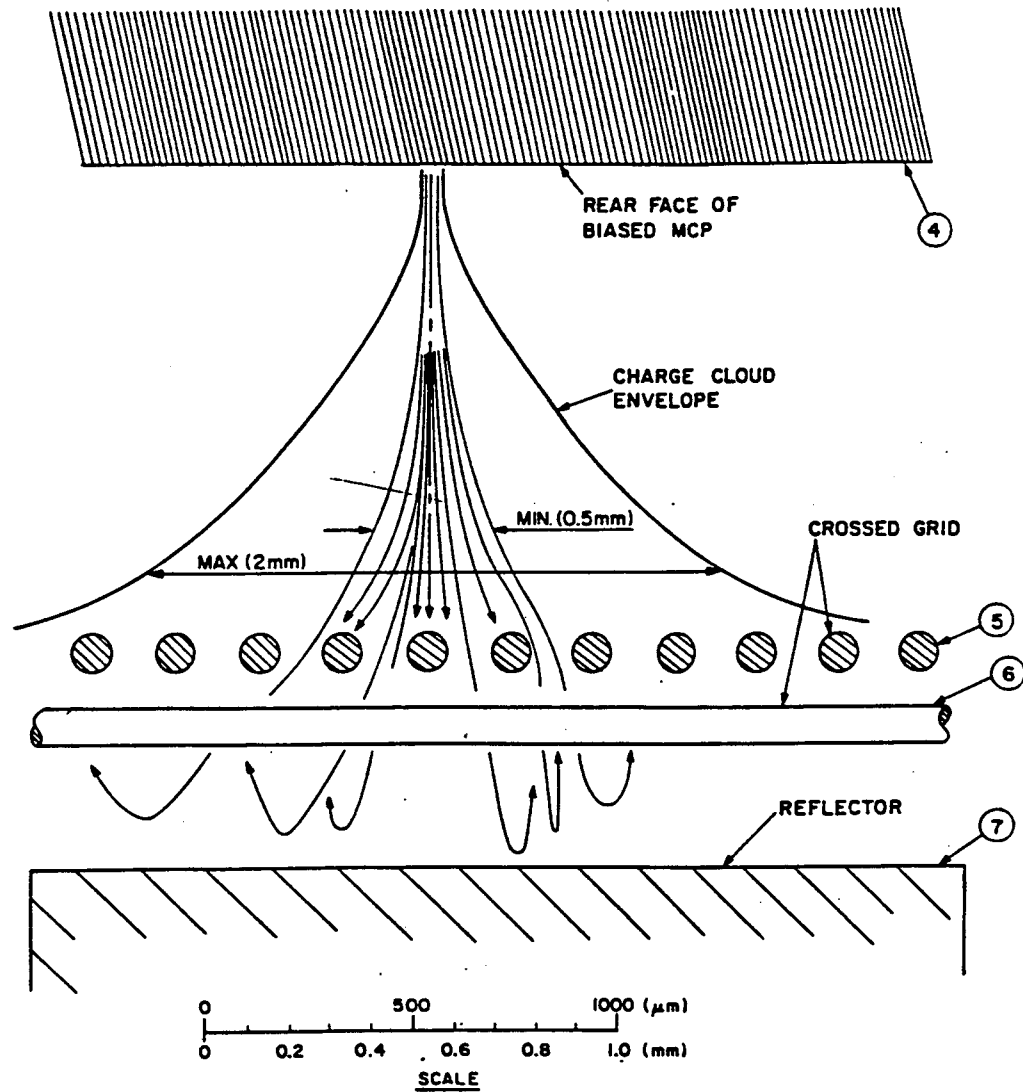
Figure 6 Schematic electron trajectories. The electron cloud spreads over several wires of the CGCD. The dimensions quoted are for the *Einstein* HRI. (4=rear face of MCP; 5=wire; 6=wire of the orthogonal plane; 7=reflector plane) (Kellogg, *et al.*, 1976)

MCP Charge Distribution x-axis

Lorentz Fit Parameters
A = 217.0534
Xo = 4.0099
Γ = 0.4047

Counts/Tap

Tap Number

MCP Charge Distribution y-axis

Lorentz Fit Parameters
A = 269.1207
Xo = 4.0122
Γ = 0.617

Counts/Tap

Tap Number
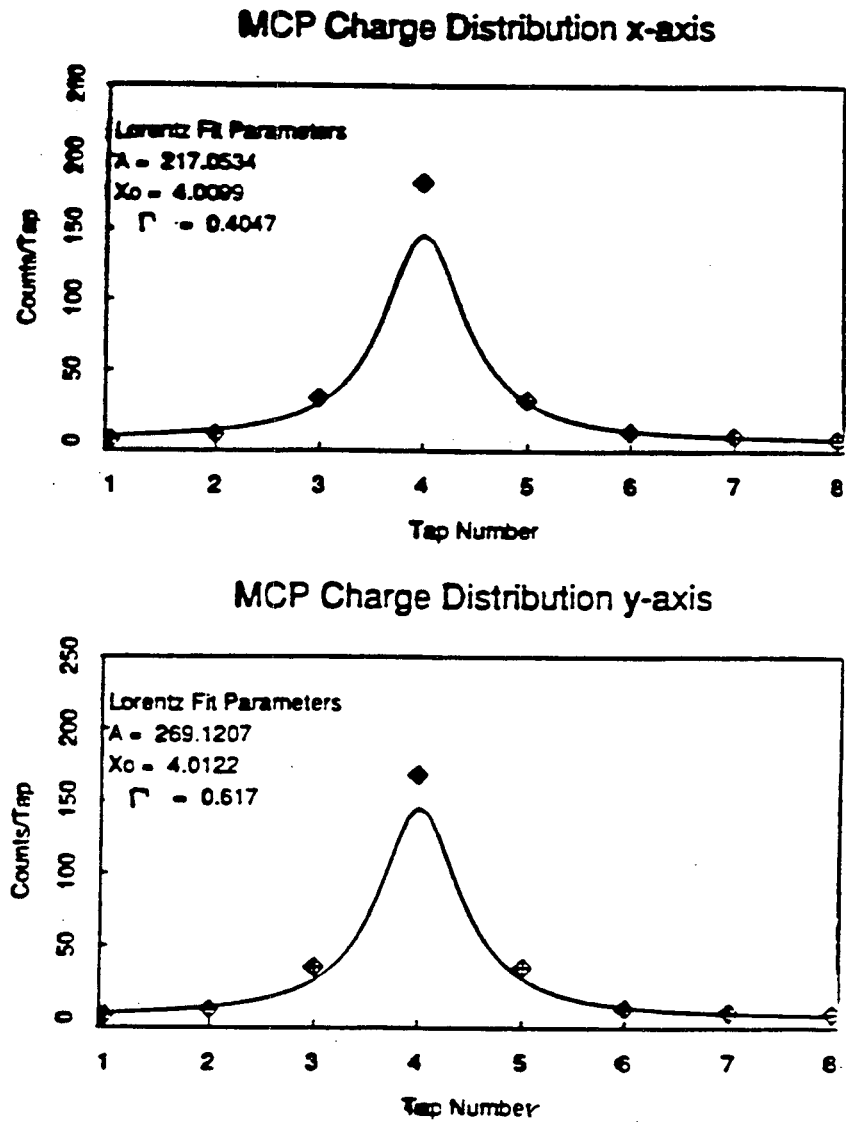
Figure 7 Measured charge cloud distribution function vs. tap position. (Chappell and Murray, 1989)
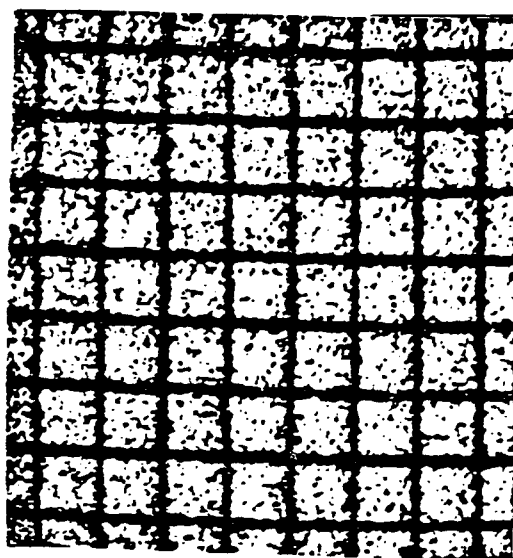
Figure 8 Gaps apparent in raw flat-field image. "De-gapping" is accomplished by applying a linear correction factor. (Chappell and Murray, 1989)

FROM COARSE
POSITION LOGIC
(NOT SHOWN)

TIMING SIGNALS
FROM SEQUENCER
(NOT SHOWN)

64: 3 SELECTOR

CHG INJECT
CORRECTION

ANALOG
MUX

FAST
T/H
AMP

PRECISION
T/H

ADC

offset
adj.

INPUTS
FROM
GRID

84

FAST
T/H
AMP

PRECISION
T/H

ADC

OUT

offset
adj.

FAST
T/H
AMP

PRECISION
T/H

ADC

offset
adj.

14 BIT ADC
(EFFECTIVE RANG
<15us CONV.TI

SELECT 3 CHANNELS
ABOUT PEAK

FAST
CAPTURE OF
WAVEFORM PEAK
~4us

PRECISION
HOLD
~20us

GRID
PREAMPS/POSTAMPS

HRC FINE POSITION CIRCUIT
SIMPLIFIED DIAGRAM

Figure 9 Block diagram of the HRC image processing electronics. (Jack Gomes, private communication)
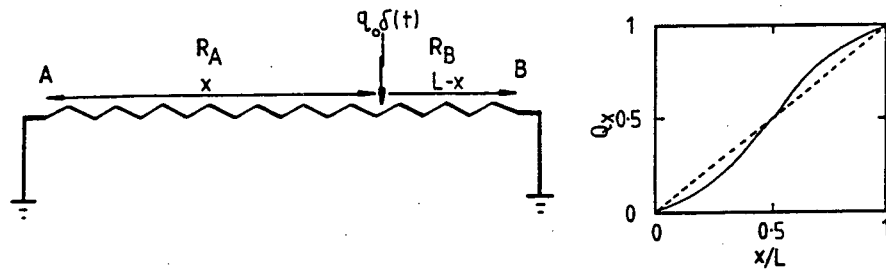
Figure 10 Principal of signal location by resistive charge division. A current impulse $i_0 = q_0\delta(t)$ is injected to a uniformly distributed resistor, total resistance R, at coordinate x. The currents flowing into the shorted ends A, B are such that (i) $i_A + i_B = i_0$, and (ii) $i_A R_A = i_B R_B$. R_A and R_B are the resistances between the point of current injection and the ends of the resistor. Obviously: (iii) $R_A = (x/L)R$, and (iv) $R_B = (1 - x/L)R$. Manipulation of (i)–(iv) gives the result: $i_B/i_0 = i_B/(i_A + i_B) = x/L$.

(b) Amplitude ratio Q_x. Broken curve = ideal. Full curve = measurement (the s-curvature is exaggerated for the purposes of illustration). (Fraser, 1989)
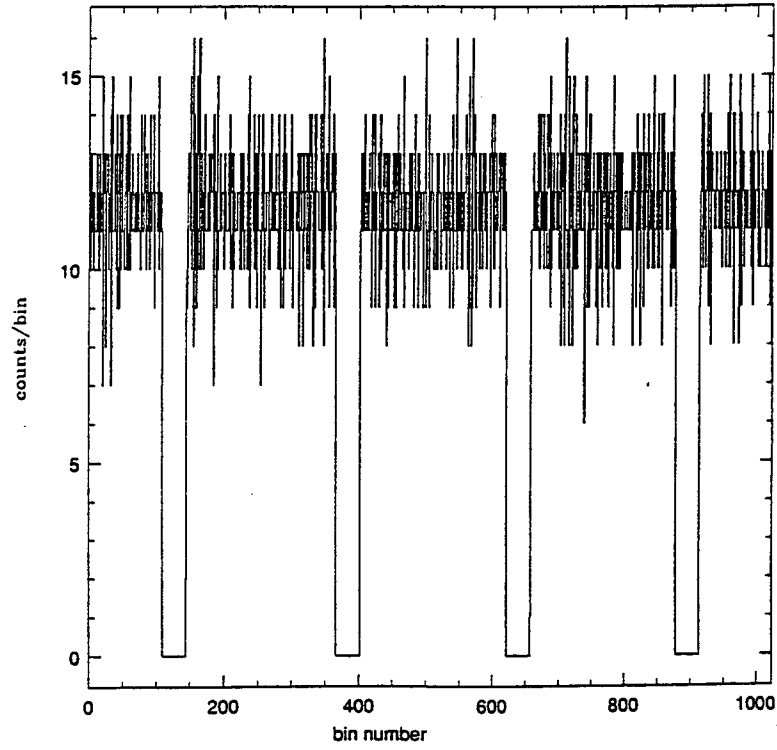
Figure 11 Histogram of input events as a function of X_{raw} to show gaps. The true input distribution (as a function of X_{act}) is uniform. (Baseline case)
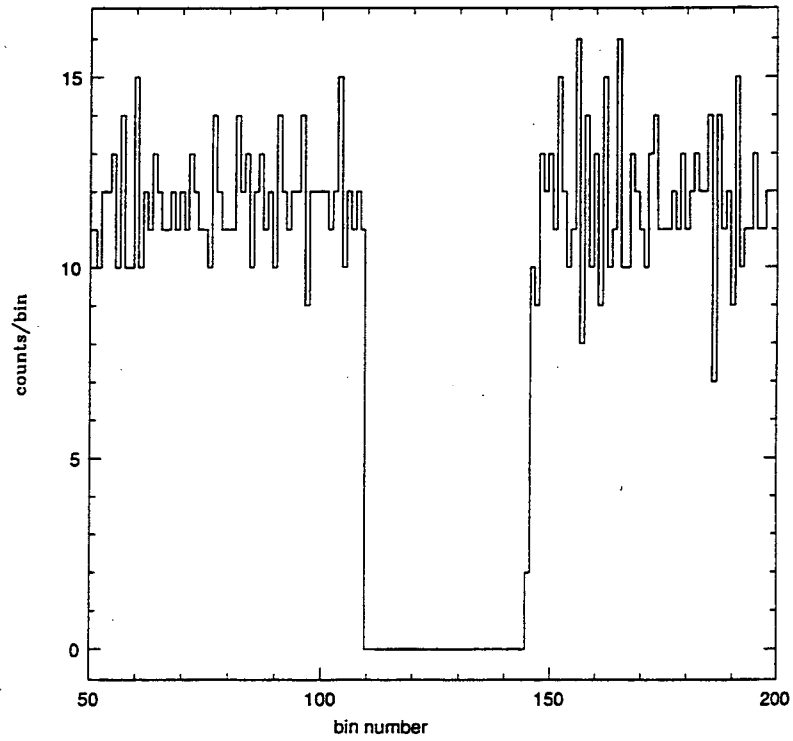
Figure 12 First gap of Figure 11. (Baseline case)
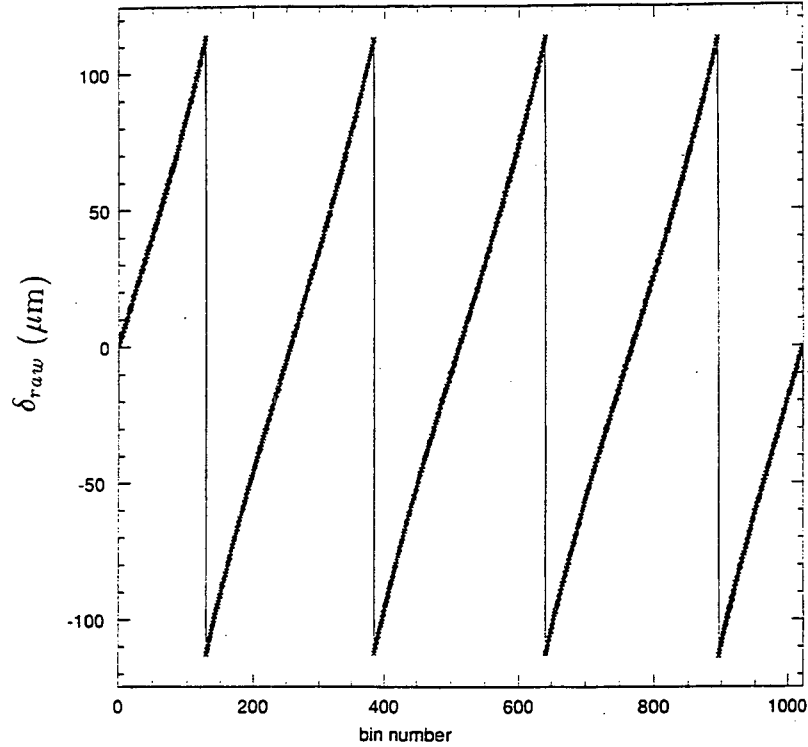
Figure 13 Plot of $\delta_{raw}=X_{act} - X_{raw}$ as a function of true input position, X_{act}, for the baseline case.
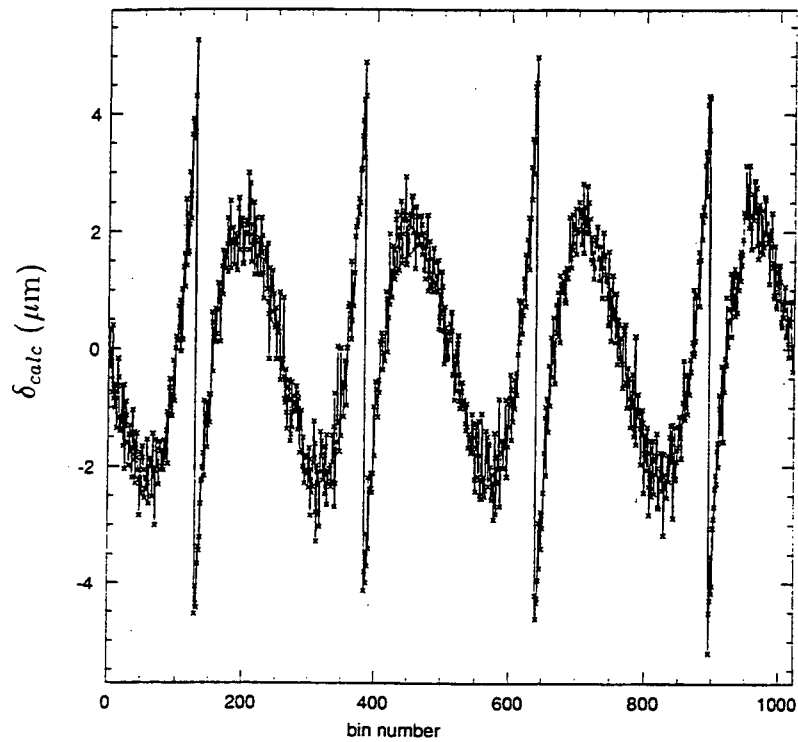

Figure 14 Plot of $\delta_{calc}=X_{act} - X_{calc}$ (after linear correction factor has been applied) as a function of true input position, X_{act}, for the baseline case. Note that applying a linear correction factor reduces the position error by more than an order of magnitude.
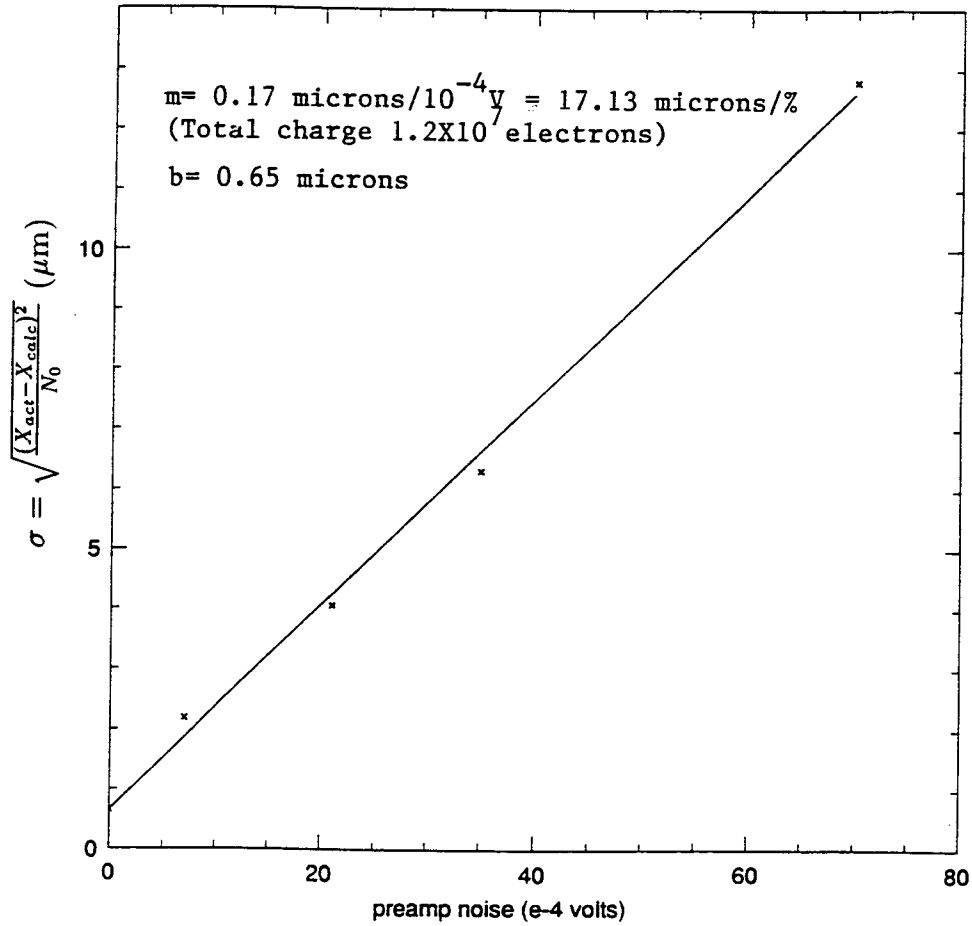
Figure 15 Plot of $\sigma = \sqrt{\frac{(X_{act}-X_{calc})^2}{N_0}}$ in μm as a function of preamp noise in volts. The total charge was 1.2×10^7 electrons, corresponding to 1 volt. The noise has been varied equally in all preamps.
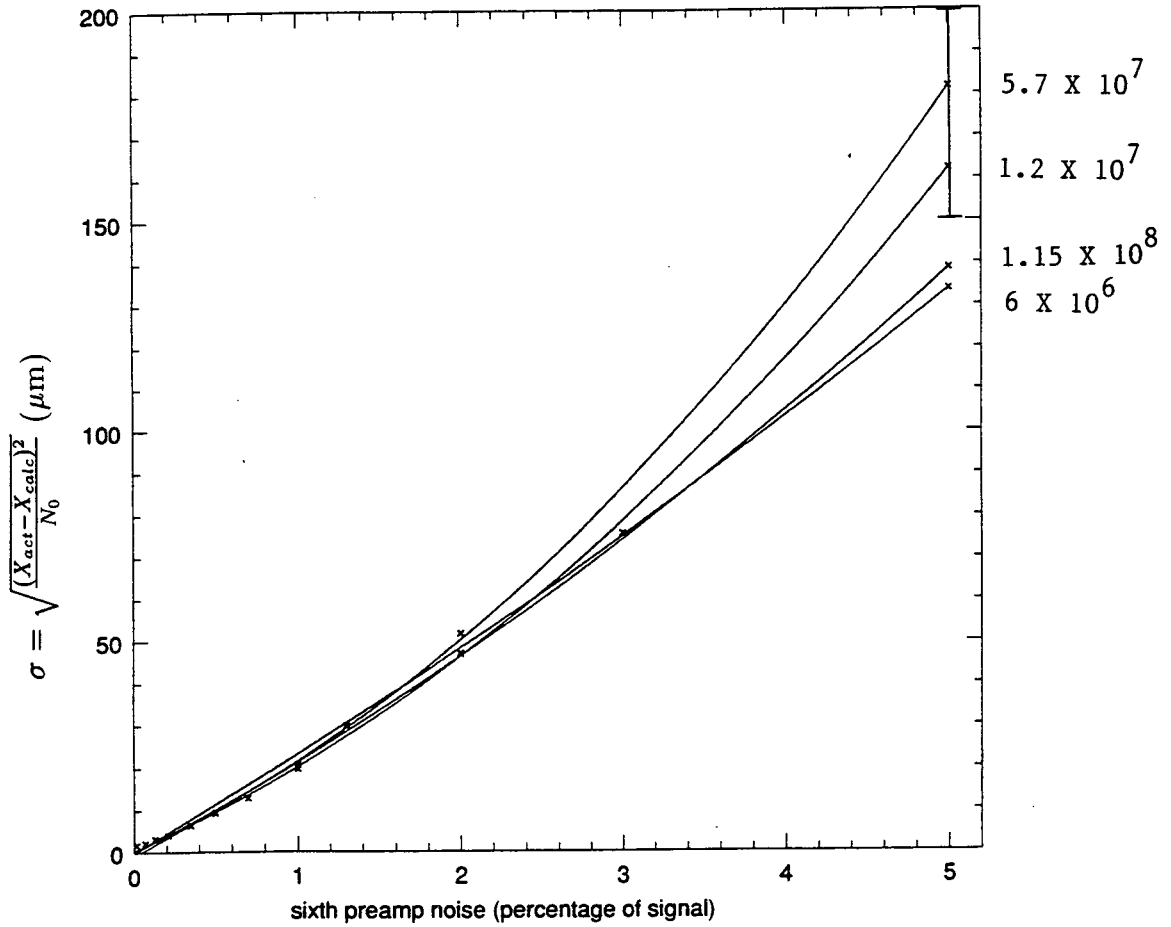
Figure 16 Plot of σ as a function of preamp noise expressed as a percentage of the total signal. Four different values for total signal are examined, ranging from $6\mathrm{x}10^6$ electrons to $1.15\mathrm{x}10^8$ electrons. The noise has been varied equally in all preamps.
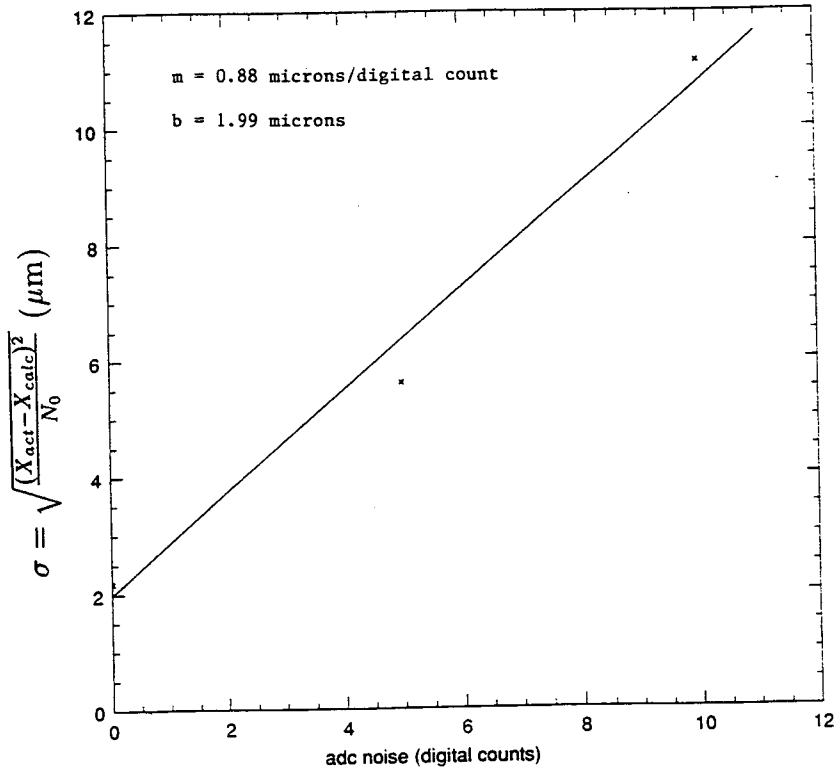
Figure 17 Plot of σ as a function of ADC noise in digital counts. The noise has been varied equally in all ADCs.
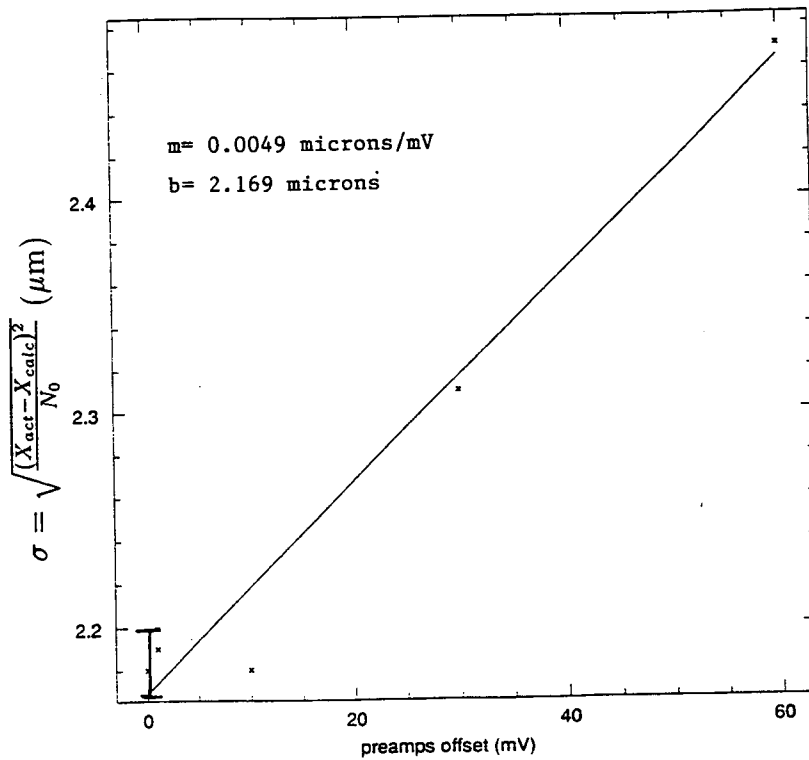
Figure 18 Plot of σ as a function of preamp offset in mV. The offset has been varied uniformly in all preamps.
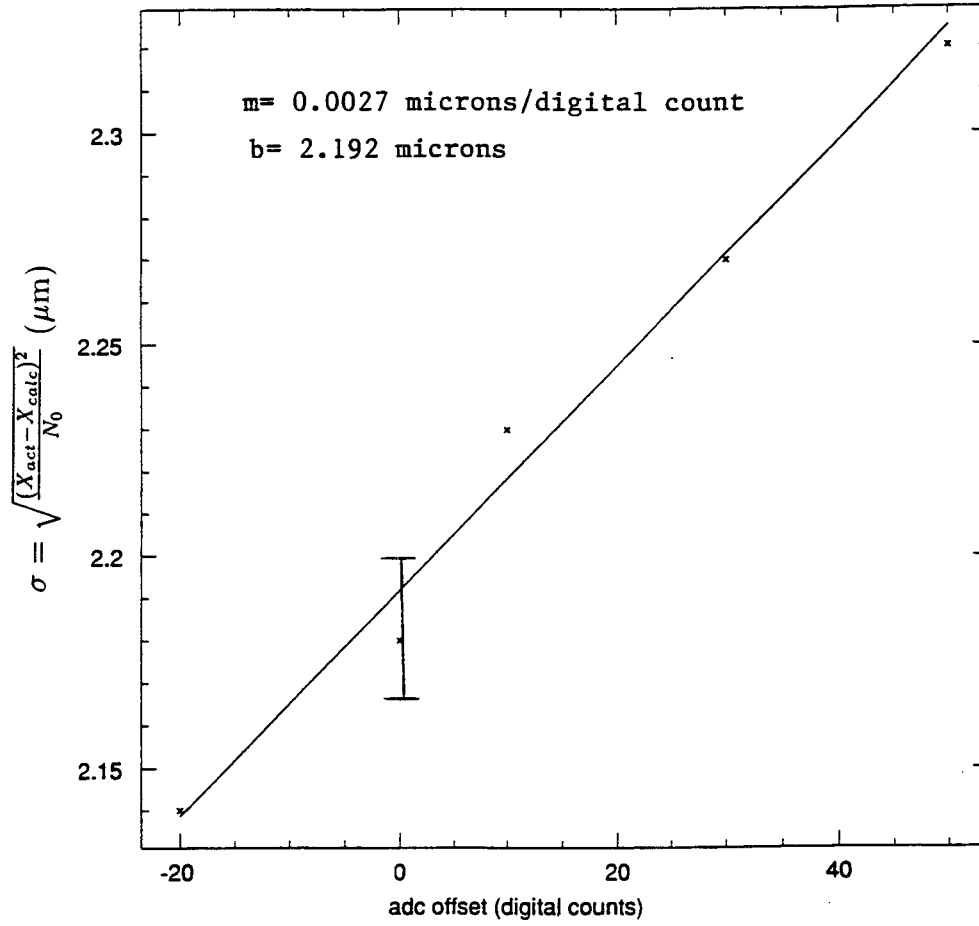
Figure 19 Plot of σ as a function of ADC offset in digital counts. The offset has been varied uniformly in all ADCs.
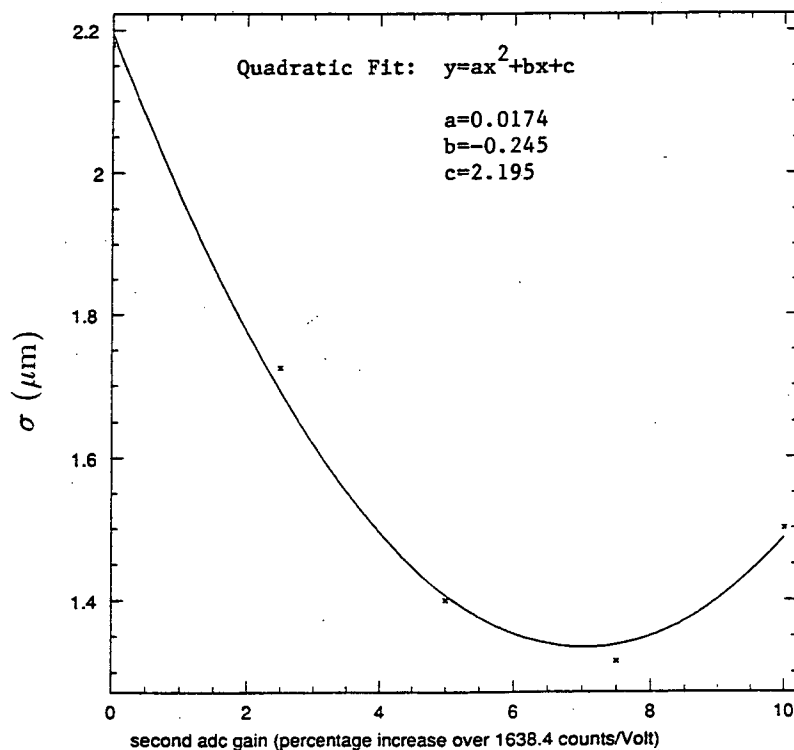
Figure 20 Plot of σ as a function of percentage increase in gain over its default value. Only the gain of the second ADC has been varied.
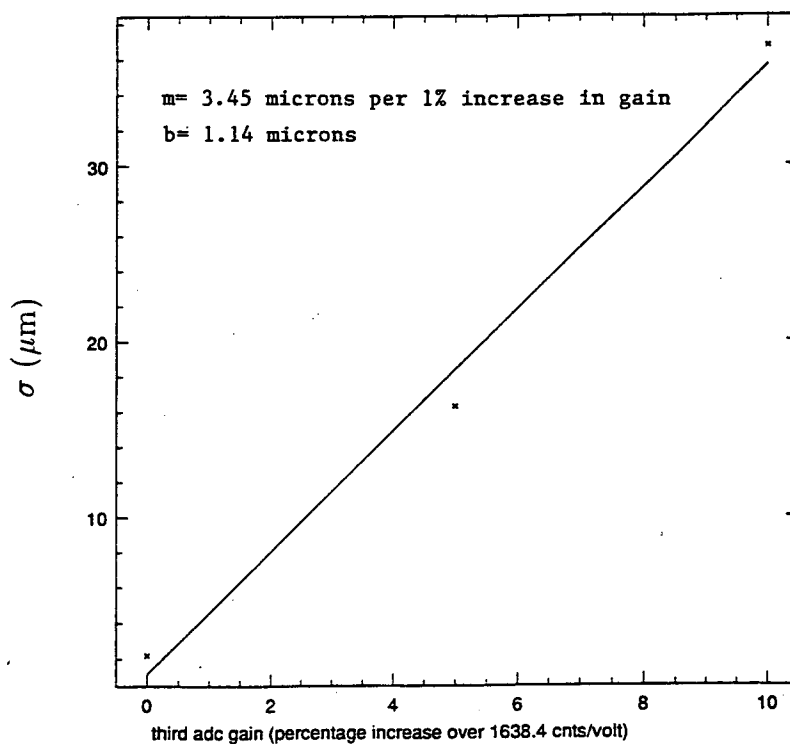
Figure 21 Plot of σ as a function of percentage increase in gain over its default value. Only the gain of the third ADC has been varied.
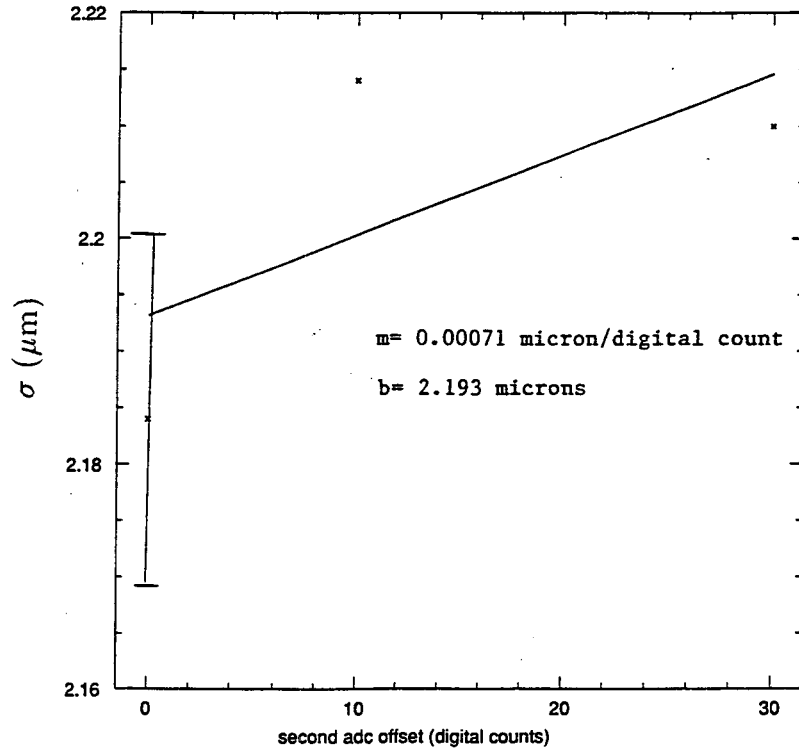
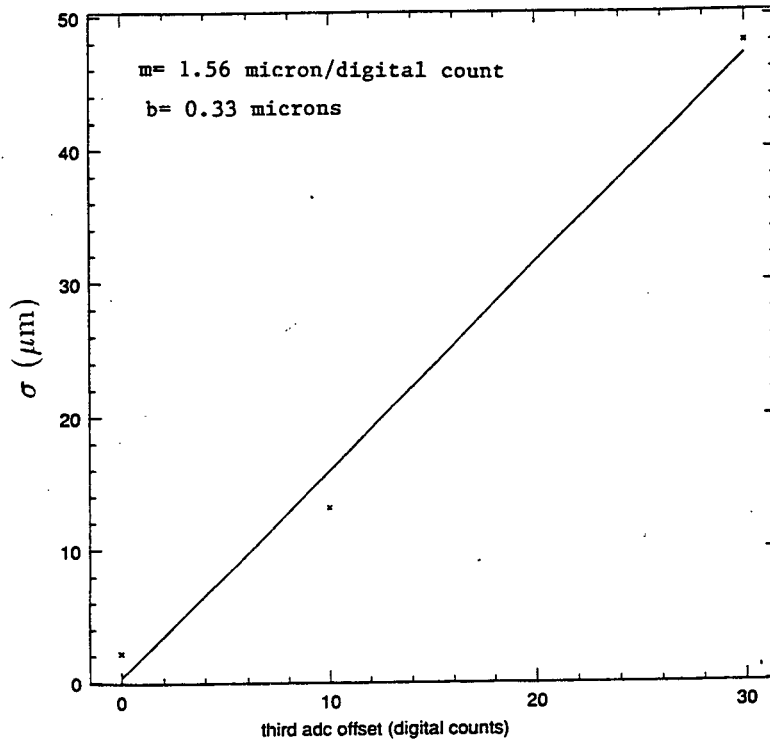**Figure 22** Plot of σ as a function of offset introduced in the second ADC.

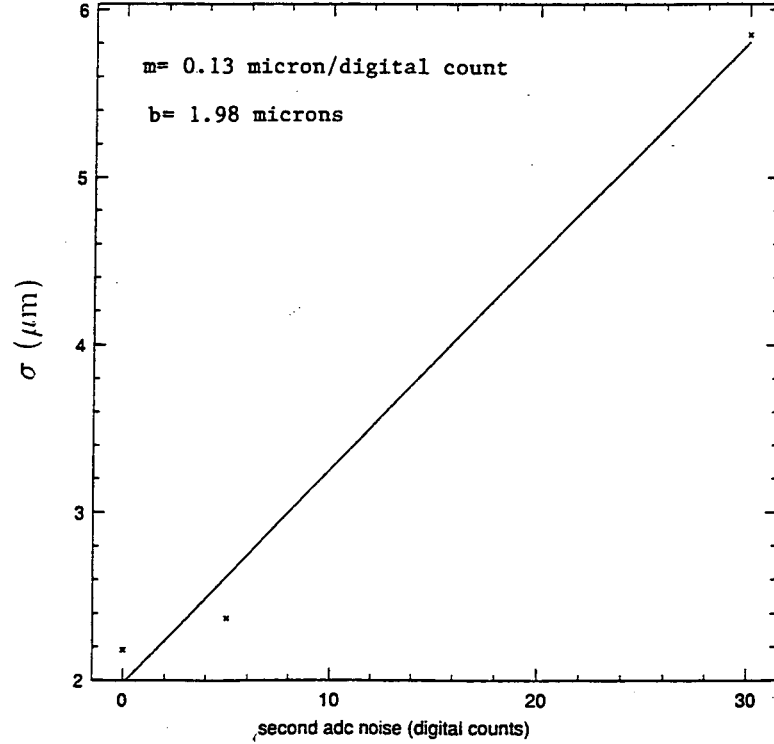**Figure 23** Plot of σ as a function of offset introduced in the third ADC.

Figure 24 Plot of σ as a function of noise in the second ADC.
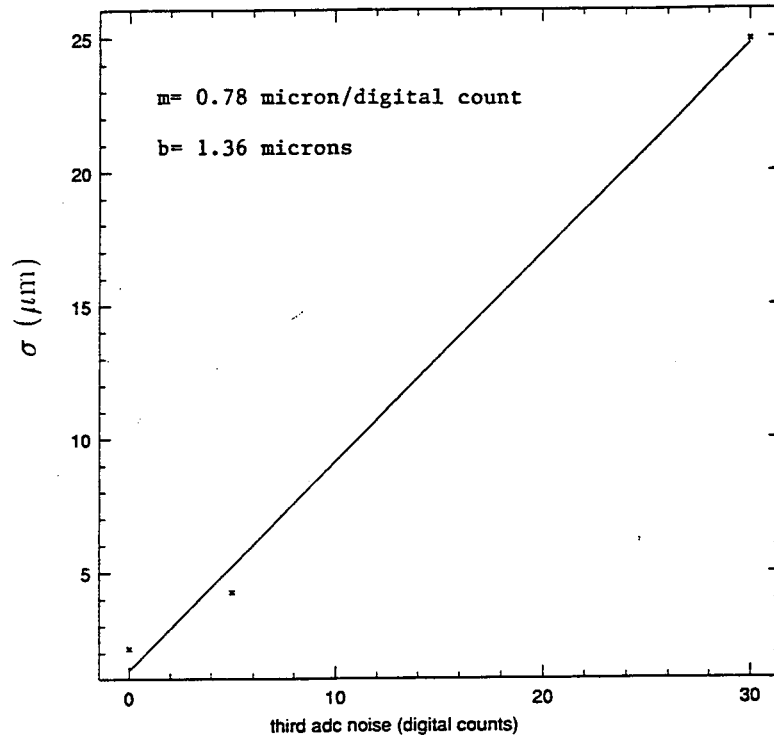

Figure 25 Plot of σ as a function of noise in the third ADC.

Figure 26 Plot of δ_{calc} as a function of true input position X_{act}. In this case, a 10-count offset has been introduced in the second ADC.

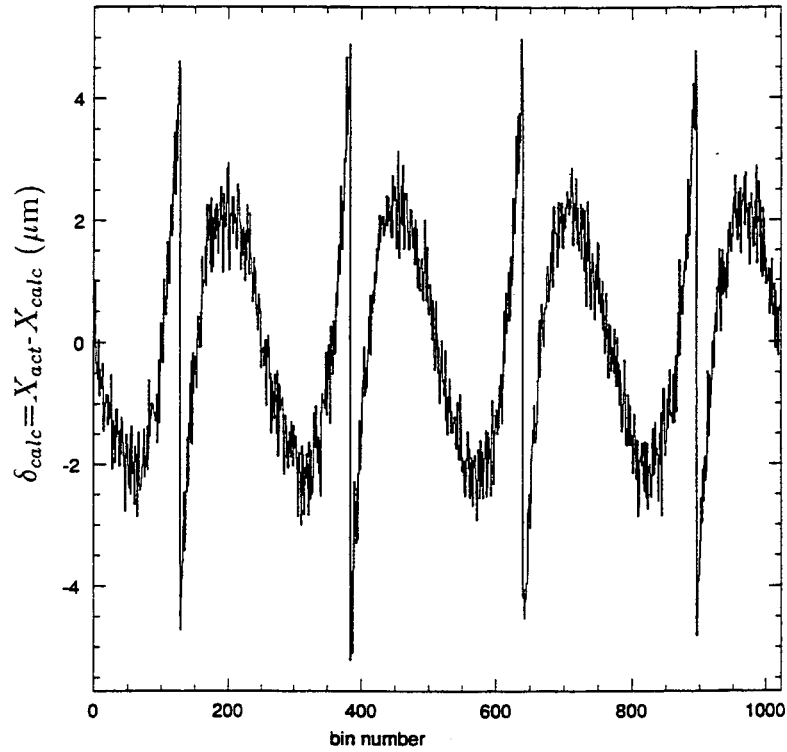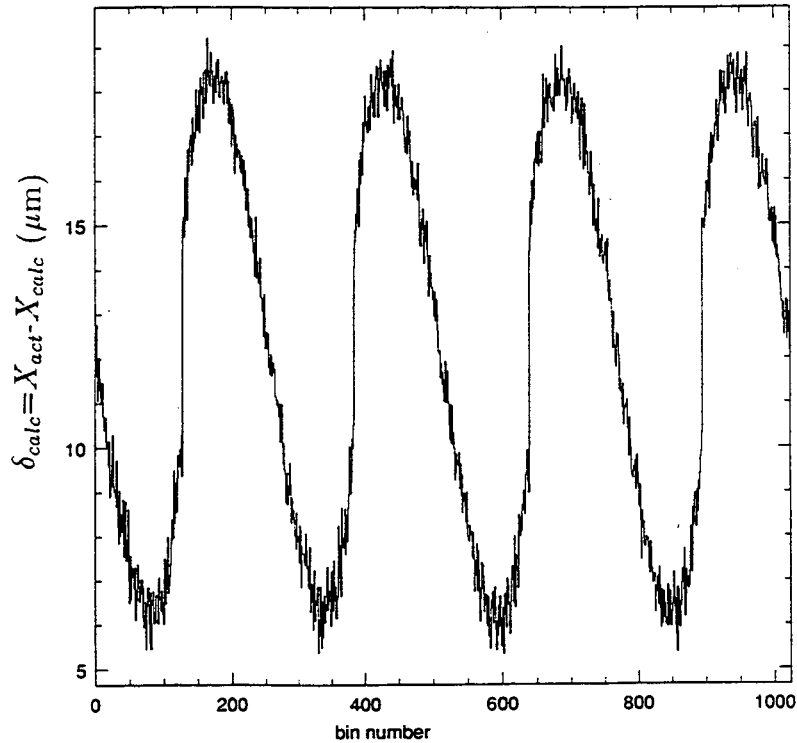**Figure 27** Plot of δ_{calc} as a function of true input position X_{act}. In this case, a 10-count offset has been introduced in the third ADC.
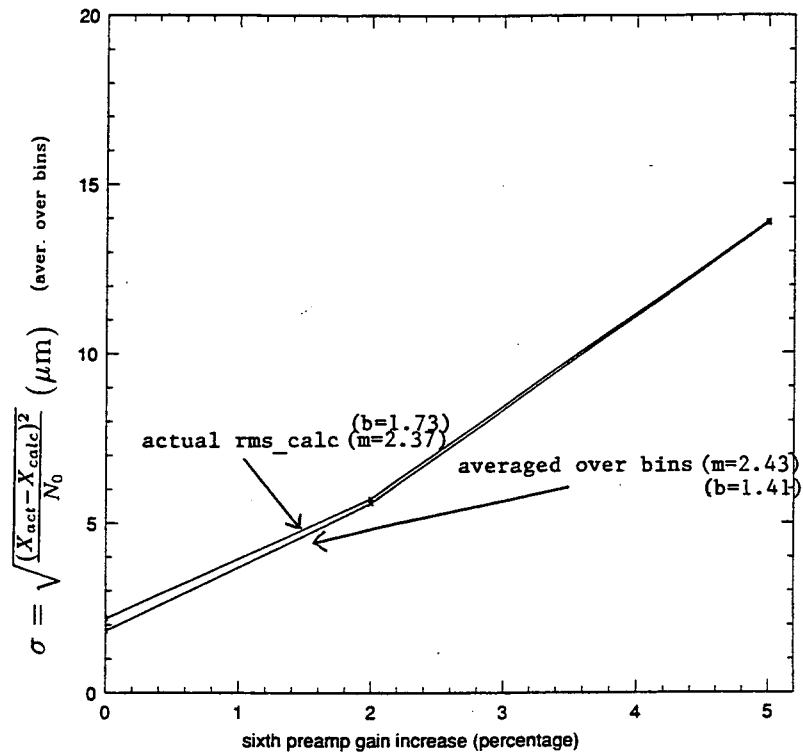
Figure 28 Illustration of two types of analysis. Top curve shows σ calculated event-by-event. Bottom curve shows σ obtained by using weighted average values in each bin. The differences in the results are insignificant.
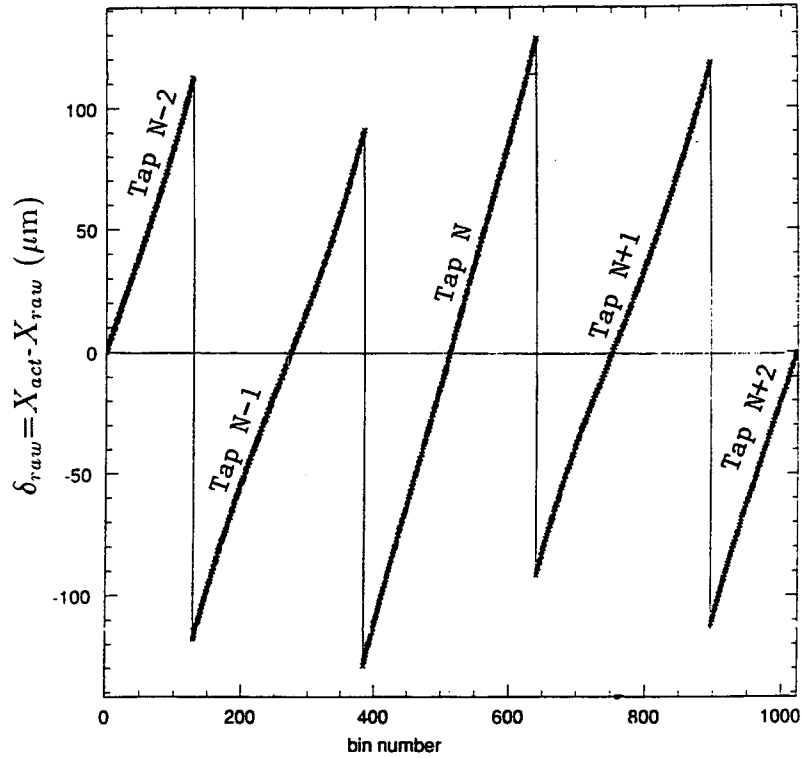
Figure 29 Plot of $\delta_{raw} = X_{act} - X_{raw}$ as a function of true input position X_{act} for a 5% increase in the gain of preamp #6.

Figure 30 Plot of $\delta_{raw} = X_{act} - X_{raw}$ as a function of true input position X_{act} for a 5% increase in the gain of preamp #5. Note that this plot can be obtained from Figure 29 by shifting the curve over one tap.

Figure 31 Plot of $\delta_{calc}=X_{act} - X_{calc}$ as a function of true input position X_{act} for a 5% increase in the gain of preamp #6.
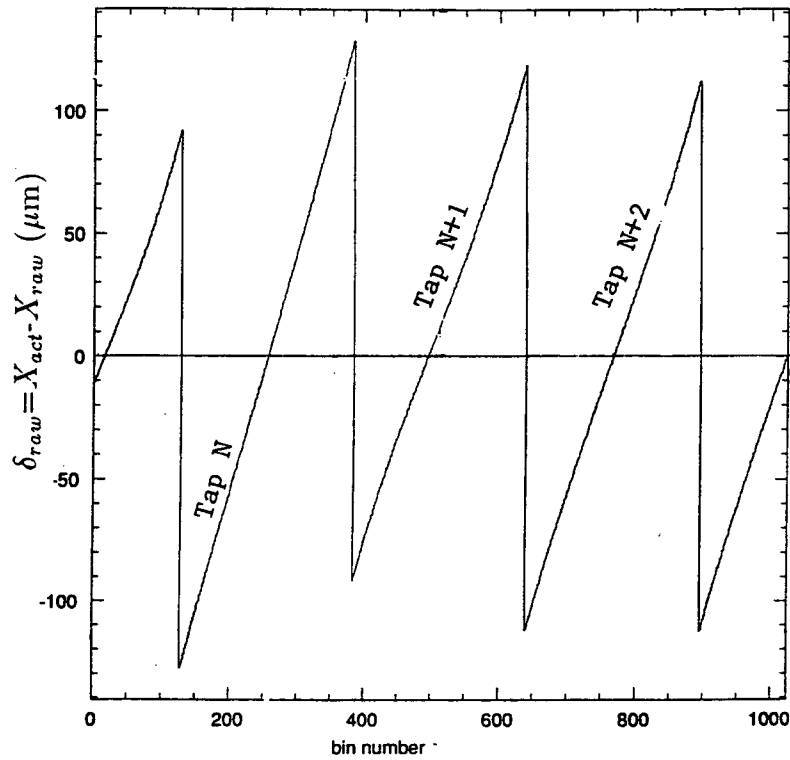

Figure 32 Plot of $\delta_{calc}=X_{act} - X_{calc}$ as a function of true input position X_{act} for a 5% increase in the gain of preamp #5. This shows similar behavior to that of Figure 31, except shifted by one tap.
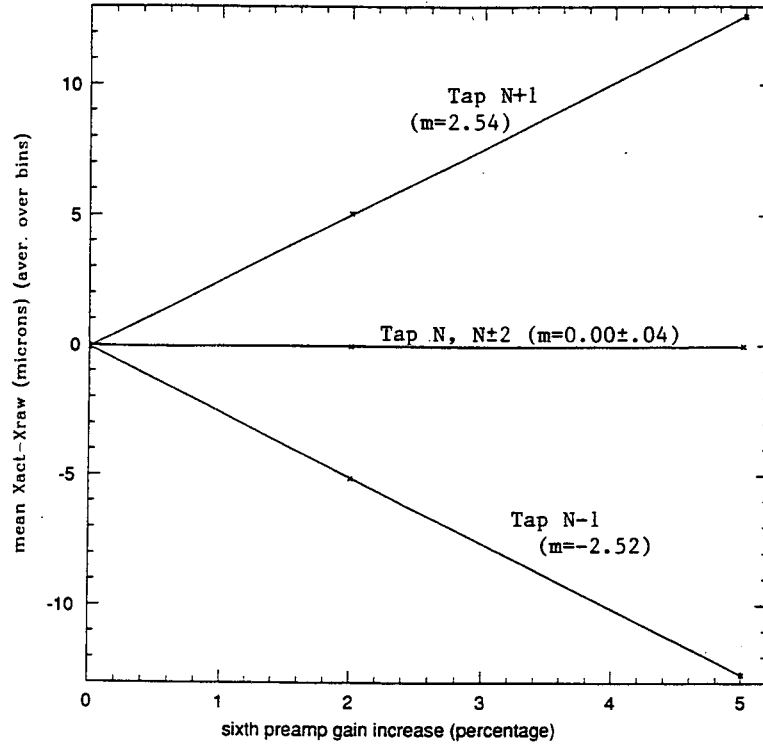
Figure 33 Mean value of δ_{raw} as a function of percentage increase in gain for preamp #6.
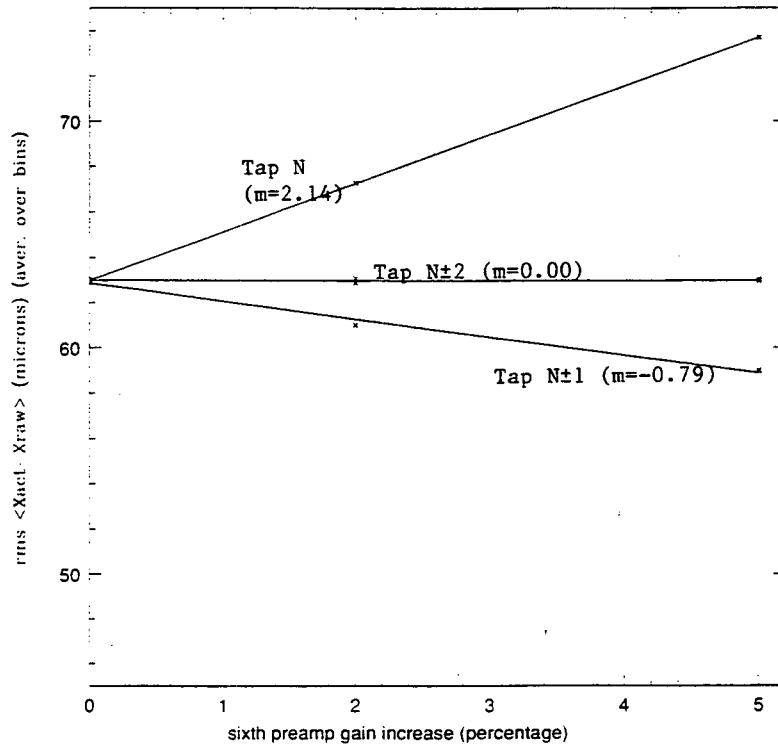
Figure 34 Rms value of δ_{raw} as a function of percentage increase in gain for preamp #6.
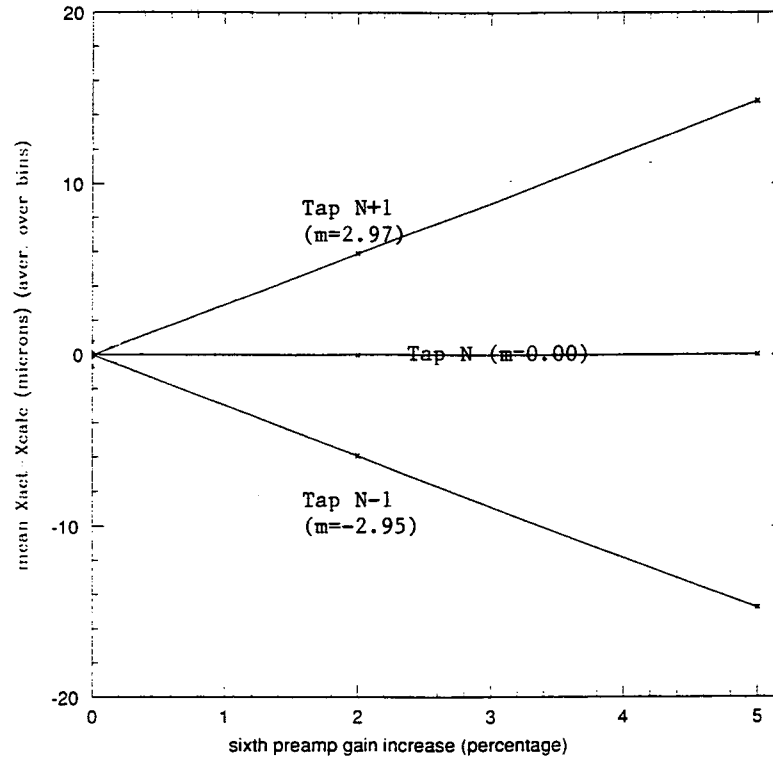
Figure 35 Mean value of δ_{calc} as a function of percentage increase in gain for preamp #6.
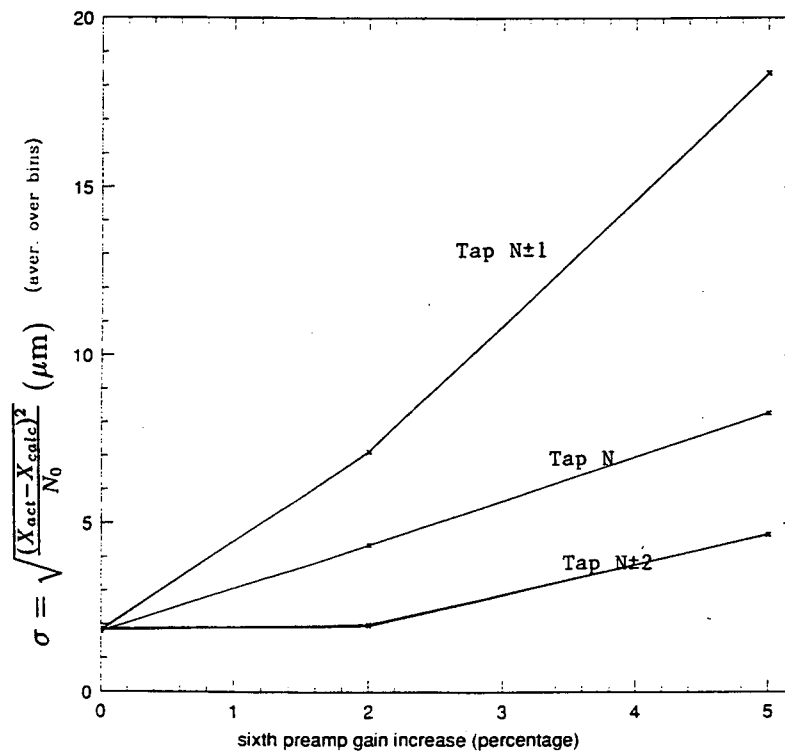
Figure 36 Rms value of δ_{calc} as a function of percentage increase in gain for preamp #6.
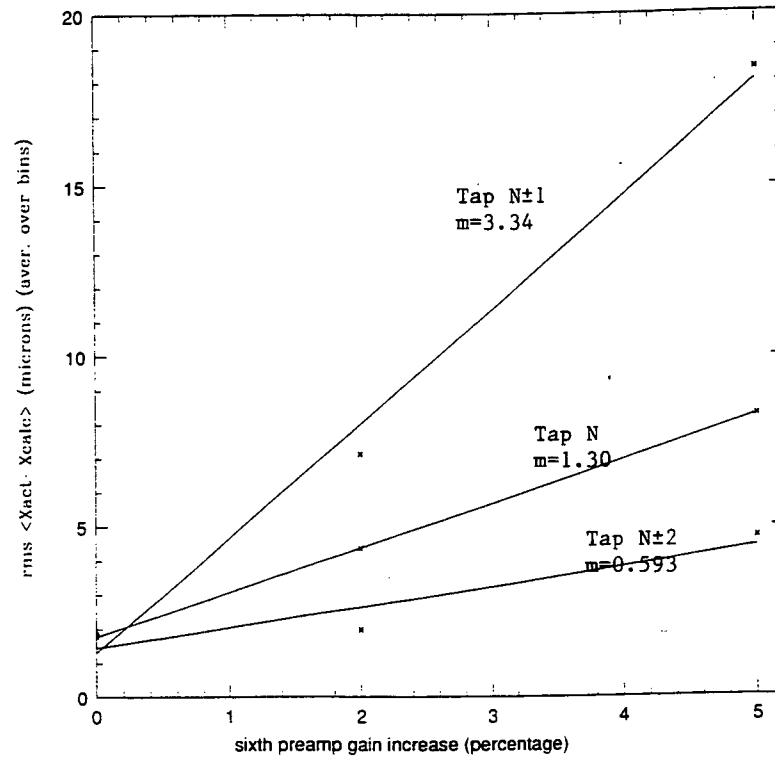
Figure 37 Same as Figure 36, except best-fit lines are also plotted.
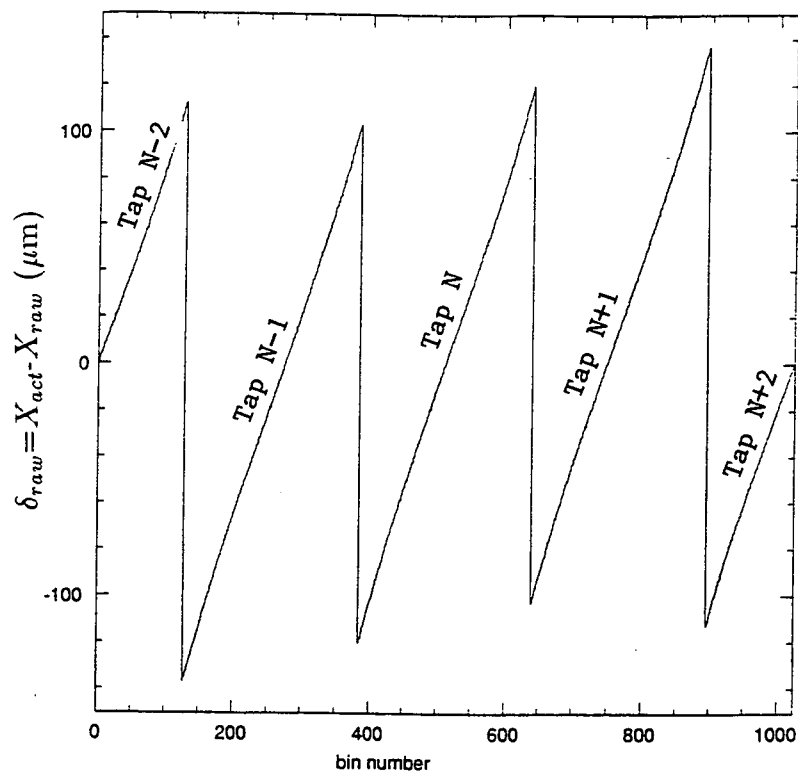
Figure 38 Plot of $\delta_{raw} = X_{act} - X_{raw}$ as a function of true input position X_{act} for a 10 mV offset introduced in preamp #6.
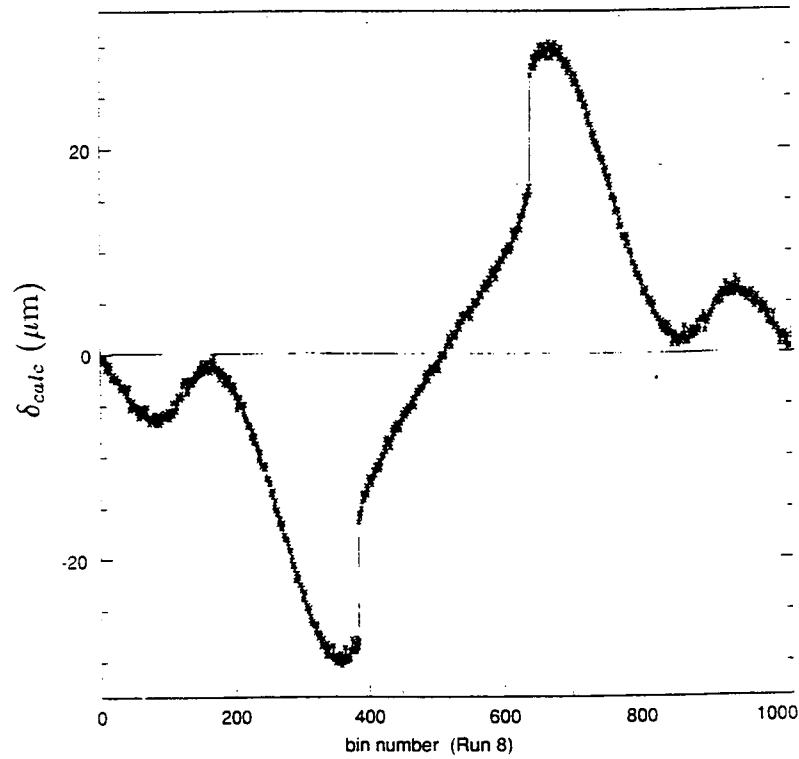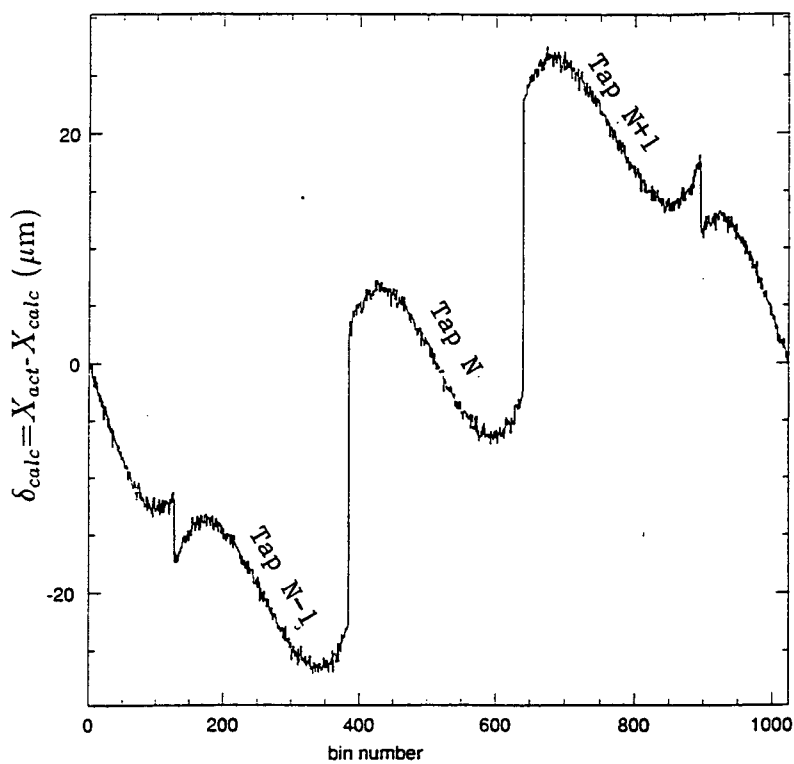

Figure 39 Plot of $\delta_{calc} = X_{act} - X_{calc}$ as a function of true input position X_{act} for a 10 mV offset introduced in preamp #6.
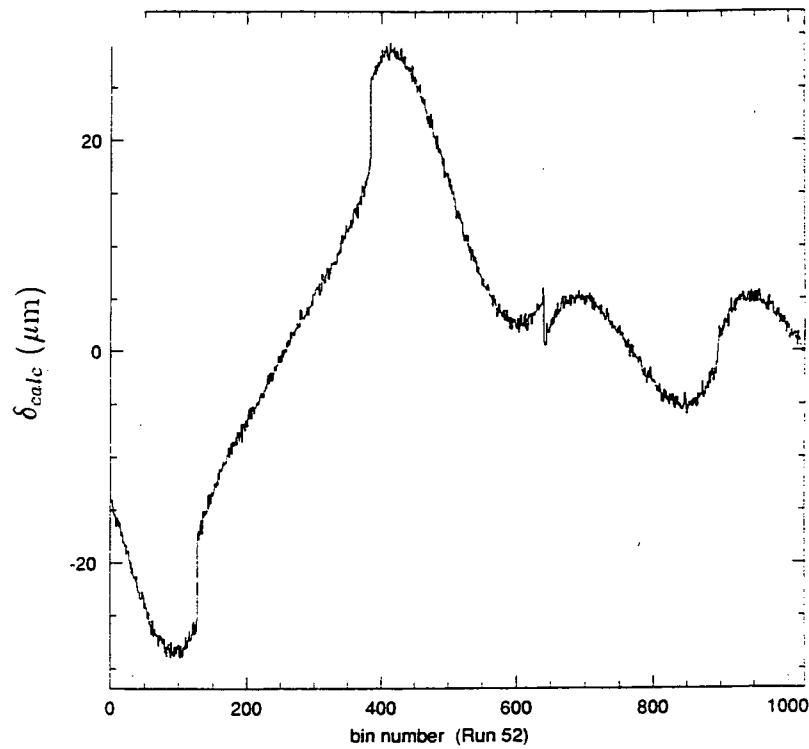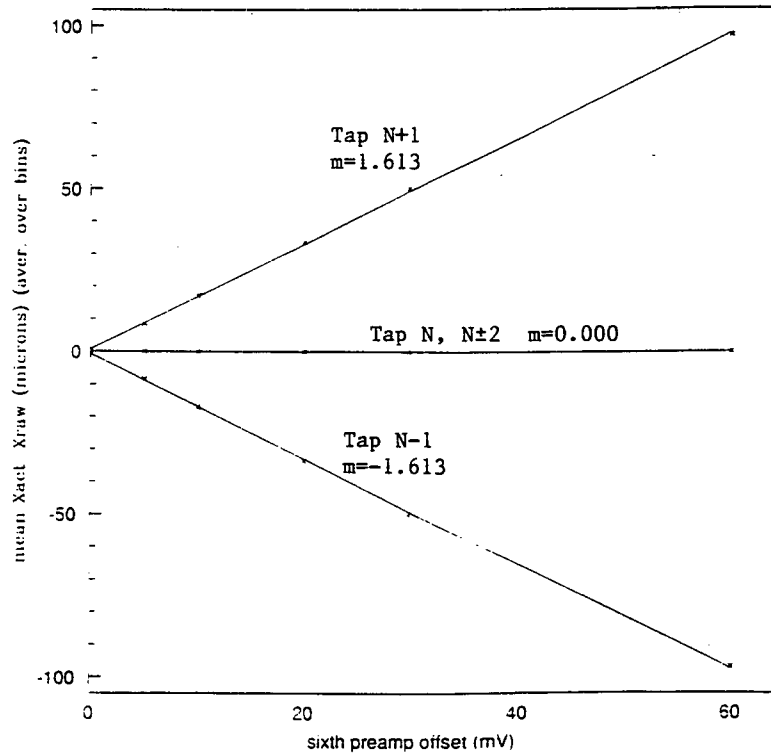
Figure 40 Mean value of δ_{raw} as a function of offset introduced in preamp #6.
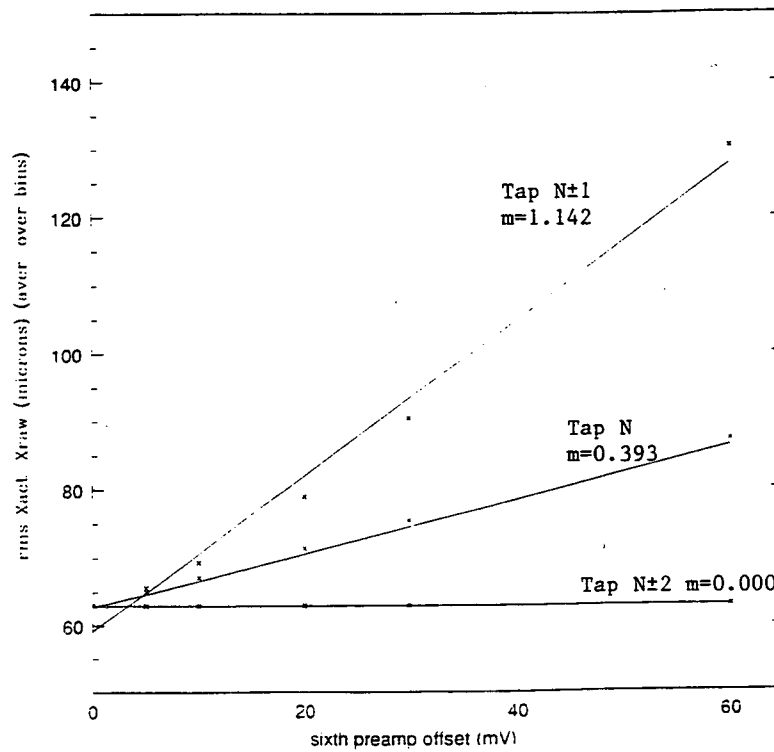
Figure 41 Rms value of δ_{raw} as a function of offset introduced in preamp #6.
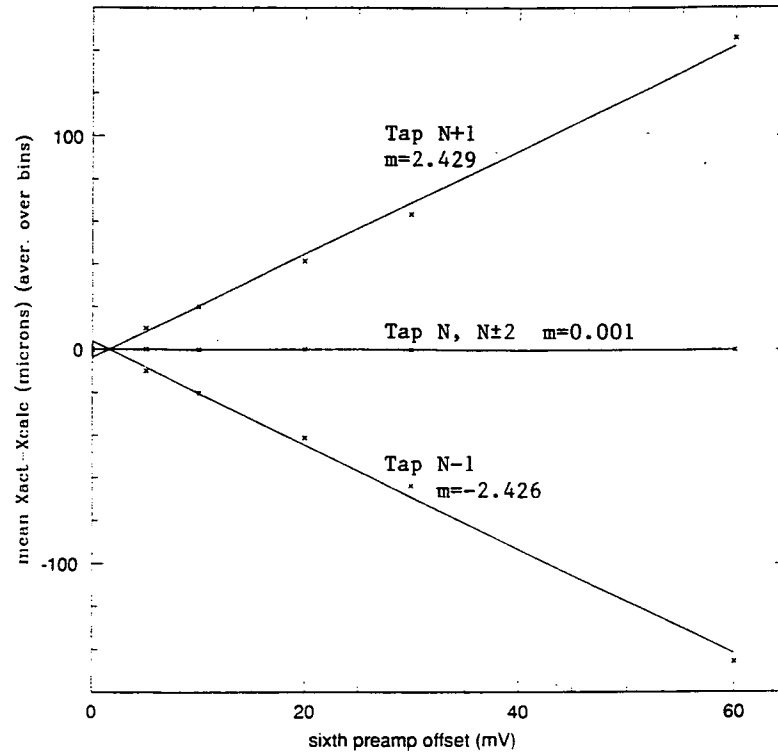
Figure 42 Mean value of δ_{calc} as a function of offset introduced in preamp #6.
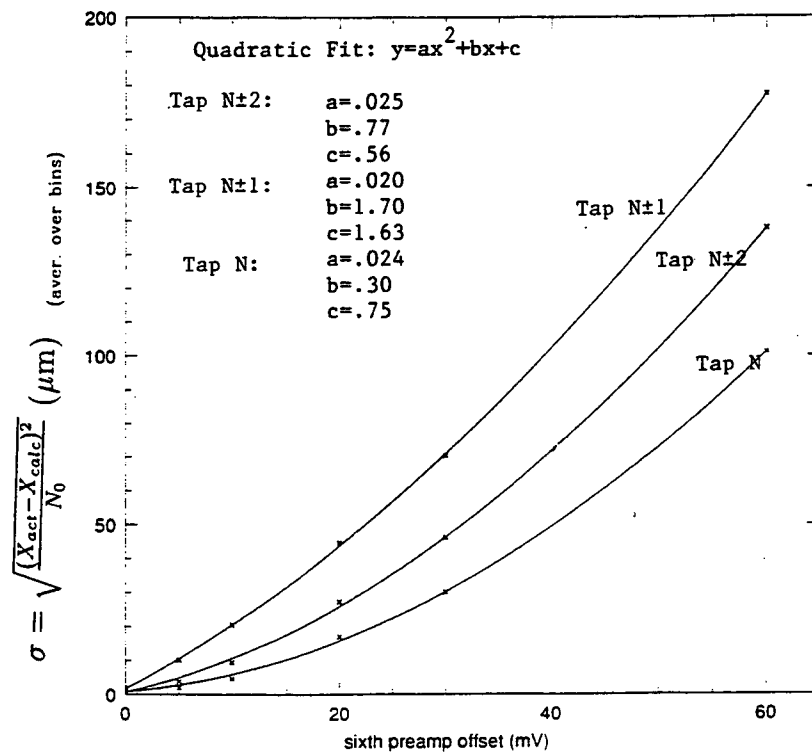
Figure 43 Rms value of δ_{calc} as a function of offset introduced in preamp #6.
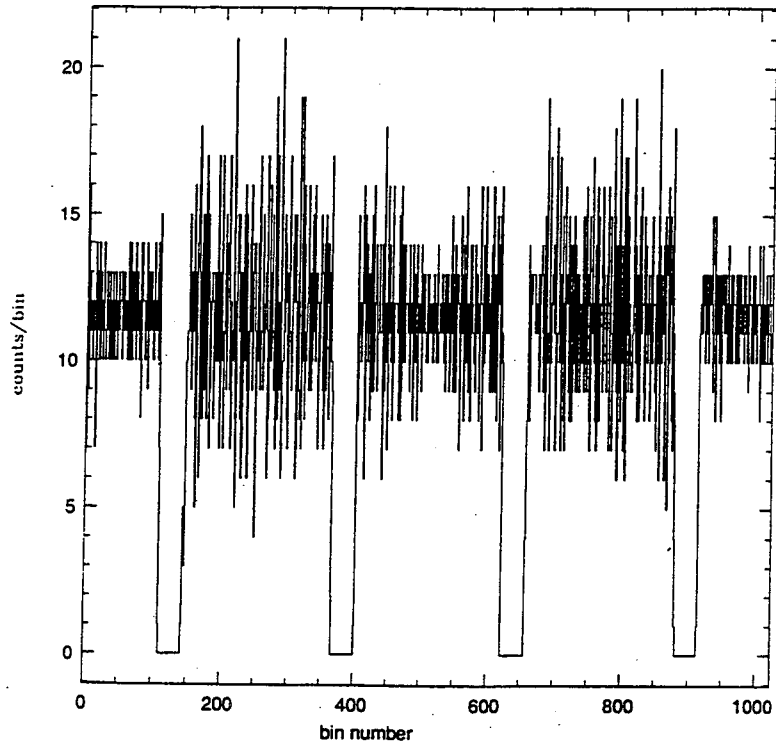
Figure 44 Histogram of input events as a function of X_{raw} to show gaps. The true input distribution (as a function of X_{act}) is uniform. Noise has been increased ten-fold in preamp #6 only.
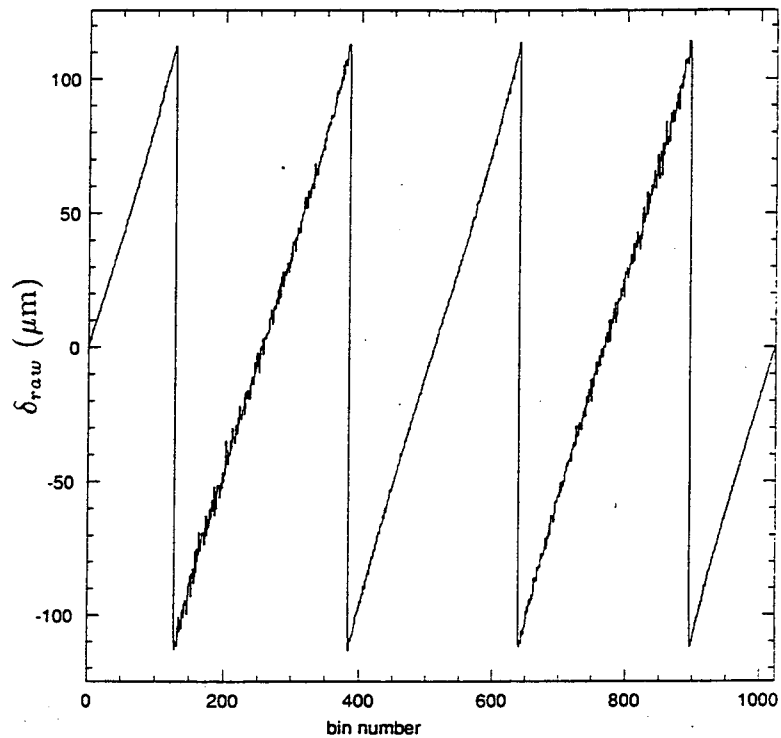
Figure 45 Plot of $\delta_{raw}=X_{act} - X_{raw}$ as a function of true input position, X_{act}. Noise has been increased by a factor of ten in preamp #6 only.
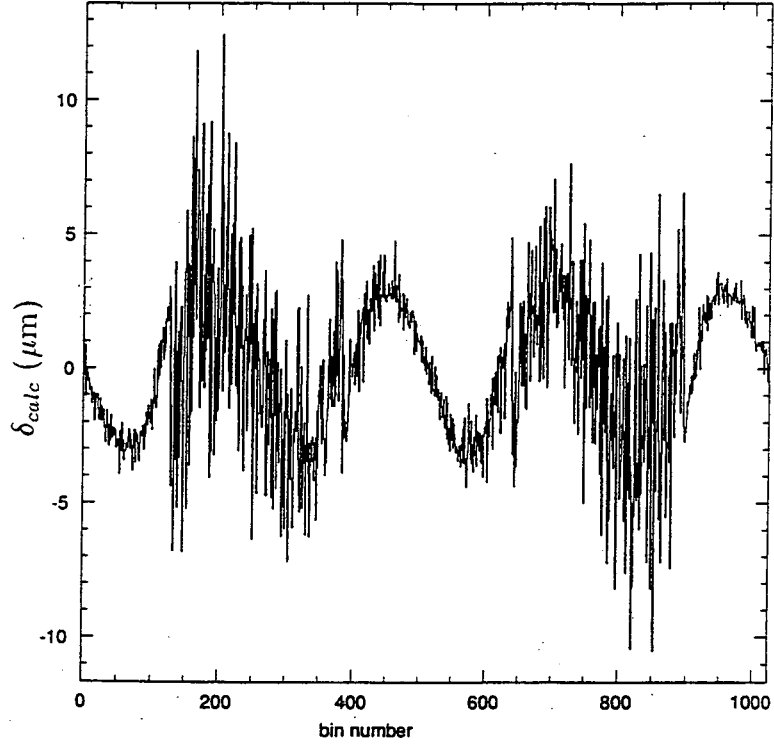
Figure 46 Plot of $\delta_{calc} = X_{act} - X_{calc}$ (after linear correction factor has been applied) as a function of true input position, X_{act}. Noise has been increased ten-fold in preamp #6 only.
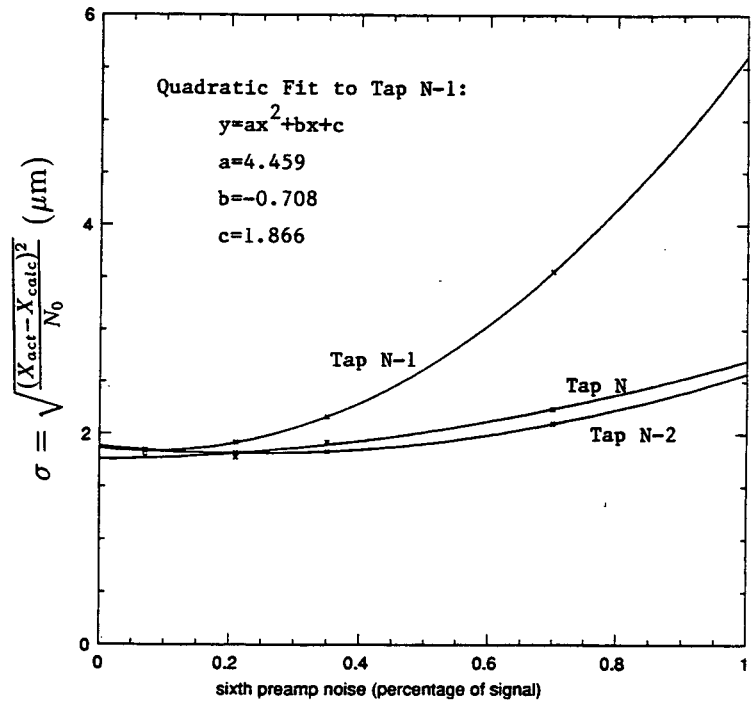
Figure 47 Plot of σ as a function of preamp noise expressed as a percentage of the total signal. The noise has been varied in preamp #6 only.
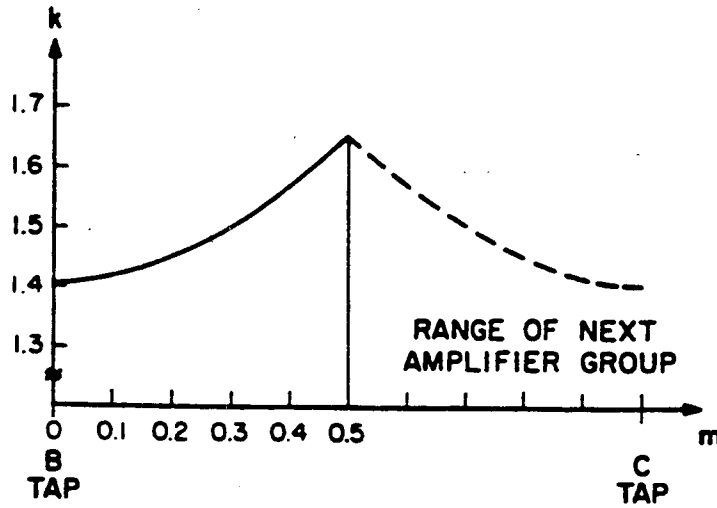
Figure 48 Noise factor, k, of a three-tap algorithm. Note that it reaches a maximum at the half-way point between taps. (Reproduced from Knapp.)
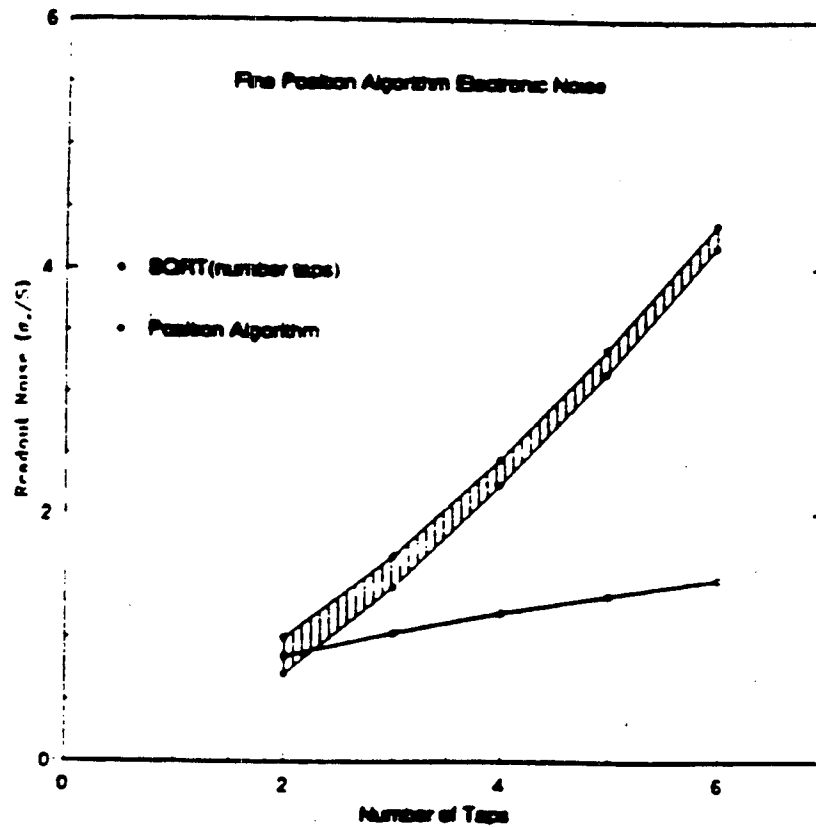
Figure 49 Electrical noise as a function of the number of taps in the algorithm. The hatched region depicts the range of variation associated with the minimum and maximum points in the noise factor,k, as seen in Figure 47 for the case of a three-tap algorithm. (Reproduced from Murray and Chappell, 1988.)

9   HRC Reports Pertaining to Modeling

Center for Astrophysics

MEMORANDUM

October 16, 1991

To: HRC science

From: K. Flanagan

Subject: Modeling

cc: J. Gomes

This memo is intended to document the results obtained with a first cut at the modeling of the HRC. In this memo I treat only the results obtained in varying the width of the charge cloud assuming a Gaussian§ distribution. No attempt has been made to include parameters (gain, offset and noise) for amplifiers or ADC's, and distributions other than Gaussian§ have not been considered.

1. I calculated the correction factor for *each event* generated by solving the following two equations simultaneously:

$$X_{true} = X_{cp} + b*X_{fp}$$

$$X_{calc}^{\S\S} = X_{cp} + X_{fp}$$

where X_{true} is the true input position from the model, X_{calc} the the raw calculated position using the three-tap algorithm (which leaves gaps), X_{cp} is the coarse position and X_{fp} is the fine position as determined by the three-tap algorithm (see Chappell and Murray, SPIE **1159**, 460 (1989)). The parameter b is the linear correction factor. Plots of the results are shown in Figures 1 and 2. It is evident that a single value for b is quite good

§: Erratum; This should read "Lorentz", not "Gaussian".

§§: Erratum; This should read "X_{raw}", not "X_{calc}".

over the whole range, except possibly near $X_{fp}=0$. (However, b seems to be symmetrically distributed about the mean there, and division by X_{fp} would naturally result in the large scatter of values seen near $X_{fp}=0$.) Thus, we can expect a single constant correction factor to provide a fairly good result.

A single linear correction factor was applied and the positions were recalculated. The root mean square difference between the true position and the calculated position was used as a figure of merit to gauge the effect of different correction factors, i.e.

$$\sigma = \sqrt{\frac{(X_{true} - X_{calc})^2}{N}}$$

As shown in Figure 3, σ has a well defined minimum and varies linearly with the correction factor outside this region. This region of minimum σ is enlarged in Figure 4. The mean (1.1539) of the individual correction factors plotted in Figure 2 did *not* represent the optimum case (i.e σ was 22.1 % higher). This can be understood by careful inspection of Figures 1 and 2, where it can be seen that the appropriate correction factor increases slightly toward the half-tap positions, the point of greatest discrepancy between true position and calculated position. Alternatively, by weighting the individual correction factors according to a normalized value of $(X_{true} - X_{calc})^2$, a very close estimate (1.1581) of the optimum correction factor (1.1577) is found. (In this case, the correction factor differed by .03% and σ was .24% higher relative to the optimum case.) Therefore, I have considered this technique adequate for establishing the appropriate correction factor without resorting to an iterative search.

2. For the simple case considered here, the model generates equal gap widths, no matter which particular gap is examined. Thus, it was necessary to examine only one gap in detail for each charge cloud distribution modeled. The data below reflect the results.

3. The gap edges are found (as expected) to be located according to

edge = ±.5 (gap width) + (gap center)

Since the gap centers are known and edge locations are well defined by the gap width for this simplified model, *the gap width and the location of either gap edge constitute equivalent parameters.*

4. The gap width is linearly related to the width of the charge cloud distribution, as shown in **Figure 5**.

5. The correction factor as a function of gap width in bins is shown in **Figure 6**. The best linear fit to the function is given by:

corfac = 0.005446 * (gap width in bins) + 0.9655

This will predict the correction factor to better than 1.2% (0.0124) over the range shown, corresponding to an error of 0.7% (or 0.009 microns) in the predicted rms value of $X_{true} - X_{calc}$ (i.e., σ as defined above).

6. The rms value of $X_{true} - X_{calc}$ as a function of gap width is shown in **Figure 7**. The best linear fit to the data is given by

rms (microns) = .0435 * (gap width in bins) + .602

This fit will predict the rms to better than 0.1 micron (better than 7%). Since the largest value of σ is less than 4 microns, it seems that a linear correction is sufficient, and there is no need to go to higher order corrections. We may want to consider using the maximum value of $X_{true} - X_{calc}$ instead of the rms value.

CONCLUSIONS

A linear correction appears to give adequate (a few microns) adjustment to the cal-

culated event positions without resorting to higher order corrections. The appropriate correction factor can be directly obtained from the gap width (or the edge position), and from this gap parameter the rms error in the position correction can also be predicted.
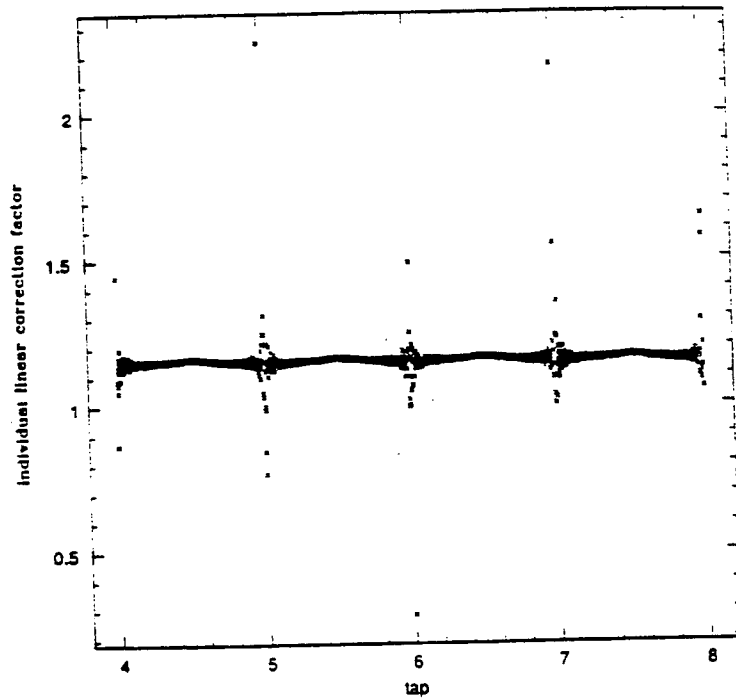
Figure 1
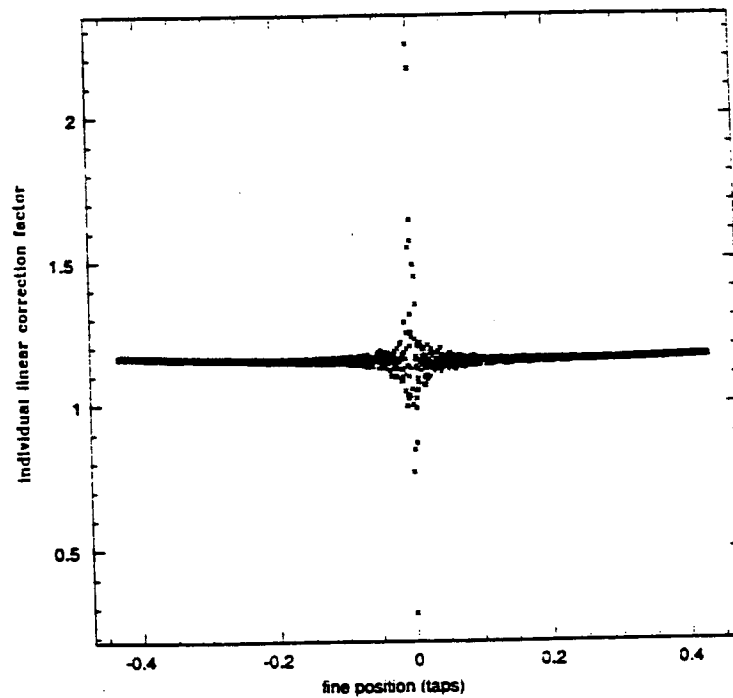
Figure 2
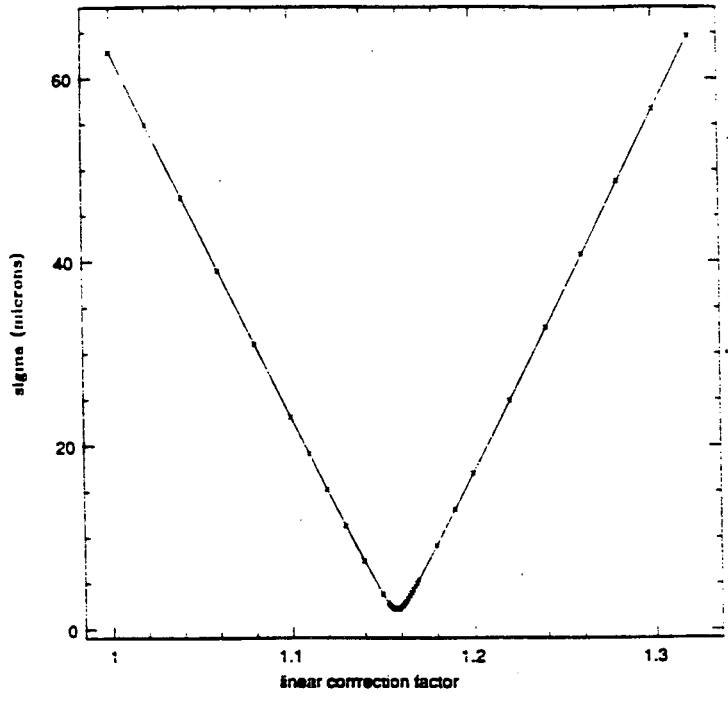
Figure 3
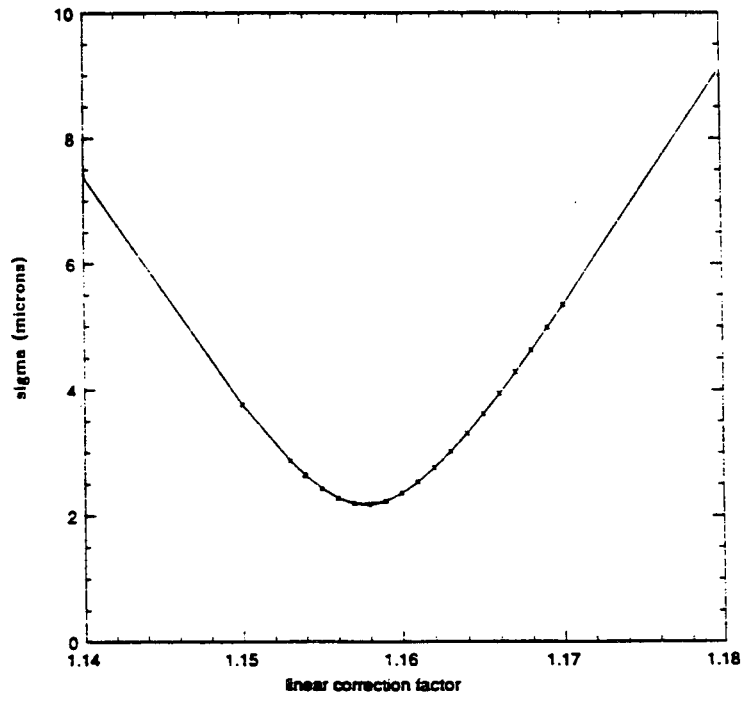
Figure 4
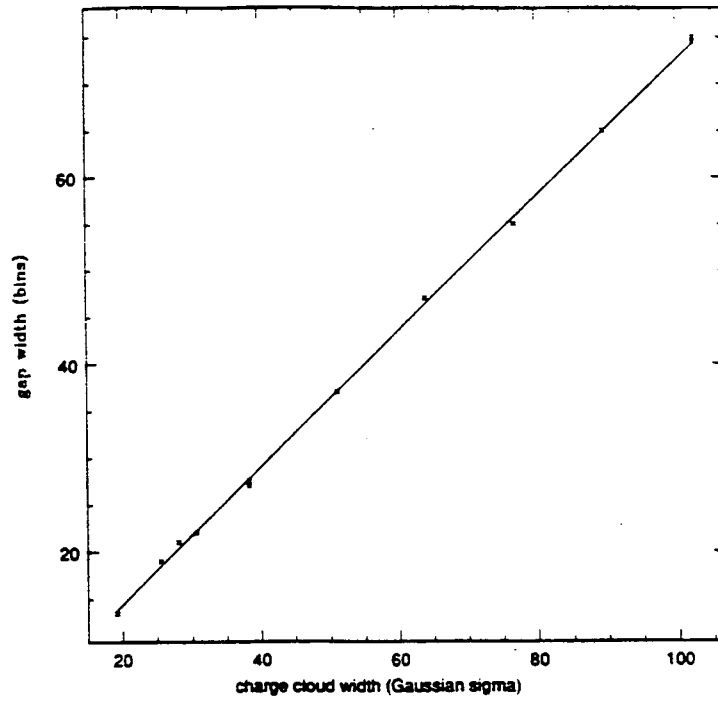
Figure 5
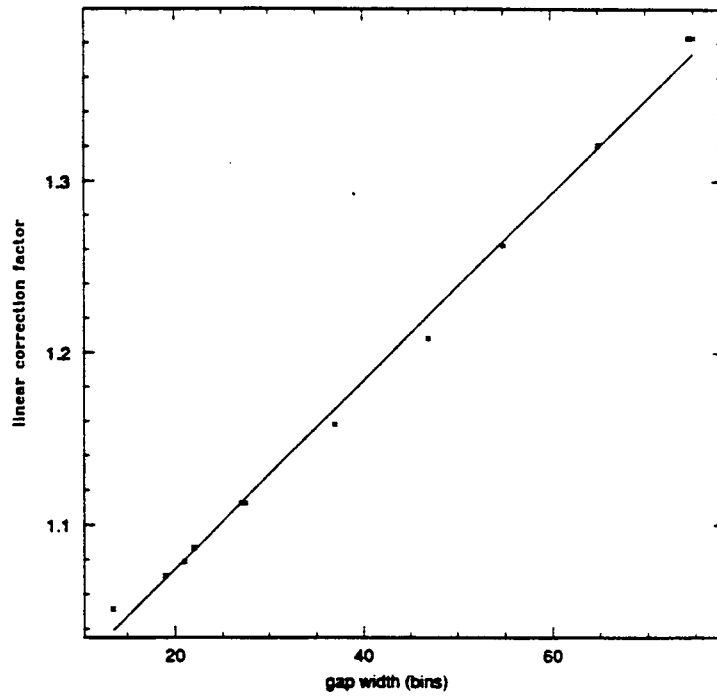
Figure 6
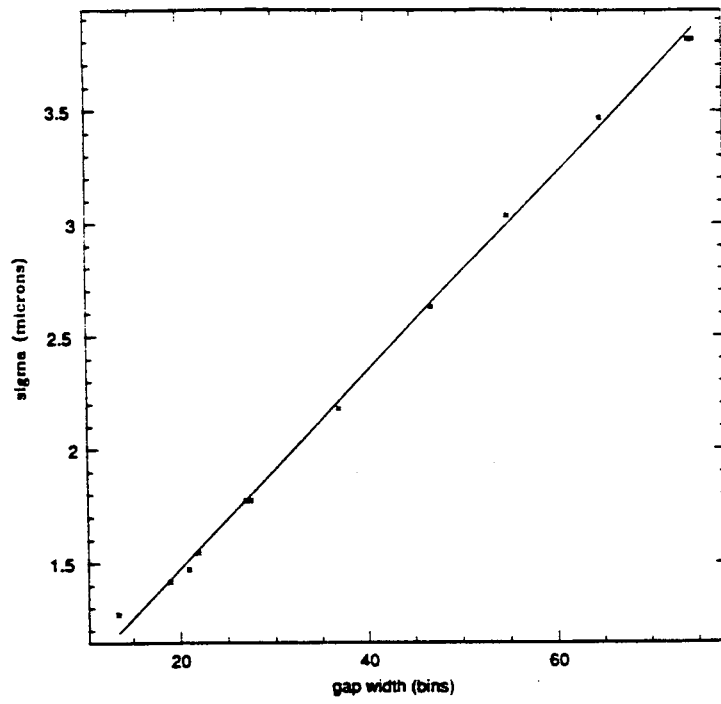
Figure 7

Center for Astrophysics

MEMORANDUM

February 11, 1992

To: M. Zombeck

From: K. Flanagan

Subject: HRC Modeling Update

cc: K. Daigle

This memo is an update on some of the modeling results since October. These results should be viewed as preliminary.

The modeling at this point examines the effect of three parameters on two components of the electronics. The three parameters are: gain, offset and noise. The two components are the preamps and the adc's. There is one preamp associated with each tap, and there are three adc's. In our 'three-tap algorithm', we engage all three adc's in detecting an event: the three adc's are assigned to the three taps involved in the algorithm. The center tap is that associated with the largest charge (voltage) collected (i.e., the 'coarse position'). The two taps to either side are involved in determination of the fine position. A single linear correction factor is assigned to multiply the fine position, and a final position X_{calc} is calculated. If we define δ as the difference between the true or actual input position (X_{act}) and the final calculated position (X_{calc}) (i.e., $\delta = X_{act} - X_{calc}$), then a useful figure of merit is σ, the rms value of δ:

$$\sigma = \sqrt{\frac{(X_{true} - X_{calc})^2}{N}}$$

This figure of merit σ is discussed below. In addition, some remarks about the effects on the gap width and placement will be made.

I. Varying parameters for ALL preamps or adcs:

1. Varying (equally) all gains of all preamps, or of all adcs, had no effect (as expected).

2. Increasing noise in all preamps or in all adcs increased σ. The gaps didn't change in placement or width.

3. Increasing the offset in all preamps or all adcs increased the gap width and (only slightly) increased σ. The gaps did not move when the offsets of all preamps were varied.

II. Varying CENTER ADC

1. Increasing gain increased the gap width. and *decreased* σ. This is understood because the fine position is calculated according to X_{fp}=A-C/(A+B+C), where B refers to the signal of the center adc. Gaps did not shift.

2. Increasing offset increased the gap width but didn't affect gap placement, which is to be expected because the adc involved is the "symmetric" one. The figure of merit, σ, increased.

3. Increasing noise did not affect the gaps, but did increase σ.

III. Varying ADC number three (ADC to the right side).

1. Increasing gain *decreased* the gap width and "moved" the gap to the left (i.e., both sides of the gap move by unequal amounts). The figure of merit σ increased.

2. Increasing offset increased the gap width and moved the gap to the left. σ increased.

3. Increasing the noise had a very slight effect on the gaps, and increased σ.

4. Varying a single adc in general produced symmetric results in plots of δ vs input position. so that at no single tap was the effect different than at any other. This is an advantage arising from the fact that all three adc's are involved in calculating the position (and obtaining δ and σ), no matter where the initial event arrives. In the above cases, however, all the preamps were identical in all respects including noise, which was fixed at 7×10^{-4} volts rms. (The total charge generated for each input event was 1.2×10^7 electrons.)

IV. Varying a single preamp

1. Varying a single preamp introduces assymetries in the curve of δ vs input position. This more complicated case is presently under investigation.

In the cases above, the following ranges of variation were tested.

- Preamp Noise: up to factor of 10; default value is $7x10^{-4}$ volts

- Preamp Offset: up to 60 mV;default value is 0 ($\pm$ 1mv)

- Preamp Gain: up to 10% increase; default value is $8.7x10^{-8}$ ($\pm$ .5%)

- ADC Noise: up to 30 digital counts; default value is 0

- ADC Offset: up to 30 digital counts; default value is 0 ($\pm$ 1mv=1.6 counts)

- ADC Gain: up to 10% increase; default value is 1638.4 ($\pm$ .5%)

IMMEDIATE AREAS OF INVESTIGATION:

Three areas of investigation are under way; (1) understanding that gap changes are as expected (and can be predicted), (2) deriving the numerical estimates of what percentage change occurs in σ given a 1% change in any individual parameter, (3) modifying the range of variation to reflect real ranges (already suggested by engineering) and identifying the most likely areas of improvement.

Center for Astrophysics

Harvard College Observatory

Smithsonian Astrophysical Observatory

60 Garden Street. Cambridge. MA 02138

Memorandum

From: J. Chappell

Phone: 617 495-7140

FAX: 617 495-7356

e-mail: jhc@cfa.harvard.edu

To: HRC Science Distribution

Date: May 27. 1992

Subject: CGCD model V2.0

File: 091191.1.tex

Cc: Jack Gomes

I have just finished the first cut at a modeling program for the crossed grid charge detector (CGCD). This memo describes the use and limitations of this first model.

1. The Model

    In summary. an electron charge cloud form the MCP is collected on a one-dimensional grid of wires. The charge is resistively divided between the grid taps. Each amplifier tap is characterized by a gain. offset. and noise figure. The three ADC's are characterized in the same mannor. A more complete description of the modeling can be found in two papers published in SPIE (ref...).

2. The Command Line

    The CGCD model is invoked with the following syntax:

```
$ cgcd < mcp_events > cgcd_events
```

    In this version. the program accepts one-dimensional 'MCP-events' from stdin. A MCP-event is characterised by four numbers. the event number. the y-position. the standard deviation of the charge distribution. and the total number of electrons in the exiting charge cloud.

```
0.000000e+00    5.407183e+00    2.000000e-01    1.200000e+07
1.000000e+00    4.224508e+00    2.000000e-01    1.200000e+07
2.000000e+00    4.774785e+00    2.000000e-01    1.200000e+07
3.000000e+00    6.396198e+00    2.000000e-01    1.200000e+07
4.000000e+00    4.310660e+00    2.000000e-01    1.200000e+07
```

Each ascii field of the mcp_event is seperated by a white space(s).

3. Command Line Parameters

Runtime parameters can be supplied to the program using switches on the command line.

```
usage: cgcd -[nlpaDv] < mcp_events
        n - number of taps to be used [12]
        l - distribution type [gau]
        p - preamp file name [preamps]
        a - adc    file name [adcs]
        D - Debug Level [0.00]
        v - SCCS Version Level
```

The -n switch selects the number of taps to be used in the model. The default is 12. The larger the number tends to increase the runtime of the model. N should be 8 taps more than the number of taps you model. This means if your y- input positions run from taps 4-8. N should be 0-12. The -l switch seleects the charge cloud dristribution type. Version 2.0 only supports a Gaussian distribution. The later versions will support Lorentz. triangle. and skewed Gaussians. The -p switch sets the file name that contains the preamplifier parameters. The -a switch selects the file name that contains the ADC operational parameters. The -D switch sets various debug levels. Increasing the debug level will cause the program to print more about the internal calculations. The debug output is directed to stderr. The -v switch prints the current SCCS version number. Since the program will change over time. it's a good idea to verify the version number of the program.

4. Preamplifier Characterizations

Each preamplifier is characterized by three parameters. the amplifer gain $m(volts/electron)$, the amplifier offset $b(volts)$. and a noise figure $vn(rms - volts)$. The output voltage on the i-th tap is defined by:

$$V_i = m_i Q_i + b_i + f(vn_i) \tag{1}$$

The nominal gain m value is $8.7E-8$ V/e-. The tolerance of each channel is $-/- 0.5\%$. The temperature drift is less than $+/- [0.1\%]$.

The nominal value of b is 0 volts. with an initial tolerance of $-$.- 1mV and a temperature drift of $+$.- [0.1mV].

The nominal value of vn is 7E-4 volts rms (8000e- rms) when connected to a grid with 80K between taps according to test data. In version 2.0. the noise component is calculated using a random number (drand48) between 0 and 1.0 times vn.

5. ADC Characterizations

As above. each ADC is characterized by three parameters. the ADC gain m(*digitalnumber/volt*). the ADC offset b(*digitalcounts*). The digital number output of the i-th ADC is given by:

$$DN_i = m_i V_i + b_i + f(dn_i) \tag{2}$$

The nominal value of m is 1638.4 digital counts/volt. The tolerance of each channel is +/- 0.5The temperature drift is less than +/- 0.1%. The nominal value of b is 0 volts. with an initial setting tolerance of +/- [1mV]. The temperature drift is less than +/- 0.1mV. The value of dn should be negligible for a properly aligned system.

6. CGCD output

The program output is directed to stdout in the following output.

```
0  5    618   817    84   1.011e+00
1  4    421   985   124   1.008e+00
2  5    123   982   422   1.009e+00
3  6    605   827    86   1.009e+00
4  4    513   911   103   1.006e+00
```

Where the first column is the event number. The second is the tap coarse position. Columns 3.4.5 are the digital output for the three taps centered about the coarse position. The last column is the total charge collected from all preamplifiers.

The Advanced X-Ray Astrophysics Facility High Resolution Camera

Stephen S. Murray and Jon H. Chappell

Smithsonian Astrophysical Observatory, 60 Garden Street Mail Stop 6, Cambridge MA 02138

Abstract

The HRC (High Resolution Camera) is a photon counting instrument to be flown on the Advanced X-Ray Astrophysics Facility (AXAF). It is a large field of view, high angular resolution, detector for the x-ray telescope. The HRC consists of a CsI coated microchannel plate (MCP) acting as a soft x-ray photocathode, followed by a second MCP for high electronic gain. The MCPs are readout by a crossed grid of resistively coupled wires to provide high spatial resolution along with timing and pulse height data. The instrument will be used in two modes, as a direct imaging detector with a limiting sensitivity of 10^{-15} ergs/cm^2 sec in a 10^5 second exposure, and as a readout for an objective transmission grating providing spectral resolution of several hundreds to thousands.

Introduction

The next major x-ray observatory planned by NASA is the Advanced X-Ray Astrophysics Facility (AXAF), for which there was a recent Announcement of Opportunity [1] for instruments. Among the four instruments selected for Phase B design definition study is the High Resolution Camera (HRC). This is a photon counting detector which provides high resolution images of celestial x-ray sources along with precise information on photon arrival times, and low resolution spectral data.

The AXAF is intended to be a long lived major observatory with a lifetime in excess of 15 years. It will be launched sometime in the 1990's and will carry a 10 meter focal length x-ray telescope consisting of six pairs of nested Wolter Type I mirrors. The telescope will have on axis angular resolution of about 0.5 arc-seconds, and will operate over the energy band from 0.1 to 10 keV. In addition to the HRC, the observatory will include a low energy transmission grating spectrometer (LETGS) that is read out using the HRC. There are two higher energy transmission gratings and three other focal plan instruments that were also selected for Phase B study. These are discussed in companion papers presented at this conference.

The overall scientific objectives of AXAF are [1]:

- .To determine the nature of celestial objects from normal stars to quasars.
- .To understand the nature of physical processes which take place in and between astronomical objects.
- .To understand the history and evolution of the Universe.

The HRC will be used to address these general areas of research. Some of the specific scientific investigations that can be carried out are studies of:

- .The nature and origin of the cosmic x-ray background and the relative contributions of quasars, primordial galaxies, and diffuse gas at cosmological epochs.
- .The nature and origin of nuclear activity in galaxies and quasars, and the physical relationships between AGNs and their host galaxies.
- .The structure and evolution of galaxy clusters and superclusters as probes of the formation of galaxies and theories of the early universe.
- .The mass and nature of haloes of galaxies as derived from observations of the hot gas they contain and from the x-ray properties of stars.
- .The origin of stellar activity as manifested in the x-ray emission from winds and coronae of stars.

These scientific studies require the high angular resolution made possible by the x-ray optics of AXAF and the imaging performance of the HRC. They also require the use of the grating spectrometer to obtain high spectral resolution data for various classes of x-ray sources.

Instrument Description

The HRC is a single photon counter, that is it detects individual x-rays and provides the position, energy, and time of arrival for each. The detector is based on the use of microchannel plates and an electronic readout. It is similar to the highly successful HEAO-2 (Einstein Observatory) High Resolution Imaging Detector (HRI) [2,3] which operated

flawlessly for 2½ years in-orbit. The main detector properties are summarized in table 1., they include high spatial resolution and high time resolution over the entire field of view, low internal background, low sensitivity to cosmic ray induced background, high x-ray quantum efficiency from 0.1 to 8 keV, and modest energy resolution particularly at low energies. Compared to the Einstein HRI, the AXAF HRC has substantially increased capability in the areas of quantum efficiency, detector size, reduced background rate, and intrinsic energy resolution. These properties of the HRC, combined with the large area of the AXAF x-ray optics lead to an increase in point source sensitivity of 50 compared with the Einstein HRI. The low background of the HRC also provides a sensitive detector for studies of diffuse sources. The high efficiency and high spatial resolution of the HRC at low x-ray energies allows it to be used as an efficient readout for the grating spectrometer, particularly below 0.5 keV.

The x-ray detector, shown schematically in figure 1, consists of a protective UV/Ion shield; a photocathode, which converts the incident photons to electrons; a set of microchannel plates (MCPs), which amplify the electron signal while maintaining high spatial and temporal resolution; and electronic read out, which uses resistively coupled crossed wire grids (CGCD); and an active plastic scintillator anticoincidence shield, which reduces the induced cosmic ray background. The entire instrument includes two detector assemblies which are housed in a vacuum chamber with calibration and checkout mechanisms such as a UV calibration system, radioactive x-ray sources, and fiducial lights. Electronics providing low voltage power, high voltage bias, event processing, command decoding, and telemetry are also part of the instrument.

The HRC has two principal operating modes, as a direct imaging device and as a readout for the objective grating. In the imaging mode, a single detector assembly is active and the center of the detector is nominally at the axis of the x-ray telescope. In the spectroscopy mode, there are several possible combinations of operating detectors and telescope axis positions. The nominal configuration will be with both detector assemblies active, and the telescope axis position offset to the interior corner of a detector. The detectors are oriented to provide maximal spectral coverage in both first order images from the grating. The low energy grating dispersion is such that in this configuration wavelengths shortward of ~140A will fall on the detectors. The two detector assemblies are slightly tilted with respect to one another (~30 arc-minutes). This approximates the Rowland circle of the grating and maximizes the energy resolution at the longest wavelengths. Focus adjustments are also provided since the optimal axial position differs in the imaging and spectroscopy modes.

The Instrument Principal Investigator (IPI) team for developing the HRC includes members of the Harvard-Smithsonian Center for Astrophysics, Leicester University, and the University of Hawaii. Overall direction of the project is through the Principal Investigator (PI) at the Smithsonian Astrophysical Observatory (SAO). In the Phase B design definition portion of the project, major responsibilities for detector study have been spread out among the participating organizations to take advantage of the expertise available. Specifically, photocathode and MCP studies are being jointly carried out at SAO and Leicester, UV/Ion shield design is being done at Hawaii, and the readout system and active anticoincidence are being developed at SAO.

Instrument Development

Each of the major detector elements contributes to the overall performance of the HRC. The window determines the low energy efficiency of the detector while providing shielding against ultraviolet radiation and low energy ions which would otherwise dominate the instrument background. The photocathode determines the quantum efficiency, uniformity of response, and energy resolution. We have selected CsI for the photocathode based on the work of Fraser et al. [4] who have demonstrated many of the desired properties of a soft x-ray photocathode. The microchannel plates determine the limiting spatial resolution due to their pore size. The operating voltages on the MCPs effect the gain uniformity of the detector, the internal background, and the spectral resolution. The crossed grid charge detector readout also determines the spatial resolution of the HRC, particularly important parameters are the wire and resistor uniformity, and the operating voltages.

Photocathodes

The use of CsI as a soft x-ray photocathode has been discussed by Fraser et al. [4], who have measured various properties of CsI deposited directly onto a microchannel plate. Their latest results are described elsewhere in these proceedings [5]. Chappell et al. have evaporated up to 26,000 A of CsI onto the front surface of an MCP [6] and have confirmed the efficiencies reported by Fraser. The strong dependence of coated MCP detector quantum efficiency on the angle of incidence [7] requires the deposition geometry to be optimized for the particular application. In the case of AXAF, the cone angle of the telescope beam ranges from 2° to 4°, and the plate must be coated at angles at least this shallow to insure adequate penetration of the CsI into the channels. The coating process must also be uniform and cylindrically symmetric to insure that there will not be

systematic variations in efficiency or gain. This requires carefully controlled conditions in the deposition process such as rotation of the MCP with respect to the CsI source and sufficient source to MCP distance to insure uniform illumination. In figure 2, the quantum efficiency versus energy is shown for the HRC. This curve is based on theoretical calculations by Fraser [8] and normalized by measured values at several energies. The effects due to absorption edges in Cs, I, and the MCP glass are included. [9] In addition to the high detection efficiency afforded by the use of CsI, Fraser et al. have shown that it is possible to operate CsI coated MCPs in a mode whereby energy resolution is obtained. Figure 3 shows an example of the pulse height distributions obtained at two different energies using a CsI coated MCP. Fraser and colleagues present more recent results on this aspect of coated channel plates in their contribution to these proceedings [5].

We have investigated alternatives to directly coating MCPs with x-ray photocathodes. Henke and Henry [10] suggested that free standing cathodes made by depositing low density ("fluffy") CsI on thin plastic films could yield high quantum efficiencies, particularly at energies above 6 keV. We constructed this type of photocathode by evaporating CsI onto stretched polypropylene in a chamber filled with nitrogen at low pressure. The resulting photocathode was placed in front of an MCP chevron and operated at various voltages with respect to the front channel plate. The quantum efficiencies measured were not significantly higher than those for the deposited photocathodes. Moreover, at low energies the window absorption resulted in lower net efficiency when compared with directly deposited cathodes.

We also examined the energy resolution performance of the fluffy photocathode and found that there was no measurable difference in pulse height distributions as function of x-ray energy. This is because the fluffy photocathode produces a secondary electron distribution that peaks at one electron independent of the incident energy [11]. Only the tail of the distribution changes with energy, and this effect is washed out by the MCP gain characteristic. In the case of deposited CsI photocathodes, the most probable number of secondary electrons depends on incident energy and thus provides energy resolution [9]. The secondary electron yield from CsI deposited onto the MCP increases with increasing x-ray energy. However, the depth of penetration of the x-ray photon also increases with energy so that the most probable number of electrons that escape into the MCP channel to begin the multiplication process does not grow linearly. Measured performance indicates that useful spectral resolution can be obtained only for x-ray energies below about 2 keV.

Microchannel Plates

The microchannel plates we have been using for the HRC are manufactured by Mullard Ltd in the United Kingdom. These are 100mm x 100mm square plates with 12½ µm pores on 15 µm centers. The plates have a length to diameter (l/d) ratio of 120/1, and were specially manufactured for this application. We have also been using somewhat more standard 36mm diameter MCPs from Mullard for our deposition and quantum efficiency measurements. Tests with the large area plates have been limited to imaging studies and background measurements. When we are able to obtain additional large area plates, we will carry out coating tests and lifetime studies to confirm the results from the smaller plates. Since the MCPs are made from the same glass and go through similar processing as the standard Mullard MCPs, we do not anticipate any significant performance changes. We note however, that the background rate in the one set of large area plates we have tested is substantially lower than that of any set of MCPs we have previously measured. This low internal background significantly improves the overall detector performance in terms of signal to noise and sensitivity to low surface brightness objects. We are currently investigating the reasons for such low count rates in a joint program with our colleagues at Leicester University.

The imaging performance of the HRC is demonstrated in figure 4. Here we show an x-ray shadowgraph obtained with the large area MCPs that were illuminated through a mask made from 5 µm thick nickel. The readout used is a 75mm x 75mm CGCD connected to a HEAO-2 event processor. As shown in the figure, the detector can easily resolve the smallest slit pattern on the mask corresponding to 20 lp/mm. An analysis of the image, assuming a gaussian point response function for the detector, results in a measured spatial resolution characterized by FWHM = 25 µm (= 10.6 µm). The resolution obtained is limited mainly by MCP pore size with a small contribution due to electronic noise.

We have recently had discussions with Mullard regarding the availability of large area MCPs with smaller pore size. There appear to be no technical problems with manufacturing them in the HRC format, however at this time there has been no official quotation form Mullard for prices or delivery schedule. The potential advantages of such plates are discussed by Fraser et al. [5] in terms of improved spectral resolution and lower background. Based on the imaging results discussed above, we predict that MCPs with 8 µm pores would yield spatial resolution characterized by a FWHM of 20µm. Fraser et al. [5] have shown that the smaller pore size MCPs can be sucessfully coated with CsI and that they yield improved pulse height distributions.

Read Out System

The crossed grid charge detector (CGCD) used for the Einstein HRI has been described in the literature (3,12). We have constructed two larger readouts which provide 75mm x 75mm active area for imaging studies. The imaging data discussed above was obtained with one of these CGCDs. The data show that the coarse/fine position determination algorithm can be scaled from the 25mm unit with no loss in resolution.

The Einstein HRI readout system used 17 preamplifiers per axis to divide the image plane into 16 x 16 coarse position elements. In the case of the HRC we will have 65 preamplifiers per axis and 64 x 64 coarse image elements. The fine position is determined from a centroid calculation of the charge collected on the grid wires. The precise algorithm to be used for the HRC is one of the areas of investigation during Phase B. For Einstein a 'three tap' calculation was carried out using an analog divide circuit and a multiplying ADC [12]. For the HRC were are considering the use of a digital processor and a 'four tap' algorithm. The advantages of this approach are faster event processing time and less systematic distortion in the calculated position. To allow a more complete evaluation of this design, we have built a set of prototype processing electronics which are interfaced to a MASSCOMP MCS-500 computer system. The electronics provide the coarse position encoding and digitization of signals from the CGCD. The computer is used to carry out the fine position calculation which can be modified via software so that a number of algorithms can be studied. The MASSCOMP also serves as the ground support system for the HRC providing command, status, and imaging display capabilities.

Background

The sensitivity of MCPs to high energy charged particles and gamma rays is a major contributor the the total background in detectors such as the HRC. In order to minimize this background source we have designed the instrument with a plastic scintillator shield. Laboratory measurements show that between 50% and 85% of cosmic ray muons produce events in the HRC. Because the HRC is a photon counting detector, it is possible to reject cosmic ray induced events using an anticoincidence system. The resolving time of the HRC is fast (10usec), and the total count rate from cosmic rays is low (< 100 ct sec^{-1}). The HRC will process all events and include the status of the shield so that the induced events can be screened out during ground processing. Measurements of the pulse height distribution from shields similar to the one planned for the HRC show that more than 99% of all minimum ionizing particles can be detected [13] and thus this component of background effectively reduced.

The background due to gamma rays and compton scattered electrons is not reduced by the anticoincidence system. However, the HRC is relatively insensitive to gamma rays as demonstrated by the observation that the background rate for the Einstein HRC did not increase significantly in orbit over the ground rate. We have measured the response of a chevron MCP detector to gamma rays from 60 keV to 400 keV using radioactive sources. For gamma rays that pass through the plates in the plane normal to the channel axis (the maximum amount of material), there is about a 3% chance of an interaction which is independent of the gamma ray energy in the region studied. Most of these interactions are single compton scattered electrons that are knocked out from the channel walls. These electrons produce low amplitude events in the MCP first because they are single electrons initially, and second because most events occur part way down the channels resulting in less gain. By setting the valid event threshold high enough most of these events are not processed.

Instrument Performance

The predicted performance of the HRC depends upon the performance of the individual elements of the instrument as described above, and the manner in which the AXAF spacecraft and x-ray telescope perform. The baseline AXAF mirror areas are given in the Announcement of Opportunity. Based on the recent measurements from the Test Mirror Assembly (TMA) [14], the expected mirror scattering function and figure have been revised (favorably). We have taken a surface roughness of 10A and a FWHM of <0.5 arc-seconds to characterize the mirror. Image quality also depends on the precision of the aspect solution obtained. We have assumed that the total on axis point response function will have FWHM <1.0 arc-seconds. In calculating the HRC sensitivity, we included the effects of a 3000A thick Lexan UV/Ion shield overcoated with 500A of aluminum. The CsI quantum efficiency shown in figure 2 was assumed.

The detector background is derived from three components, the internal MCP noise, cosmic and gamma ray induced events, and diffuse x-rays. The contributions of these components are listed in table 2. The internal MCP background rate is that measured in the laboratory for HRC type plates as discussed above. The cosmic ray rate assumes a 99% rejection efficiency using an anticoincidence shield. The diffuse x-ray background is based on a model consisting of three parts: a thermal galactic component with temperature 10^{6} °K, emission measure 1.5 x 10^{-3} cm^{-6}pc, Hydrogen column 1 x 10^{-4} cm^{-2}; a second thermal galactic component with temperature $10^{6.5}$ °K, emission measure 3.6 x 10^{-3} cm^{-6}pc, Hydrogen column 1 x 10^{-2} cm^{-2}; and a power law extragalactic component of the form

$10E-1.4$ photons $cm^{-2}s^{-1}keV^{-1}ster^{-1}$ with a hydrogen of column density 3×10^{20} cm^{-2}. The emission measures and Hydrogen column densities used are typical for high galactic latitudes.

Based on these inputs and assumptions, we have calculated the HRC sensitivity for on axis point sources and diffuse sources of 20 arc-second extent. Figure 6 is a plot of a typical sensitivity calculation showing the minimum detectable source flux as a function of observation time. In this figure, the criteria for detectability is that the source flux be measured with a 5 statistical precision (20% measurement error). The source spectrum was taken to be a power law with photon index 1.4 and with a hydrogen column of 3×10^{20} cm^{-2}.

Acknowledgements

References

1. NASA Announcement of Opportunity AO No. OSSA-3-83 Advanced X-Ray Astrophysics Facility, August 15, 1983

2. Giacconni et al., Ap.J. (Letters) Vol. 230 (1979) pp. 540

3. Henry,J.P.,Kellogg,E.M.,Briel,U.G.,Murray,S.S.,VanSpeybroeck,L.P., and Bjorkholm,P.J., Proc. SPIE Vol. 106 (1977) pp. 163

4. Fraser,G.W. and Pearson,J.F., Nucl. Instr. Meth. Vol. 219, (1984) pp. 199

5. Fraser,G.W., Whiteley,M.J., and Pearson,J.F., "Developments in Microchannel Plate Detectors for Imaging X-ray Astronomy", these proceedings.

6. Chappell,J.H., Everman,D.E., and Murray,S.S., in preparation

7. Bjorkholm,P.J., VanSpeybroeck,L.P.,and Hecht,M. Proc. SPIE Vol. 106 (1977) pp. 189

8. Fraser,G.W. Private Communication (1985)

9. Fraser,G.W.,Barstow,M.A.,Pearson,J.F.,Whiteley,M.J.,and Lewis,M., Nucl. Instr. Meth. Vol. 224, (1984) pp. 272

10. Henke,B.L. and Henery,J.P., Private Communication (1983)

11. Garwin,E.L.,and Llacer,J., J. Appl. Phys. Vol. 41 (1970) pp. 1489

12. Kellogg,E.M.,Henry,J.P.,Murray,S.S.,VanSpeybroeck,L.P.,and Bjorkholm,P.J., Rev. Sci. Instr. Vol. 47, (1976) pp. 282

13. Grindlay,J.E.,Garcia,M.A.,Burg,R.I.,and Murray,S.S., IEEE Trans. Nucl. Sci (1986) to be published

14. Schwartz,D.A., et al. "X-Ray Testing of the AXAF Technology Mirror Assembly (TMA) Mirror" these proceedings

Figure Captions

Figure 1. Schematic Diagram of the AXAF HRC showing the major functional elements.

Figure 2. Quantum detection efficiency of the HRC versus x-ray energy.

Figure 3. Sample pulse height distributions from a CsI coated MCP at two incident energies (taken from Fraser et al [9]).

Figure 4. An example of HRC imaging performance. X-ray image through a shadow mask place directly in front of the detector and illuminated with low energy x-rays from a continuum source.

Figure 5. The sensitivity of the HRC as a function of exposure time for point-like and extended sources.

Figure 1

QUANTUM DETECTION EFFICIENCY

AXAF HRC

EINSTEIN HRI

EFFICIENCY (%)

ENERGY (keV)

Figure 2

Figure 3

= ꞮꞮꞮ= ‖

=ꞮꞮꞮ

HEAO-B

ꞮꞮꞮ= 12.5 µm open
      37.5 µm closed
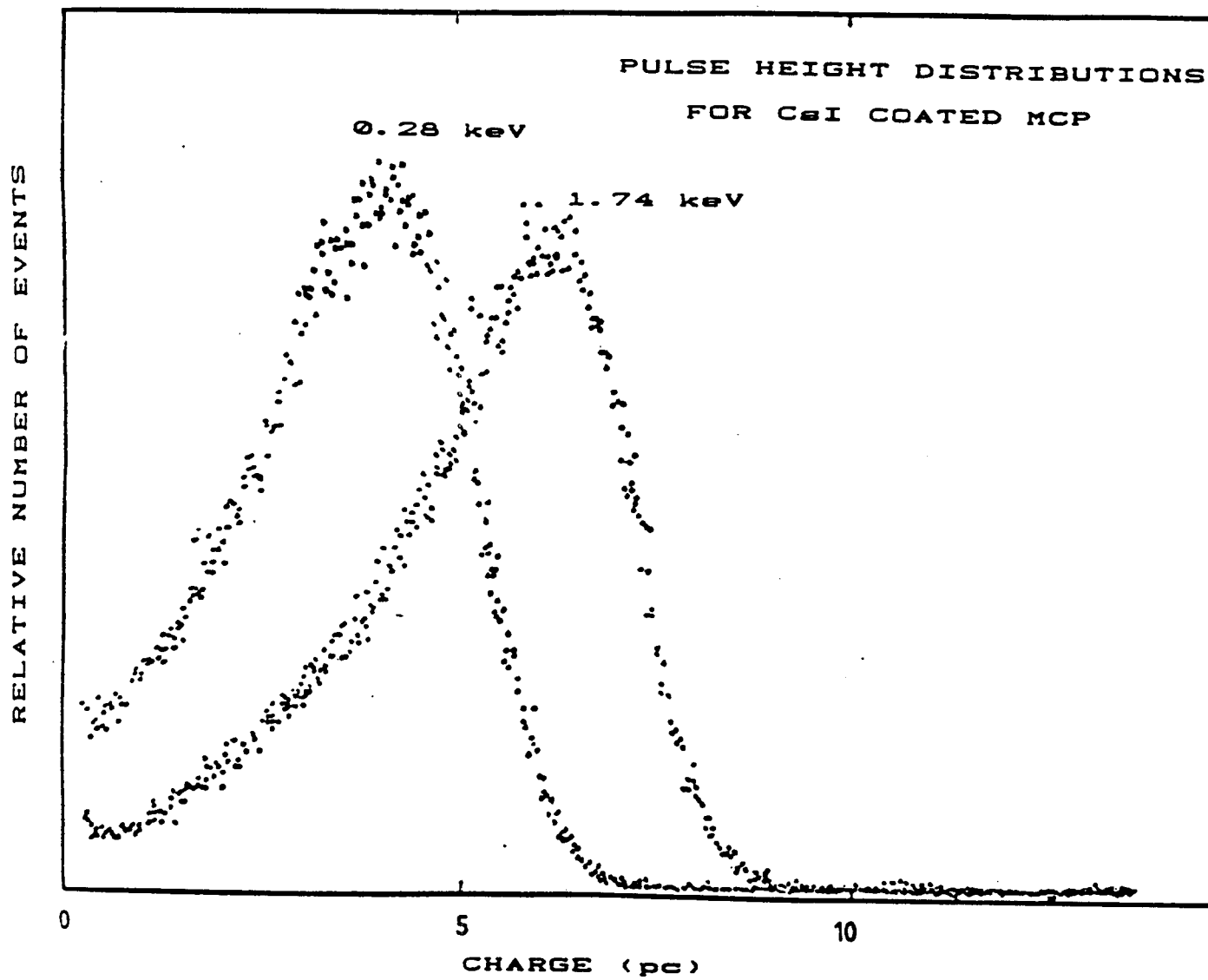
25 µm open
75 µm closed =ꞮꞮꞮ

FWHM = 25 µm

(σ = 10.5 µm)
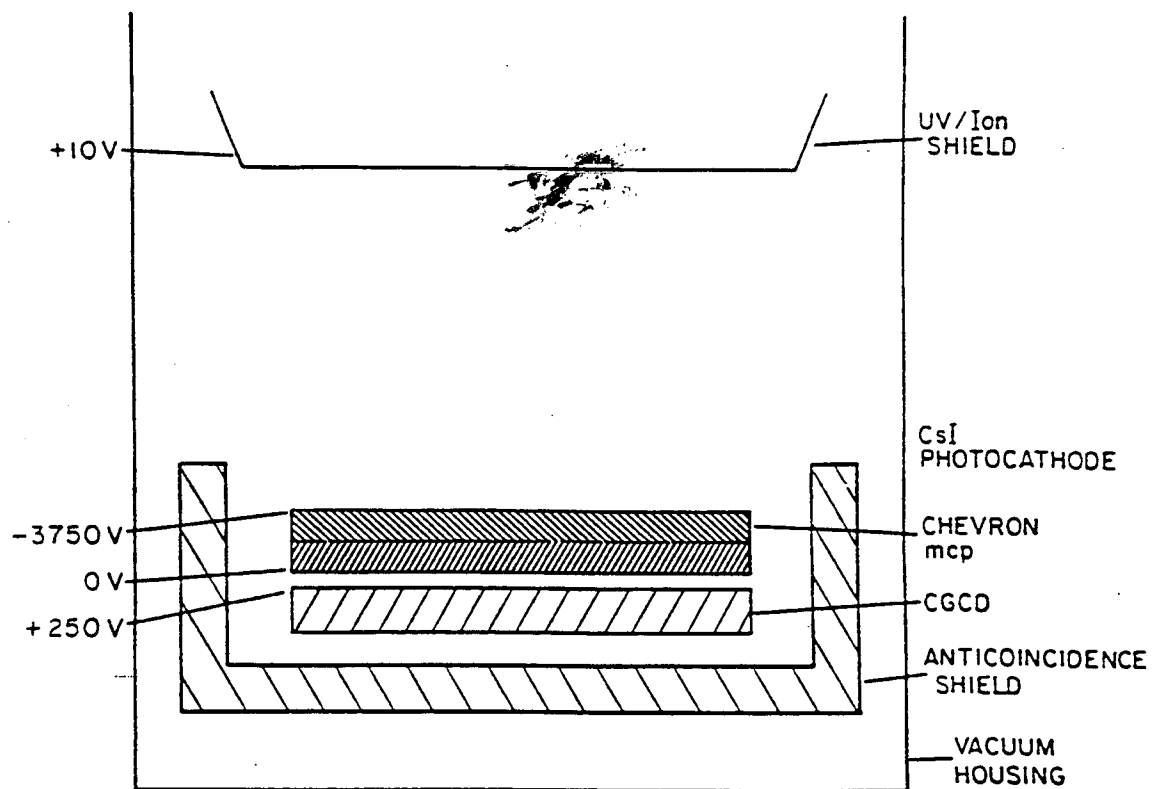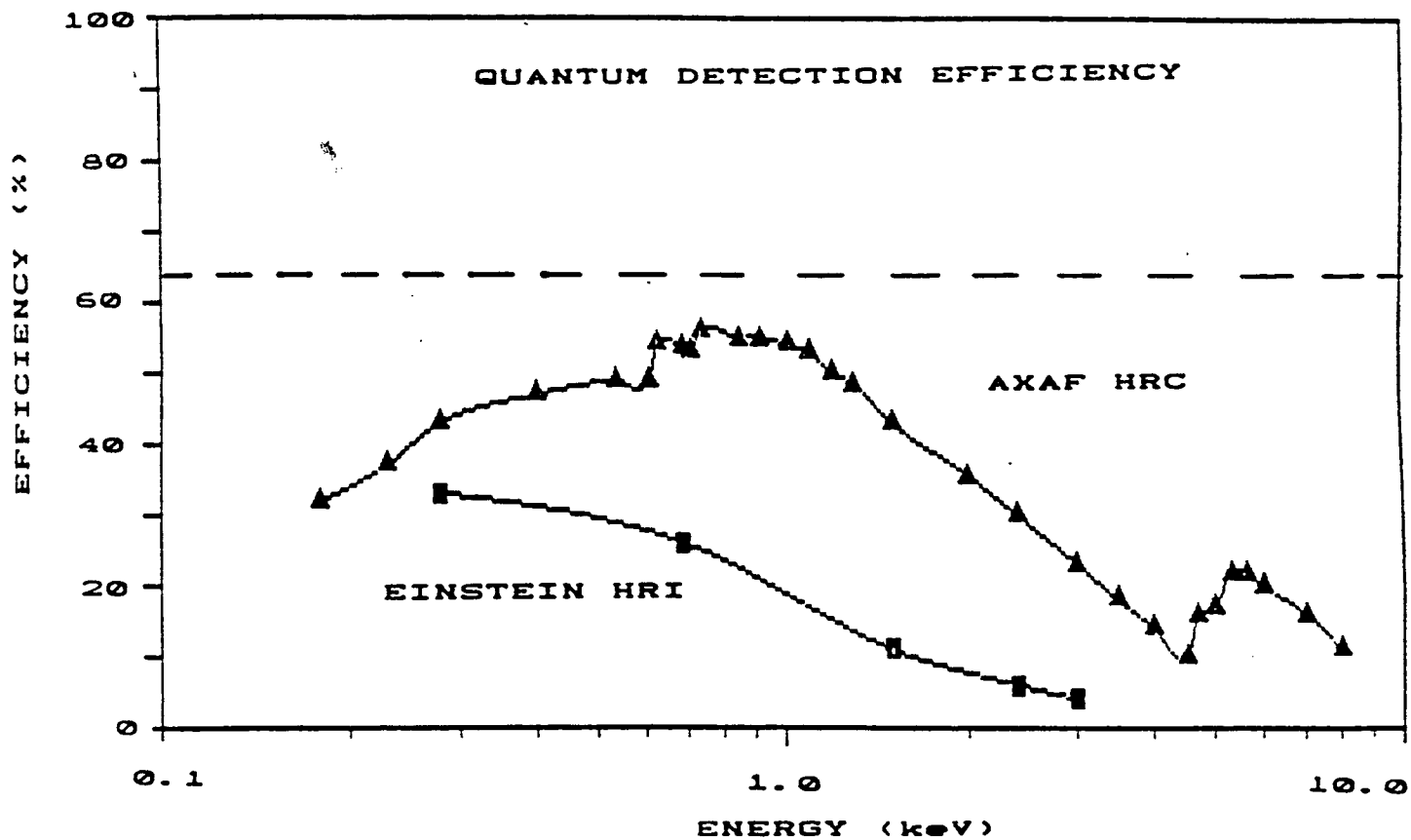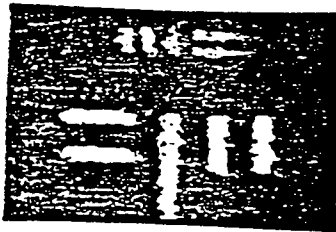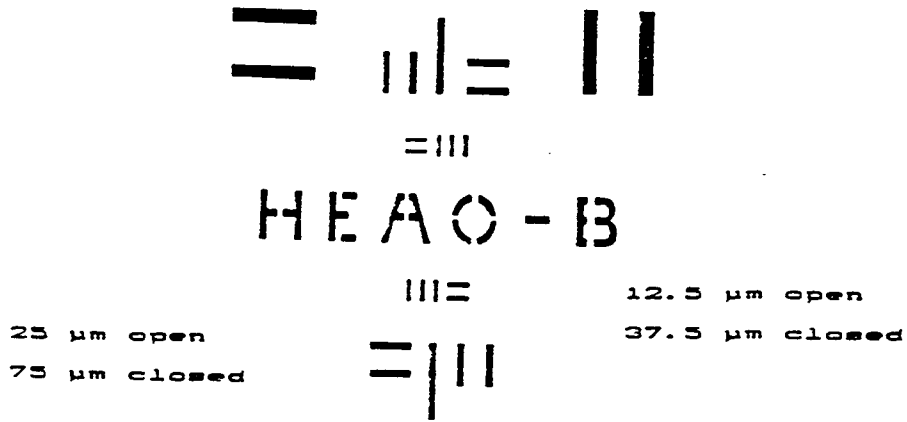
Figure 4

SENSITIVITY 5 SIGMA FLUX MEASUREMENT

Power Law 1.4 NH 3E20

Einstein Deep Survey △

Extended Source

Point Source ▣

3 Sigma Detection ◇

Log Minimum Flux (erg/sq.cm./sec)

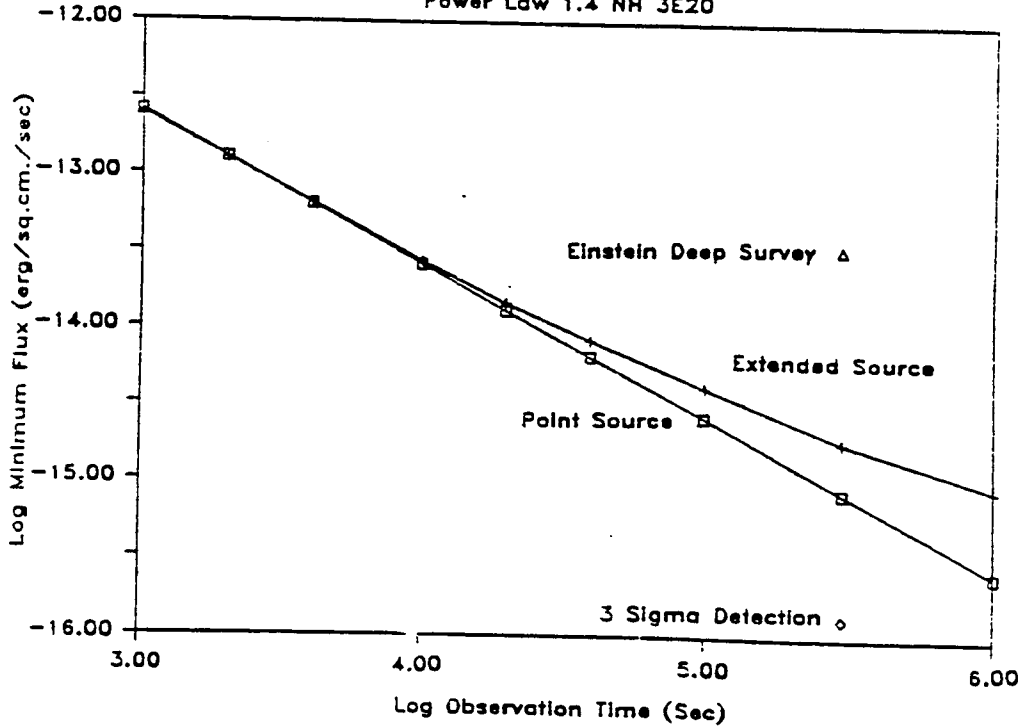Log Observation Time (Sec)

Figure 5

The AXAF High Resolution Camera

Stephen S. Murray
Jon H. Chappell
Smithsonian Astrophysical Observatory

9 July 1988

1 Introduction

The High Resolution Camera (HRC) [12] is one of four instruments selected for detailed design definition as a focal plane detector for an upcoming NASA mission - the Advanced X-Ray Astrophysics Facility (AXAF) [2]. which is scheduled for launch at the end of calendar year 1996. The camera is a microchannel plate (MCP) based detector utilizing a CsI photocathode to enhance X-ray quantum efficiency in the 0.1 to 10.0 keV energy band. An electronic readout provides better than $25\mu m$ FWHM spatial resolution over a 100mm x 100mm active area.

The HRC is closely related to the High Resolution Imaging Detector (HRI) which was successfully flown on the Einstein (HEAO-2) Observatory [3] from 1978 to 1981. A similar detector has been built for the ROSAT Observatory [4] which is scheduled to be launched in February of 1990. The major differences between the HRC and its predecessors are in overall size (20 times greater active area), quantum efficiency (3 to 4 times higher), count rate limitation (2 to 5 times greater count rate), background (3 to 5 times lower), and energy resolution below 2 keV (some compared to none).

While the basic x-ray detector is similar to previous instruments. the electronic readout and processing chain of the HRC incorporate major im-

provements in technology that allow digital event handling. This results in an extremely flexible system which is also fast enough to process up to 10,000 events per second as compared to under 1000 events per second in the analog based systems. The periodic nature of our coarse/fine electronic position encoding can result in periodic spatial distortions in the image plane [5]. We have made models of the position algorithm that reproduce this behavior and illuminate the most important sources of this feature. Based on these models we can minimize the distortions in the raw detector output and more importantly we can make systematic corrections to the data to a high degree of precision. We have also studied the relative contributions of electronic noise in the readout preamplifiers compared with the systematic sources of readout noise such as the finite size of the microchannel plate pores.

2   Detector Description

The major elements of the HRC are depicted schematically in figure 1. The active sensor is a CsI coated MCP followed by an uncoated MCP in the "chevron" configuration which provides high electron gain without ion feedback [6]. A thin plastic window, coated with aluminum on both sides serves as an ion shield and a UV filter. This eliminates background from geocoronal emission, especially at 305Å. The filter also reduces the detector sensitivity to hot stars which emit strongly in the UV continuum around 1600Å. The HRC baseline filter is 6000Å of Parylene-N, coated with 300Å of aluminum on the front and back sides.

The readout consists of orthogonal planes of wires which are connected to each other via a chain of discrete thin film resistors. Periodically there is a connection to a low input impedance charge sensitive preamplifier so that the charge cloud emerging from the MCP chevron is collected and divided according to Ohm's law [7]. The MCPs and readout are contained in a vacuum enclosure to allow ground operation and to provide protection for the components. A plastic scintillator behind the detector functions as an anticoincidence shield for cosmic ray induced background.
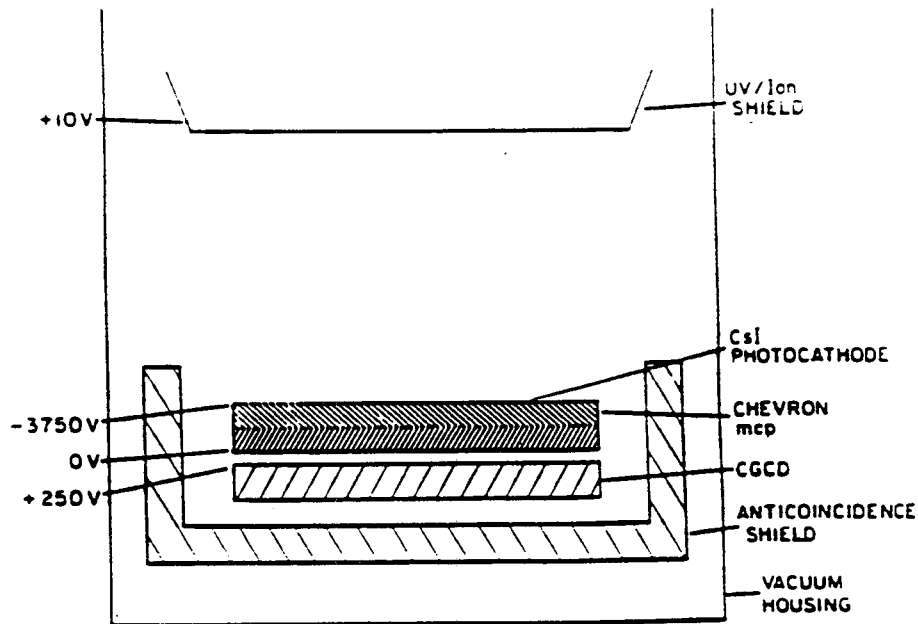
Figure 1: Schematic Diagram of HRC

The MCPs are 100mm x 100mm square, and other elements of the detector are sized accordingly. These large area plates are manufactured specifically for the HRC by Mullard Ltd. in the United Kingdom. The MCPs have 12.5μm diameter pores on 15μm centers, and they are 1500μm thick corresponding to a length-to-diameter ratio of l:d = 120:1. These plates each have a 6° to 8° bias and are rotated with respect to one another in the plate holder to give the standard chevron configuration. The is a small gap between the plates of about 400μm, which is electrically biased with a slight retarding voltage of 50 to 100 volts. The front MCP has about 1300 volts bias, and the rear plate is biased at about 1500 volts. This gives a most probable gain of about 10^7 electrons per incident x-ray, and a pulse height distribution characterized by a FWHM of 100%. These are typical values for Mullard MCPs of similar properties and operated at similar voltages [8]. The rear surface of the rear MCP is held at ground potential.

The crossed grid charge detector (CGCD) readout uses 100μm diameter gold plated tungsten alloy wire on 200μm centers to form the two collecting grids. These are formed on a ceramic frame which sets the two planes about 400μm apart. The grids are suspended about 1000μm in front of a solid conducting plane - the reflector, which is electrically biased about 50 volts

negative with respect to the grids. The grids are biased about 250 volts positive with a small potential (about 1 volt) difference to assure an even charge split. The thin film resistors are manufactured on ceramic strips with the same pitch as the wires (1 resistor per $200\mu m$). These are bonded to the grid frame and each resistor is electrically attached to the grid wires using short lengths of $25\mu m$ gold wire and an ultra-sonic wire bonder. The preamplifiers are connected to every 8th grid wire. The 100mm x 100mm HRC readout has 1025 wires. 1024 resistors, and 128 preamplifiers.

The vacuum enclosure is a stainless steel housing with a motor driven door. The door is sealed with an "o"-ring and is positively latched. Ceramic multiwire feedthroughs are used to bring the 256 preamplifier connections out from the vacuum chamber. The chamber is continually pumped while on the ground using a small ion pump. Pressure is maintained below 1 x 10^{-5} torr. The pump is turned off a short time before launch and is not used during flight. The MCPs and CGCD may outgas. building up the pressure inside the vacuum chamber to levels that could damage the thin plastic UV/ion shield when the chamber door is opened. To prevent this. a solenoid activated vent valve is used to equalize the vacuum in the chamber with the spacecraft environment prior to door opening. With this arrangement. it is possible to operate the HRC on the ground to verify proper performance. and to keep the vacuum door closed in orbit until the spacecraft has outgassed to acceptable levels.

The anticoincidence shield is a single piece of plastic scintillator viewed by redundant photomultiplier tubes (PMTs). We use 1/2 inch thick standard scintillator material, and low background PMTs. The scintillator. phototubes, coupling techniques, and preamplifiers are the same as those used in a balloon experiment (EXITE) recently constructed at SAO and flown from Australia to observe SN1987a [9]. About 99% of charged particle cosmic ray induced events can be eliminated using this shield.

3 Readout System

3.1 Charge Division

The readout system we use is an extension of the Crossed Grid Charge Detector [7] developed for the Einstein and ROSAT HRI's. One of the characteristics of these detectors is the presence of "gaps" in the transformation from real detector coordinates to electrical coordinates during event processing, and then back to real coordinates during ground processing. This is due to the discrete number of preamplifier readouts ("taps") used in the CGCD. The basic charge division process is illustrated in figure 2. One of the two grids is shown in cross section. The wires are evenly spaced with equal open and closed areas. They are connected by resistors ($R_w = 10K$ Ohms). A low input impedance charge sensitive preamplifier taps off the charge at every 8th wire so that the tap-to-tap resistance is $R_t = 8 * R_w$.
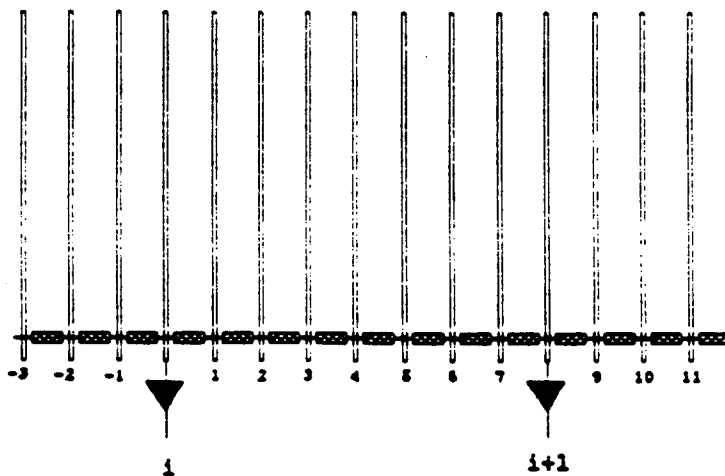

Figure 2: Schematic Diagram of CGCD in One Dimension

A charge q that is deposited on the jth wire past a tap i will be resistively divided so that the charge collected at the taps i and $i + 1$ will be given by

applying Ohm's law:

$$\left.\begin{array}{ccc} Q_i & = & q(8-j)/8 \\ Q_{i+1} & = & qj/8 \end{array}\right\} 0 \leq j \leq 8$$

Where Q_i and Q_{i+1} are the charges collected at taps i and $i+1$ respectively.

The event position can be calculated from the collected charge according to:

$$fp = \frac{Q_{i+1}}{Q_{i+1} + Q_i}$$

Where fp is the position (in units of preamplifier tap spacings) past the first tap which collects charge.

The total event position is then given by the first tap number (the coarse position) plus the above fine position.

3.2 Charge Spillover

If the charge cloud emitted from the MCPs was collected on only one wire of the grid, the event position would always be digitized to the wire pitch. A high resolution readout would require finely spaced wires. many individual resistors, and a correspondingly large number of preamplifiers. In the HRC. we allow the electron cloud to spread while traveling from the rear of the MCP stack to the CGCD so that many wires collect charge. The same position calculation will work since the algorithm appropriately weights the charge collected on each wire. In this case, the fine position will vary continuously as the center of the electron cloud moves within the taps. This two-tap algorithm is the simplest form of the coarse/fine position calculation. However. for events near a tap when the electron cloud extends over more than one wire, some of the charge collected may not be used in the position calculation. This "charge spillover" effect is shown in figure 3. and results in distorted positions being calculated. A specific example demonstrates this effect.
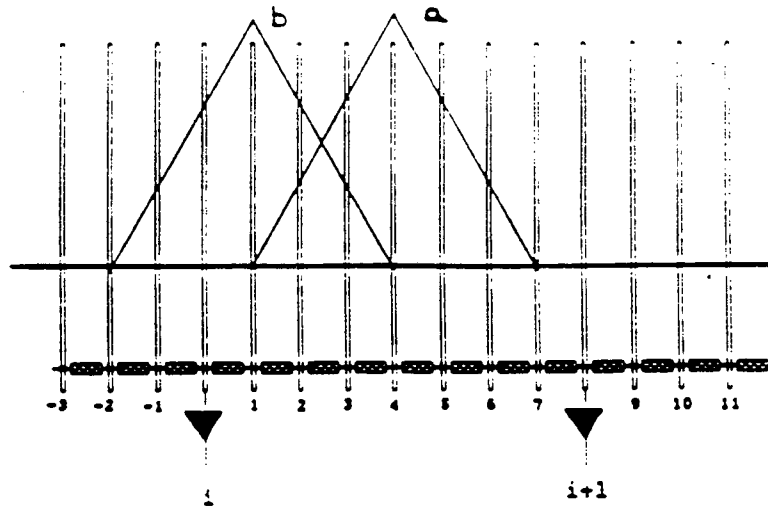
Figure 3: Charge Spillover Effect

3.2.1 Specific Example

Consider an electron cloud with a one-dimensional charge density distribution given by a triangle function (chosen only for illustrative purposes, with half width of 3 wires), and take two locations for the center of the event - case (a) where the charge falls entirely within two taps (centered on wire 4 in the figure); and case (b) where the event is near a tap (centered on wire 1 in the figure). Tables 1 and 2 show how the charge is collected and divided by the grid and what the total charge collected on the preamplifier taps will be, all normalized to the total charge in the event. The wire and tap numbering scheme corresponds to that used in figure 3.

Using the values given in the tables we can calculate the event positions using the two-tap coarse/fine algorithm and compare them to the true positions. In the first example, where all the charge is collected on the nearest two taps the calculated and true positions agree. In the second example the calculation gives $fp = 0.146$ of a tap spacing, and the true position is 0.125. The difference is due to the small amount of charge that gets collected on the $(i-1)^{th}$ tap. Notice that the percent error in position is 2.1% of a tap spacing or 16.8% in a differential sense, but that only 1.5% of the charge was not used. Figure 4 shows the calculated versus true position

Table 1: Collected Charge for Event on Wire 4

Wire #	Charge on Wire	Fraction Collected at Tap		
		i-1	i	i+1
-3	0	0	0	0
-2	0	0	0	0
-1	0	0	0	0
0	0	0	0	0
1	1	0	7/8	1/8
2	24	0	6/8	2/8
3	48	0	5/8	3/8
4	69	0	4/8	4/8
5	48	0	3/8	5/8
6	24	0	2/8	6/8
7	1	0	1/8	7/8
8	0	0	0	0
9	0	0	0	0
totals	215	0.000	107.500	107.500

for this example and illustrates that a "gap" in calculated positions occurs for events at the taps. In this example the gap size is 10% of a tap spacing.

3.3   Multi-Tap Fine Position Algorithms

One way to avoid the charge spillover effect is to make the electron cloud narrow. As already pointed out, this leads to a readout that is digitized at the grid wire spacing. The other alternative is to use coarse/fine position algorithms that make use of more than two taps. In the above examples a three-tap algorithm of the form

$$fp = \frac{Q_{i+1} - Q_{i-1}}{Q_{i+1} + Q_i + Q_{i-1}}$$

Table 2: Collected Charge for Event on Wire 1

Wire #	Charge on Wire	Fraction Collected at Tap		
		i-1	i	i+1
-3	0	0	0	0
-2	1	2/8	6/8	0
-1	24	1/8	7/8	0
0	48	0	8/8	0
1	69	0	7/8	1/8
2	48	0	6/8	2/8
3	24	0	5/8	3/8
4	1	0	4/8	4/8
5	0	0	0	0
6	0	0	0	0
7	0	0	0	0
8	0	0	0	0
9	0	0	0	0
totals	215	3.250	181.625	31.125

would completely eliminate the gaps. Detailed calculations of the charge spillover effect have ben made by Chappell and Murray [10] for a variety of charge distributions (functional forms and characteristic widths) in order to determine the relationship between the gap size and map distortion to the amount of charge that is not included in the calculation. The results are similar to the simple case discussed above.

This approach can be extended to algorithms that use as many taps as desired in order to insure that there is complete charge collection within the signals used for event position calculation. Two problems arise. First the electron cloud distribution from the MCPs appears to have a core/halo type of structure and the halo extent is large on the scale of taps on the CGCD. Second, and more important, is the extra uncertainty introduced in the position calculation due to the electronic noise associated with the
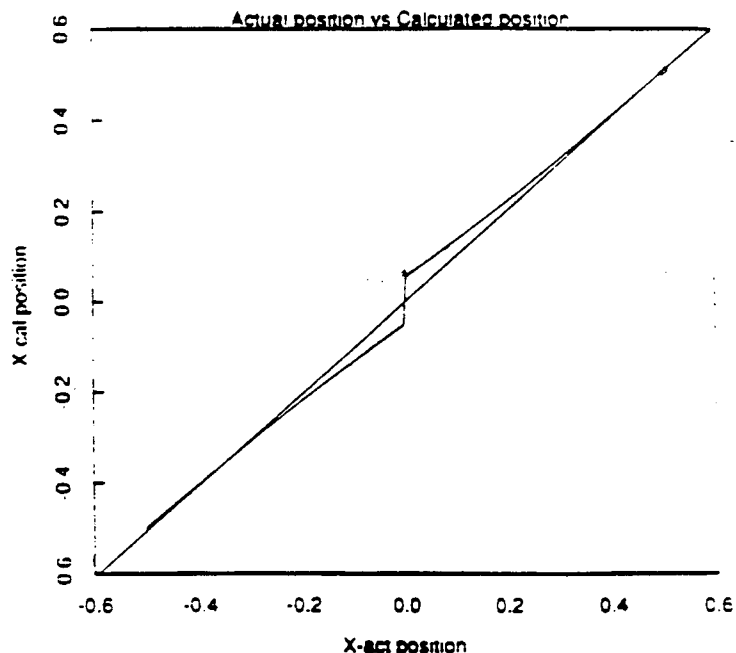
Figure 4: Gap due to "charge spillover" effect.

amplifiers.

3.3.1 Electronic Noise

Following the analysis done by Knapp [11], we have computed the positional uncertainty due to electronic noise as a function of fine position algorithm for the cases of systems that use from two to six signals. The detailed form for the linear combination of signal terms used in the fine position algorithms is derived from the requirement that the calculation be linear when all charge is collected, and it produce a single valued one-to-one mapping of real to electrical space. In effect a "center of mass" type of calculation is made. This is discussed in more detail by Murray and Chappell [12], and Chappell and Murray [10]. The electrical noise uncertainty is shown as a bar chart in figure 5. The noise uncertainties are relative to the two-tap case which results in the smallest electronic noise contribution. As pointed out by Murray and Chappell [12], the noise contribution increases much more rapidly than just the square root of the number of amplifier signals. This is due to the high weighting of additional amplifiers in the position algorithms.
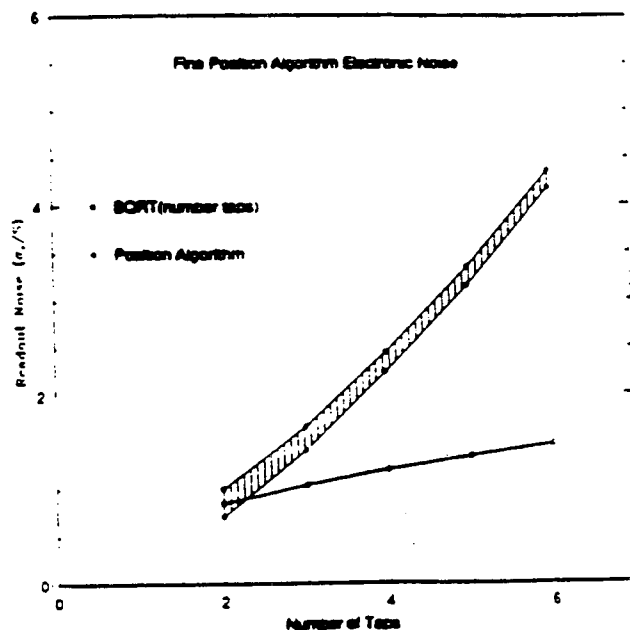
Figure 5: Electrical Noise Contribution vs Number of Taps .

Table 3: Fine Position Uncertainty (Electronic Noise)

# Taps	Minimum	Maximum	Mean=K_{taps}
2	$1/\sqrt{2}$	1	0.854
3	$\sqrt{2}$	$\sqrt{11}/2$	1.536
4	$\sqrt{5}$	$\sqrt{6}$	2.343
5	$\sqrt{10}$	$\sqrt{45}/2$	3.258
6	$\sqrt{70}/2$	$\sqrt{19}$	4.271

4 Measurements

The HRC prototype detector was designed to allow experimental investigation of the high resolution spatial properties of the instrument. The electronic processor identifies the coarse event position using high speed comparators and then captures the signals from the eight taps centered on this position for further analysis in a real time computer system. These data are also saved in unprocessed form as a data file so that different fine position calculations can be made for comparison. Figure 6 shows images of our standard high resolution test mask taken with the HRC prototype

using three. four. five. and six tap algorithms. These are images made from the identical raw data set. The three parallel slits outlined by a rectangle in these images have been projected on to the x-axis to provide an estimate of the image scale factor (microns/pixel) and equivalent one dimensional gaussian spatial resolution. These projections are plotted in figure 7.
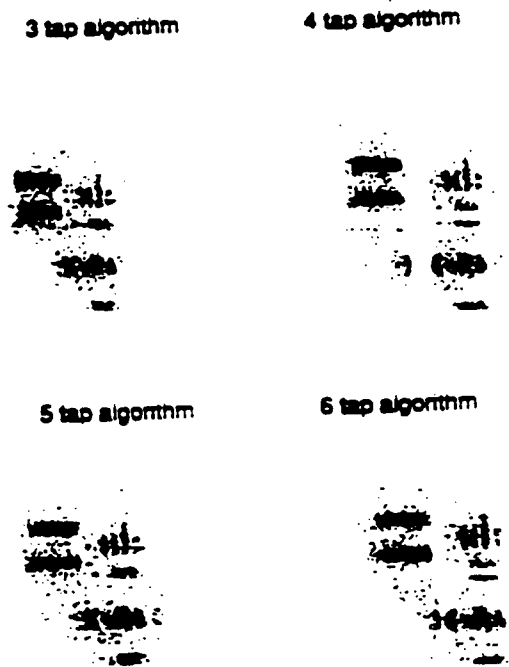
3 tap algorithm **4 tap algorithm**

5 tap algorithm **6 tap algorithm**

Figure 6: Images of resolution mask with: a) 3-tap. b) 4-tap. c) 5-tap. and d) 6-tap fine position algorithm.

We assume that the detector spatial point spread function (PSF) is approximately Gaussian characterized by standard deviation σ, and calculate the convolution of the PSF and slit of width W to model the projected data. The resulting integral can be expressed as:

$$I(x) = \frac{1}{2}\left\{ \text{erf}\left(\frac{W/2 - x}{\sqrt{2}\sigma}\right) + \text{erf}\left(\frac{W/2 + x}{\sqrt{2}\sigma}\right)\right\}$$

where erf is the error function. Using this convolution integral, we calculate the relationship between the ratio of the measured quantity, the full width
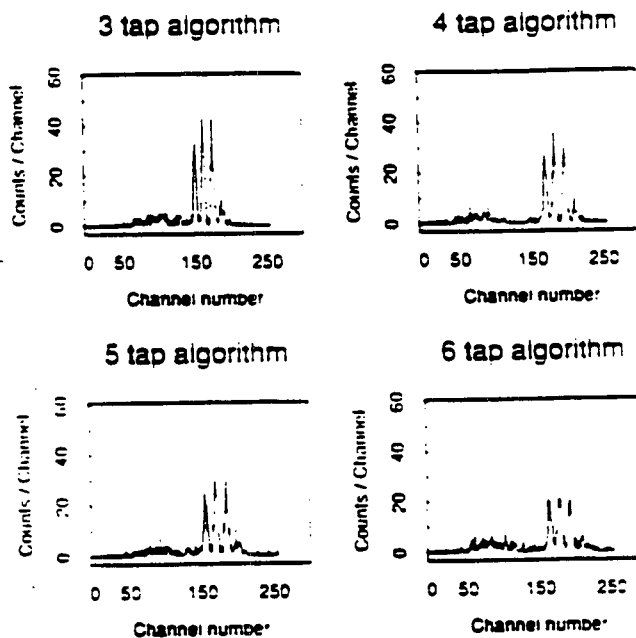
Figure 7: Projections of Slits on X-Axis.

at half maximum of the projected data. to the slit width (Γ_{slit}/W) and the ratio of the full width at half maximum to the Gaussian width (Γ_{slit}/σ). This is plotted in figure 8.

We measure Γ_{slit} for each of the three projected slit images and take the average value. The pixel scale is determined from the center-to-center spacing of the slits and the measured separation of the projections. Using the relationship in figure 8 we find the Γ_{slit}/σ and finally σ which is the Gaussian resolution of the detector. The FWHM resolution of the detector is a measure of the size of independent image elements and is given by $\Gamma_{det} = 2.354\sigma$.

We have carried out the above procedure for the four images of figure 6. and the results are listed in table 4. Using these data we can test the noise model discussed above by assuming that the image quality is due to two components – the effects of electronic noise (as discussed above) and
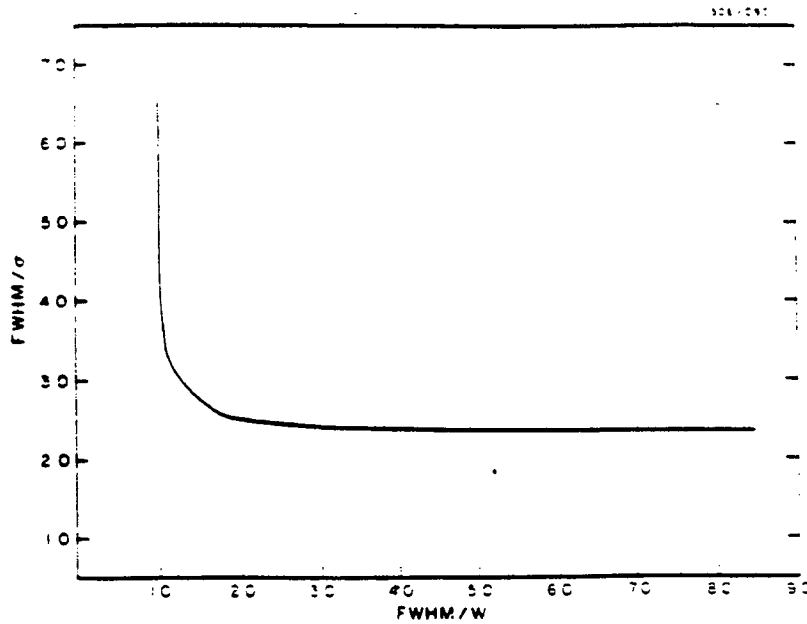
Figure 8: Convolution of Gaussian PSF and slit of width W.

systematic noise such as that due to the finite size of the MCP channels. That is we assume:

$$\Gamma^2_{det} = \Gamma^2_{elec} + \Gamma^2_{sys}$$

and.

$$\Gamma_{elec} = K_{taps}\Gamma_{e2}$$

where K_{taps} is the noise coefficient from table 3 relative to the maximum two-tap electronic noise Γ_{e2}.

Table 4: Image Resolution

Number of Taps	Observed FWHM	Calculated FWHM	Difference
2		24.55	
3	28.0	28.28	0.27
4	33.9	34.32	0.42
5	43.3	42.39	-0.92
6	51.8	52.14	0.34

A least squares fit for the quantities Γ_{sys} and Γ_{e2} yields the results

given in table 4 with $\Gamma_{sys} = 22.7\mu m$, and $\Gamma_{e2} = 11.0\mu m$. As shown in the table the least squares fit matches the data points quite well. In addition the systematic component is about the value expected on the basis of the MCP pore size of $12.5\mu m$. Finally the electronic noise corresponds to an equivalent of 10^4 electrons from the charge sensitive preamplifiers which is comparable to the measured rms noise.

5 Conclusions

A major design goal of the AXAF High Resolution Camera is to achieve the best possible spatial resolution with minimum distortions in image quality over a large field of view. The charge division readout system based on a crossed grid charge detector with periodic electronic sampling has been shown to be an acceptable solution. Models for the distortions and differential non-linearity that may arise from incomplete charge collection show that these effects can be accurately calibrated and corrected if the spillover is relatively small. The electronic noise considerations associated with multi-tap fine position algorithms lead to a readout design that uses the least number of amplifiers consistent with the charge spillover constraints. For the HRC we find that a three tap algorithm can be used and that a simple linear correction for charge spillover distortions is accurate to better than $6\mu m$ anywhere between amplifier taps.

The best measured resolution of the HRC has demonstrated that the design goal of FWHM=$25\mu m$ can be achieved. It is also possible to improve upon this result by using MCPs with smaller pore size and developing electronics with lower noise levels. Both of these areas are currently under study.

References

[1] S.S.Murray et al. *1984* Proposal to NASA for High Resolution Camera P1392-2-84.

[2] NASA Announcement of Opportunity AO No. OSSA-3-83 Advanced X-Ray Astrophysics Facility August 15, 1983.

[3] R.Giacconi et al. *1979* Ap.J. **230**.540.

[4] E.Pfeffermann et al. *1986* Proc. SPIE Berlin FGR.

[5] J.P.Henry et al. *1977* Proc. SPIE **106**.163.

[6] W.B.Colson et al. *1973* Rev. Sci. Instr. **44**.1694.

[7] E.M.Kellogg et al. *1976* Rev. Sci. Instr. **47**.282.

[8] G.W.Fraser et al.

[9] J.E.Grindlay *1988* private communication

[10] J.H.Chappell and S.S.Murray in preparation

[11] G.Knapp *1977* Trans. Nucl. Sci. IEEE

[12] S.S.Murray and J.H.Chappell in preparation

Position Modeling for the AXAF
High Resolution Camera (HRC)

J.H. Chappell and S.S. Murray
Harvard - Smithsonian Center for Astrophysics
Cambridge, MA 02138

Abstract

The High Resolution Camera (HRC) is one of four instruments selected to fly on the NASA Advanced X-Ray Astrophysics Facility (AXAF) [1]. The HRC is designed to detect single X-ray photon events in the soft X-ray energy range from 0.1 to 10. KeV. The measured spatial resolution (FWHM) is 25 μm over a 100 cm^2 detecting area. This paper investigates the accuracy and limitations of the position algorithm used with the coarse/fine resistive wire readout system.

1. Introduction

In order to understand the limitations of our imaging system, we need to investigate how the position algorithms are sensitive to various detector parameters such as the exiting MCP charge distribution function, tap spacings, amplifier gain effects, and amplifier noise. We begin our studies by constructing a model of the charge collection mechanism. From this model, we are able to investigate the various parameters that effect the errors in the position calculations. We then compare the modeling results to the measured parameters from the detector.

2. Instrument Configuration

The detector system consists of four major components, the UV/ion shield, microchannel plates, the crossed grid charge detector, and the anticoincidence shield. These components are shown in Figure [1]. The detector system is discussed in detail in Reference [1].

The charge cloud produced by the MCP's is accelerated toward the free standing orthogonal wire grid. The wire grid is consists of two isolated wire planes. Each plane is a series of parallel wires 100.μ in diameter placed on 200 μ centers. The grid potential is maintained at ~ +300V with respect to the rear MCP which is maintained at ground potential. The potential on the grids are balanced such that each plane captures 50% of the charge cloud.

In each plane, the wires are resistively coupled by 10K ohm thin film resistors. Every 8-th wire is connected to a charge sensitive amplifier (tap).

3. Charge Collection Modeling

We begin our investigations by constructing a model that describes how the charge cloud is distributed and collected on each tap. Our one-dimensional model begins with the following assumptions:

1. That the discrete charge collecting area behaves as a continuous area.

2. That if a charge $\Delta Q(x)$ is deposited on a ΔX length of wire centered at position x, then the charge will divide between the two adjacent taps proportional to the distance to each tap according to Ohms Law.
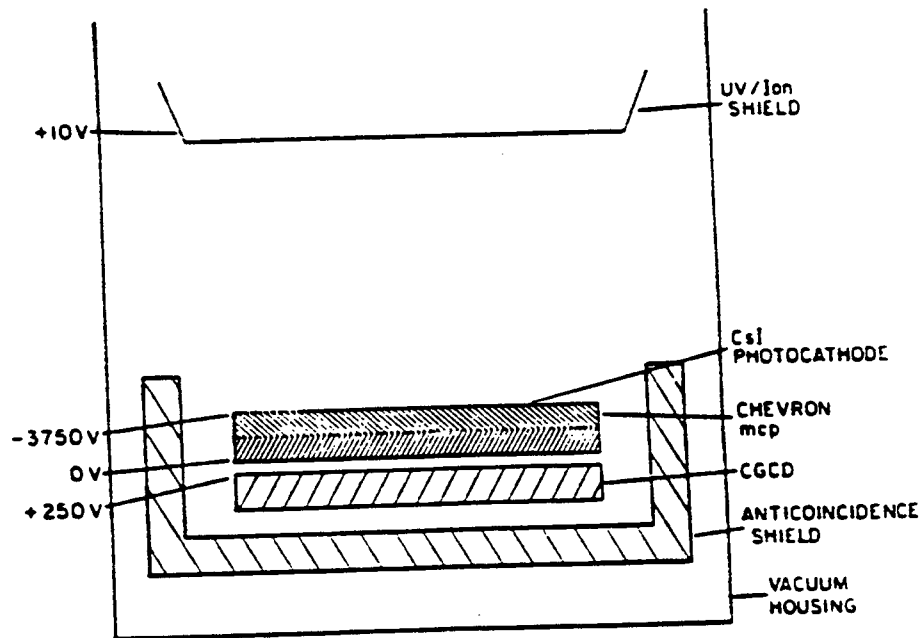
Figure 1: Schematic Diagram of HRC

The charge collected on two adjacent taps due to a charge injection between the taps is given by

$$Q_i = \frac{(X_{i+1} - x)}{(X_{i+1} - X_i)} \Delta Q(x)$$

$$Q_{i+1} = \frac{(x - X_{i+1})}{(X_{i+1} - X_i)} \Delta Q(x)$$

Where i represents the tap number, X_i is the tap position, and Q_i is the charge collected on the i-th tap. If we inject a series of discrete charges between two adjacent taps, then the charge collected at the taps can be expressed by

$$Q_i = \sum_{j=1}^{n} \frac{(X_{i+1} - x_j)}{(X_{i+1} - X_i)} \Delta Q_j(x)$$

4. A Skewed distribution:

$$\text{for } x < x_0: \qquad f(x) = \frac{1}{\sigma \sqrt{2\pi}} \exp\left[-\frac{1}{2}\left[\frac{x - x_0}{\sigma}\right]^2\right]$$

$$\text{for } x \geq x_0: \qquad f(x) = \frac{1}{\sigma \sqrt{2\pi}} \exp\left[-\frac{1}{2}\left[\frac{x - \mu}{\sigma}\right]^2\right] + \exp(-\mu x)$$

This asymmetric function is a combination of a Gaussian plus exponential distribution. Where x_0 is the center of the distribution and σ is the standard deviation of the distribution (2.36σ = FWHM).

These input distribution functions are shown in Figures [2a-d]. These Figures show various distribution widths as a function of tap position.

6. Modeling Results - Position Calculation vs. Charge Distribution Function

We have computed the charge collected at each tap position for various distributions and injection positions. Using the calculated charge on each tap, we have calculated the centroid position of these distributions using a three tap algorithm. Figures [3a-d] show the calculated vs. the actual centroid position for the various distributions using a 3-tap model.

In all cases, the position algorithm correctly predicts the centroid position of the charge cloud if the total charge collected is within the tap-algorithm boundary. If the charge cloud extends beyond the tap-algorithm boundary, the position is incorrectly computed. This error manifests itself as "gaps" in the calculated positions. Figures [4a-d] show the relative position error as a function of the tap position.

Figures [5a-d] show the excess charge spillover for various charge cloud distribution widths as a function of tap position. Figures [6a-d] show the resulting gap width as a function of the percent of charge that is lost or unused in the position algorithm. In general the accuracy of the position algorithm is independent of the charge cloud distribution function when the total charge is used in the calculations. Figure [7] shows a flat field illuminated X-ray image using a three tap algorithm to calculate the photon positions. The effect of the charge spillover is clearly evident.

7. Fine Position Correction Factors

There are several remedies available to correct the error in the fine position calculation. Ideally, one would select a tap spacing and fine position algorithm that would incorporate all of the exiting charge. Due to amplifier noise consideration (Reference[1]), the optimal fine position algorithm uses three taps. This leaves only the adjustment of the tap spacing such that all of the charge is collected on three taps. Increasing the tap spacing places a larger constraint on the accuracy of the digitizing electronics (ADC). As the tap spacing increases, the accuracy of the ADC must increase to preserve the spatial resolution.
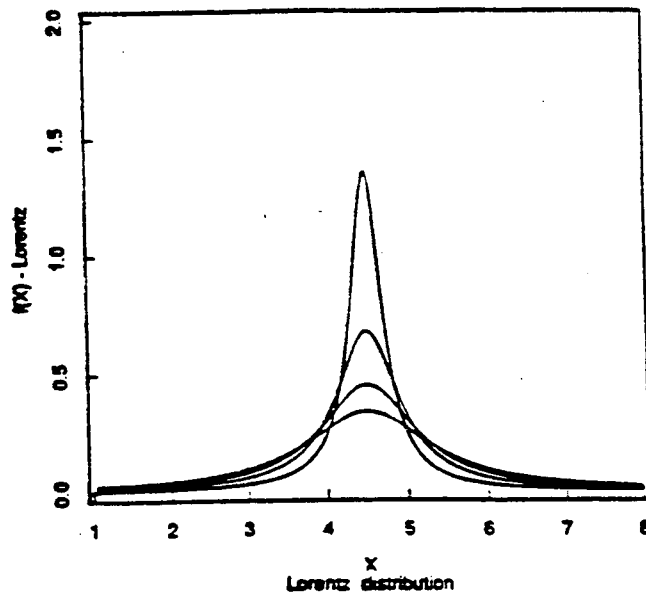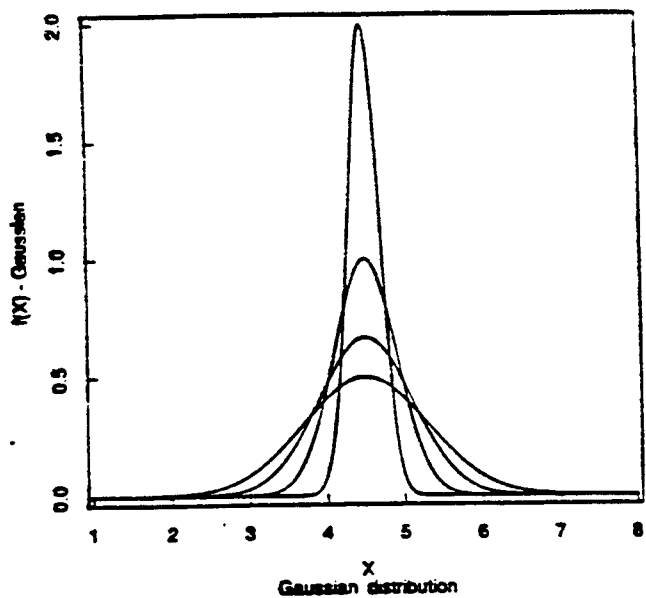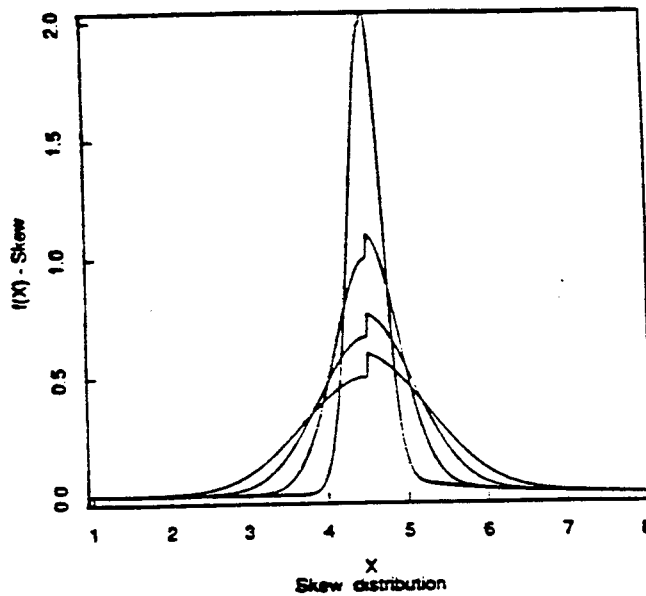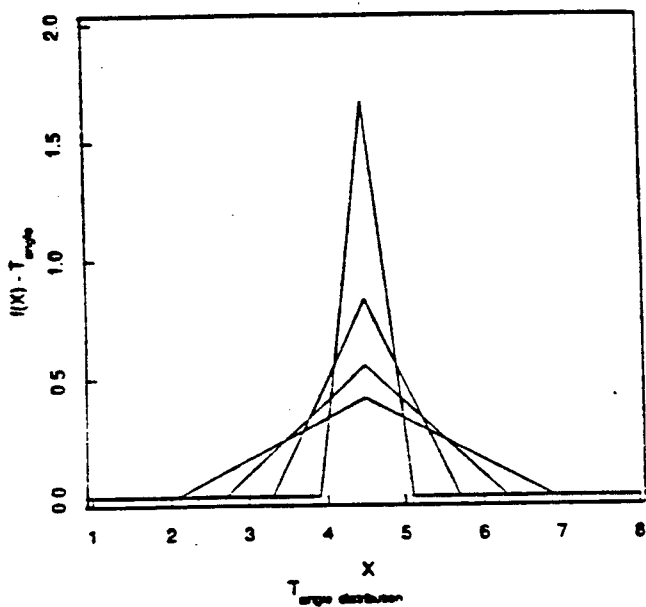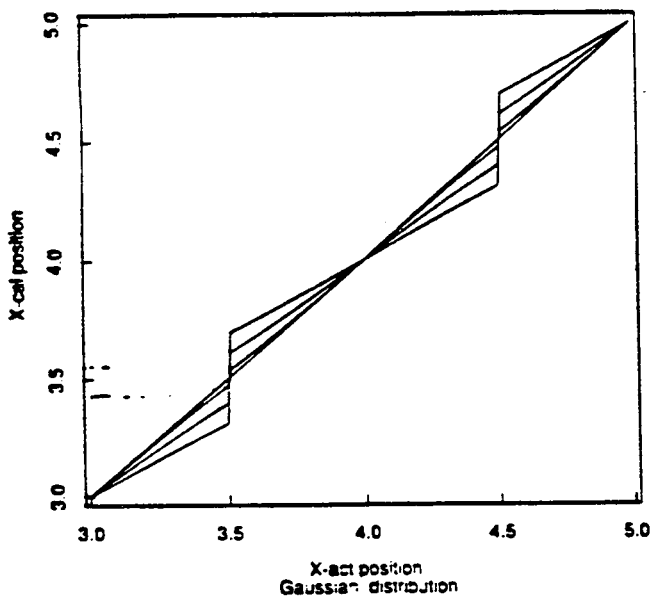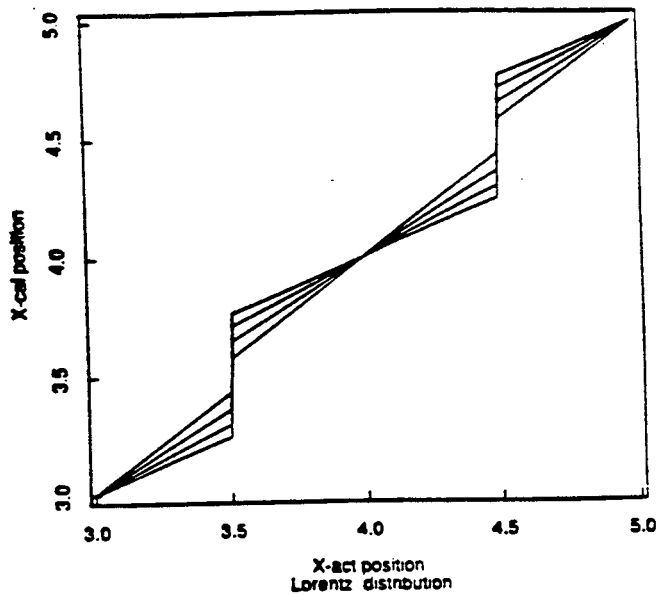
Figure 2: Input Charge Cloud Distributions

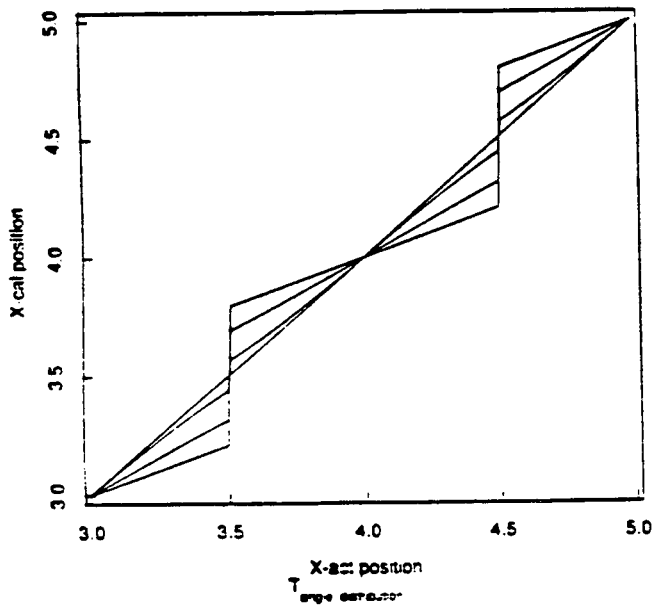Position Modeling 3-tap model

Position Modeling 3-tap model

X-act position
Gaussian distribution

X-act position
Lorentz distribution

Position Modeling 3-tap model
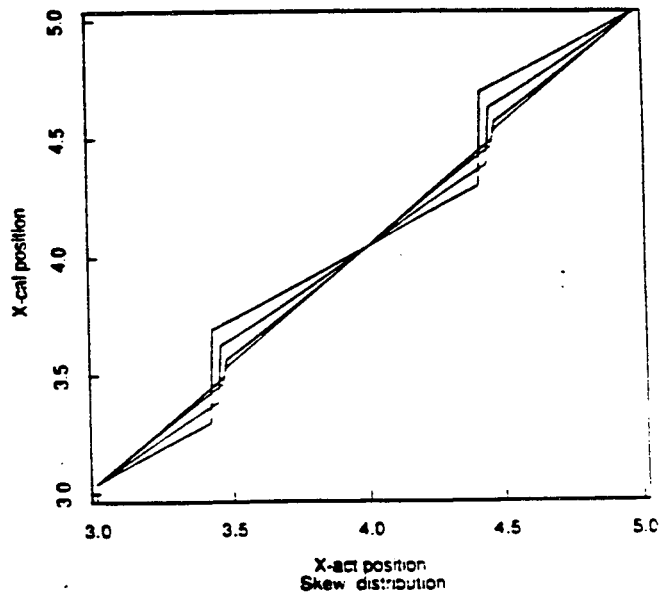
Position Modeling 3-tap model

X-act position

X-act position
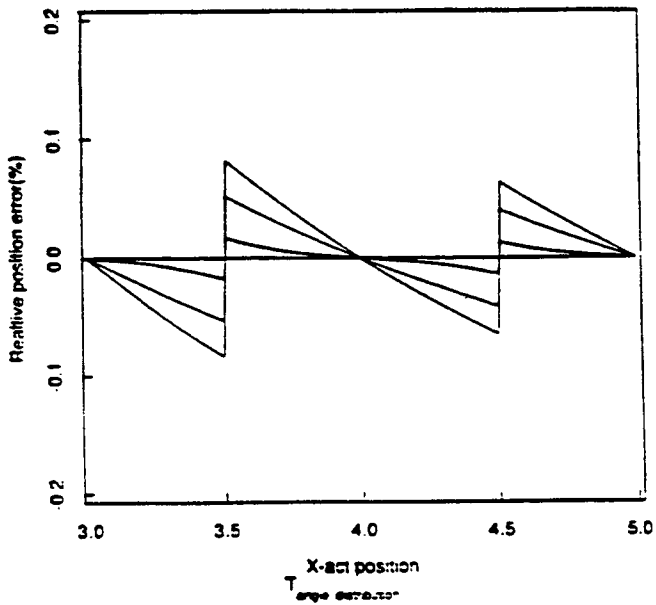Skew distribution

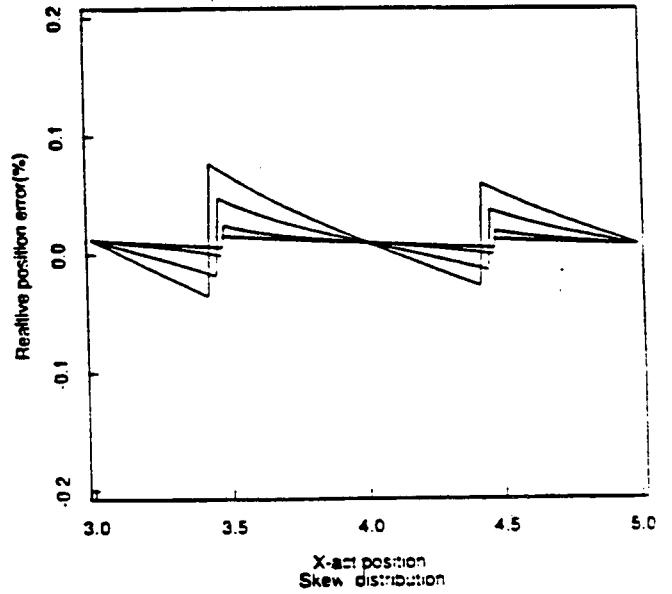Figure 3: Calculated vs. Actual Centroid Positions
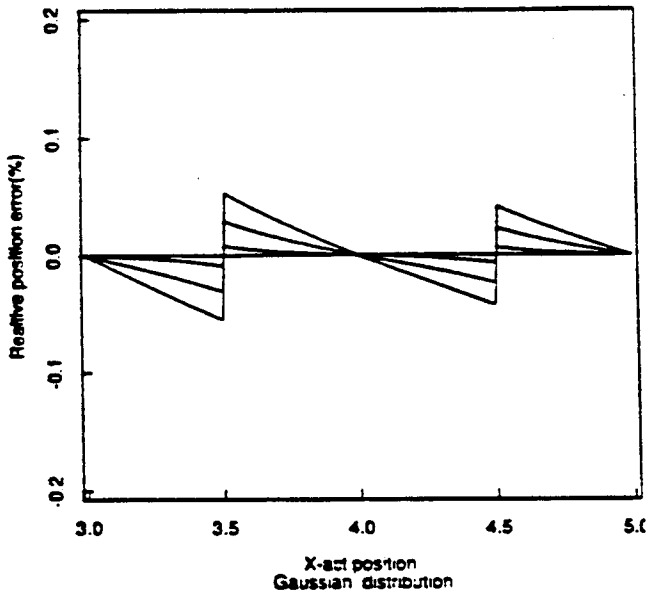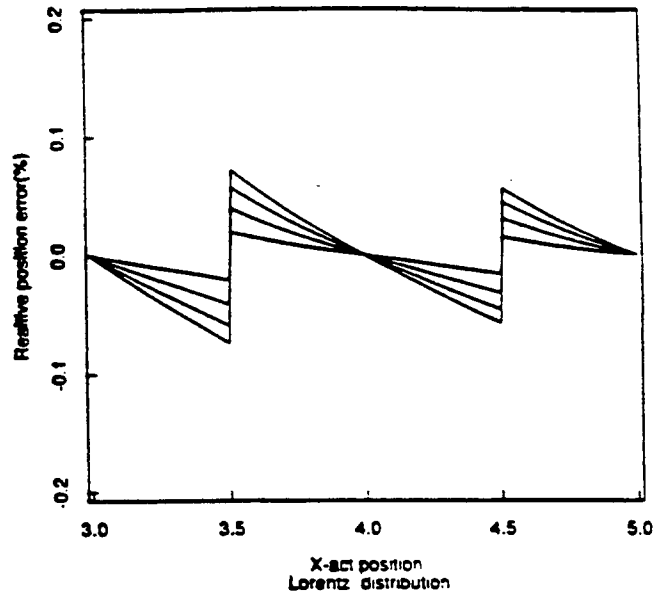
Figure 4: Relative Position Error vs. Tap Position

$$Q_{i+1} = \sum_{j=1}^{n} \frac{(x_j - X_{i+1})}{(X_{i+1} - X_i)} \Delta Q_j(x)$$

Where n is the number of charges injected. For a continuous charge distribution, the charge collected can be expressed by

$$Q_i = \int_{X_i}^{X_{i+1}} \frac{(X_{i+1} - x)}{(X_{i+1} - X_i)} dQ(x) = L^{-1} \int_{X_i}^{X_{i+1}} (X_{i+1} - x) j(x) dx$$

$$Q_{i+1} = \int_{X_i}^{X_{i+1}} \frac{(X_{i+1} - x)}{(X_{i+1} - X_i)} dQ(x) = L^{-1} \int_{X_i}^{X_{i+1}} (X_{i+1} - x) j(x) dx$$

Where $j(x)$ is the linear charge density distribution function and L is the separation distance between the taps. If the charge distribution extends over n-taps, the collected charge at each tap is given by

$$Q_i = L^{-1} \int_{X_i}^{X_{i+1}} (X_{i+1} - x) j(x) dx$$

$$Q_{i+1} = L^{-1} \left\{ \int_{X_{i+1}}^{X_{i+2}} (x - X_{i+1}) j(x) dx + \int_{X_{i+1}}^{X_{i+2}} (X_{i+3} - x) j(x) dx \right\}$$

$$Q_{i+2} = L^{-1} \left\{ \int_{X_{i+2}}^{X_{i+3}} (x - X_{i+2}) j(x) dx + \int_{X_{i+3}}^{X_{i+4}} (X_{i+4} - x) j(x) dx \right\}$$

$$\cdot$$
$$\cdot$$
$$\cdot$$

$$Q_{i+n} = L^{-1} \int_{X_{i+n-1}}^{X_{i+n}} (x - X_{i+n-1}) j(x) dx$$

4. Position Algorithms

With the above formalism in place, we can calculate the charge collected on each tap as a result of the injection of different charge distributions. We will use use this information to explore the accuracy and limitations of the position algorithm as a function of the charge cloud distribution.

The event position is defined by the sum of a coarse and a fine position measurement.

$$X = X_{coarse} + X_{fine}$$

The coarse position of an event is determined by locating the tap X_{coarse} that has collected the largest charge from the wire grid. The fine position is determined by a centroiding algorithm. The fine position algorithm uses the charge collected on the adjacent amplifiers (taps) to determine the position of the event with respect to the X_{coarse} position. The derivation of the fine position algorithm is discussed in Reference[1].

The three-tap fine position algorithm uses the charge collected on the center X_i tap plus the charge collected on the two taps located on ether side, X_{i-1} and X_{i+1}.

$$X_{fine (3)} = \frac{(Q_{i-1} - Q_{i+1})}{(Q_{i-1} + Q_i + Q_{i+1})}$$

Q_i represents the charge collected on the X_i tap.

5. MCP Charge Cloud Distribution Functions

The next step is to model the effects of different charge cloud distribution functions with the fine position algorithm. We have selected four charge cloud distribution functions to model:

1. A Gaussian distribution:

$$f(x, x_o, \sigma) = \frac{1}{\sigma \sqrt{2 \pi}} \exp \left[-\frac{1}{2} \left[\frac{x - xo}{\sigma} \right]^2 \right]$$

Where xo is the center of the distribution and σ is the standard deviation of the distribution (2.36σ = FWHM).

2. A Lorentzian distribution:

$$f(x, x_o, \Gamma) = \frac{1}{\pi} \frac{\frac{\Gamma}{2}}{(x - x_o)^2 + \left[\frac{\Gamma}{2} \right]^2}$$

Where x_o is the center of the distribution and Γ is the full width at half maximum (FWHM). The standard deviation of the distribution is $2.35\sigma = \Gamma$.

3. A triangular distribution:

$$f(x, x_o, \Gamma) = a(x - x_o) + b$$

For $x < x_o$; i $a = 2 / \Gamma$; $b = 1 - \frac{x_o}{2\Gamma}$ For $x \geq x_o$; i $a = -2 / \Gamma$; $b = 1 + \frac{x_o}{2\Gamma}$

Where Γ is the FWHM of the triangular distribution function.

Position Modeling 3-tap model

Position Modeling 3-tap model

Position Modeling 3-tap model

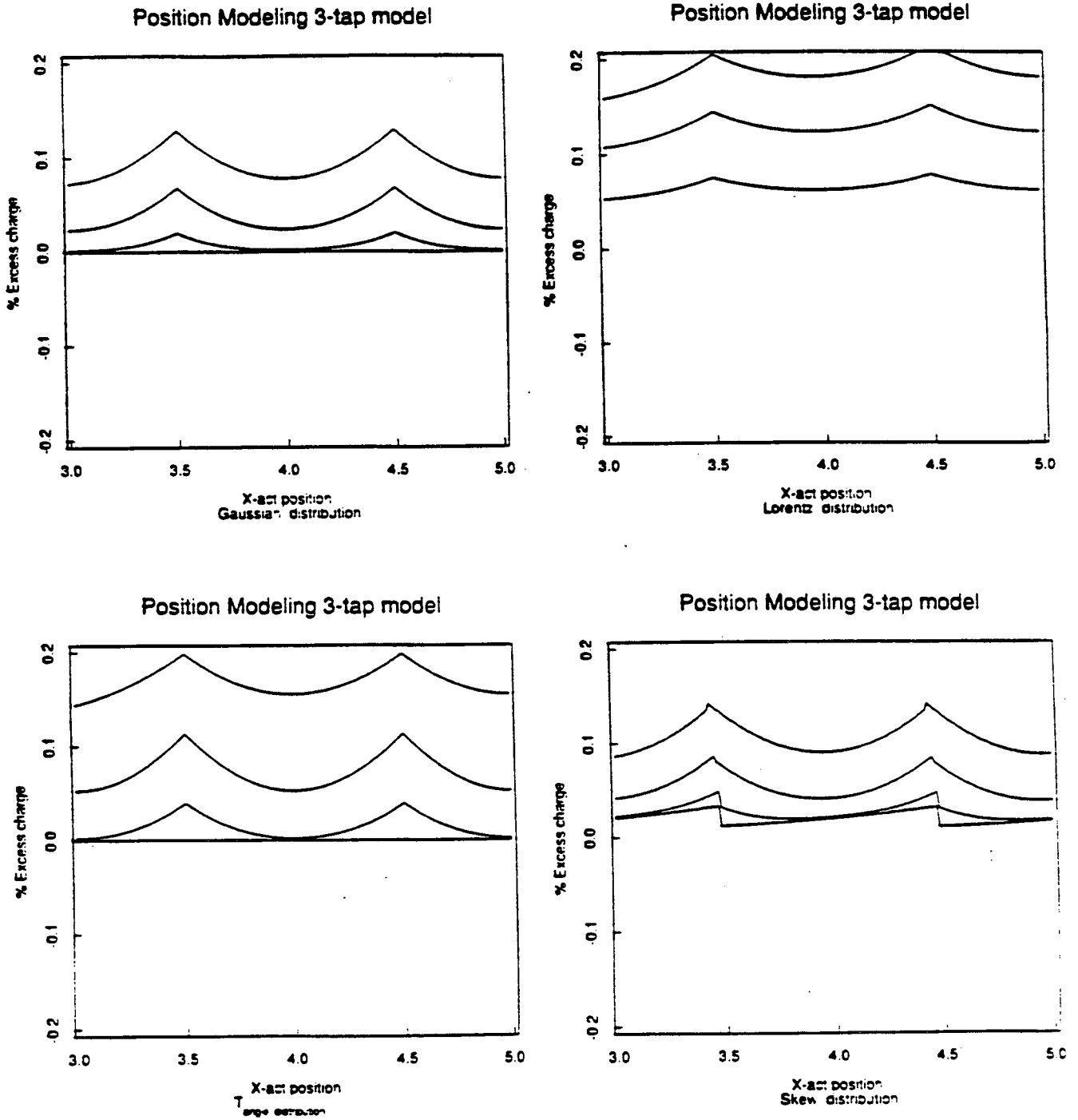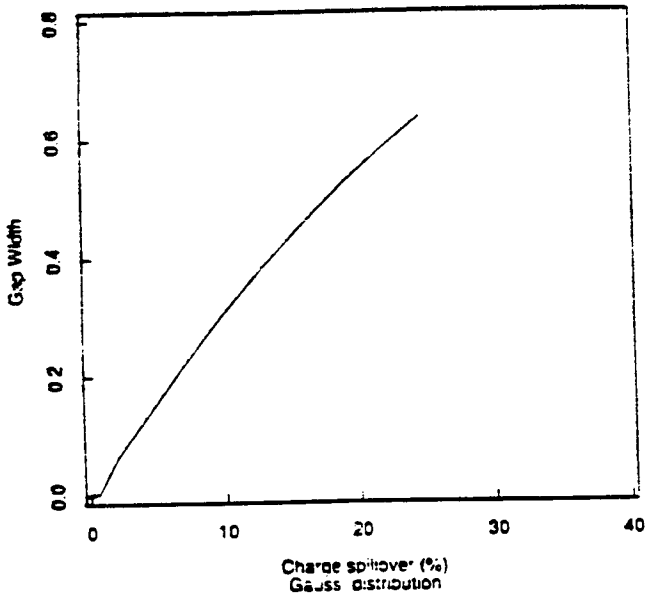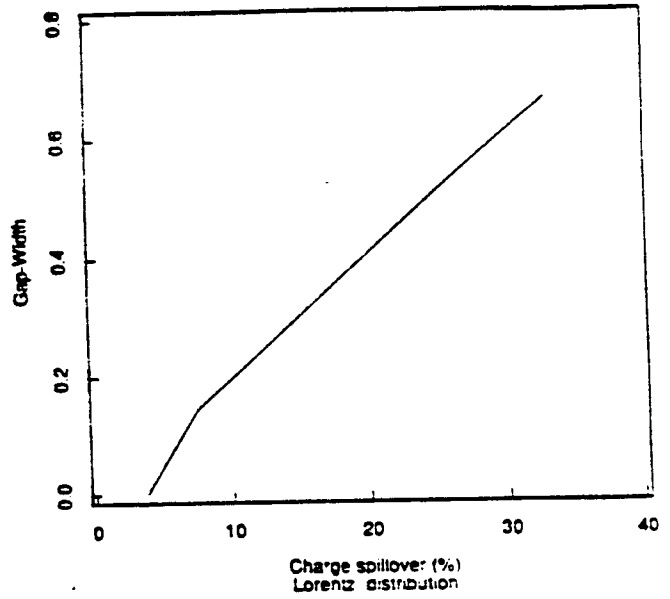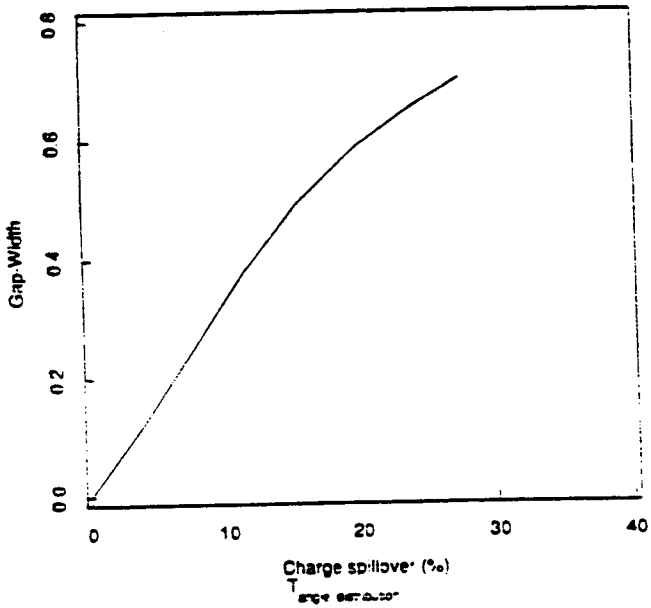Position Modeling 3-tap model

Figure 5: Charge Spillover vs. Tap Position

Position Modeling 3-tap model

Position Modeling 3-tap model

Position Modeling 3-tap model

Position Modeling 3-tap model

Charge spillover (%)
Gauss distribution

Charge spillover (%)
Lorentz distribution

Charge spillover (%)
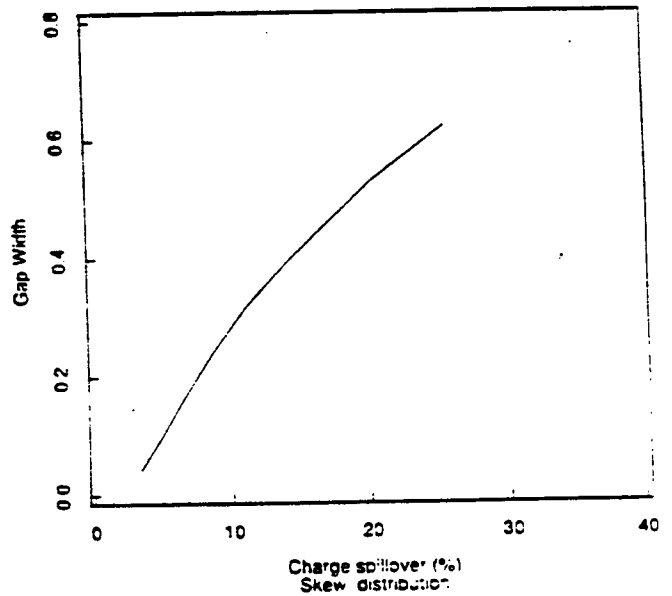Large separator

Charge spillover (%)
Skew distribution

Figure 6: Gap Width vs. Charge Spillover

Another correction method is to modify the three tap algorithm to account for the loss of charge. For our detector system, we have chosen to correct the positional error by modifying the fine position algorithm. The new fine position can be expressed in terms of a linear expansion of the originial three tap fine position.

$$X_{linear/fine(3)} = B * X_{fine(3)}$$

Figure [8] shows a plot of the difference between the actual and calculated position using the unmodified three tap position algorithm. The positional error becomes greater the further away from center tap. The standard deviation in the position error for the uncorrected algorithm is 0.013 tap (21.8μm).
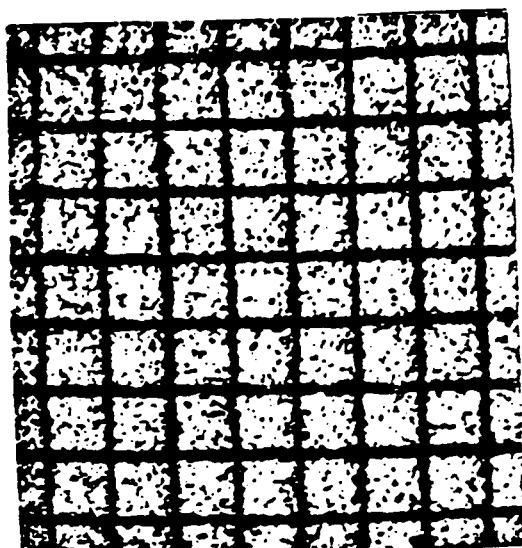
Figure 7: X-ray Flat Field Image
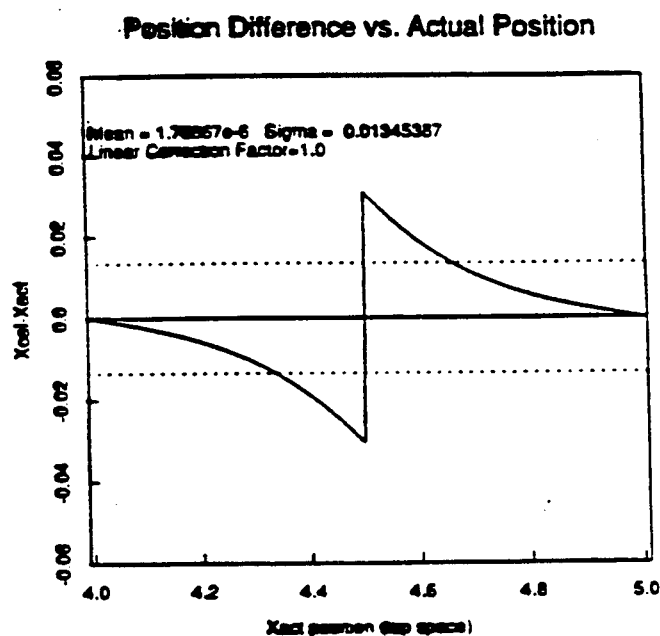
Figure 8: Relative Spatial Error vs. Tap Position

In Figure [9] shows the same plot using a linear correction factor to the fine position algorithm. By applying a linear correction factor to the fine position algorithm, the fine position error can be reduced significantly. The standard deviation in the position error for the corrected algorithm is 0.003 tap (4.9μm). For a given charge cloud distribution function one can determine an optimum linear correction factor. The results for a Gaussian charge cloud is shown in Figure [10].
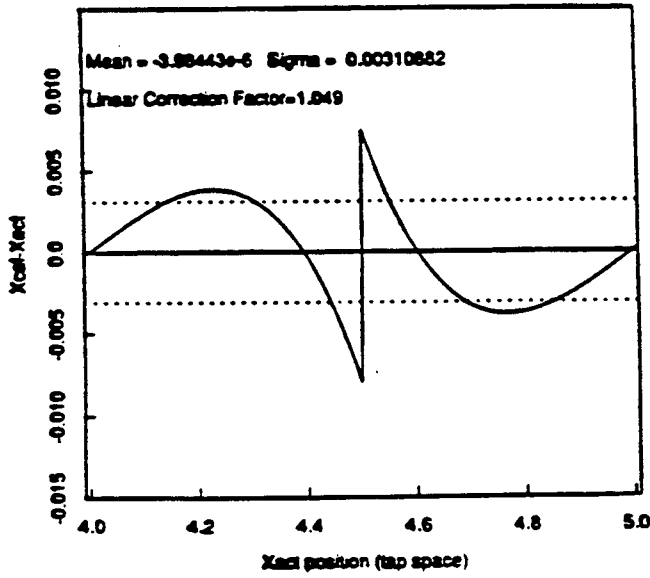
Figure 9: Relative Spatial Error With a Linear Correction Factor vs. Tap Position
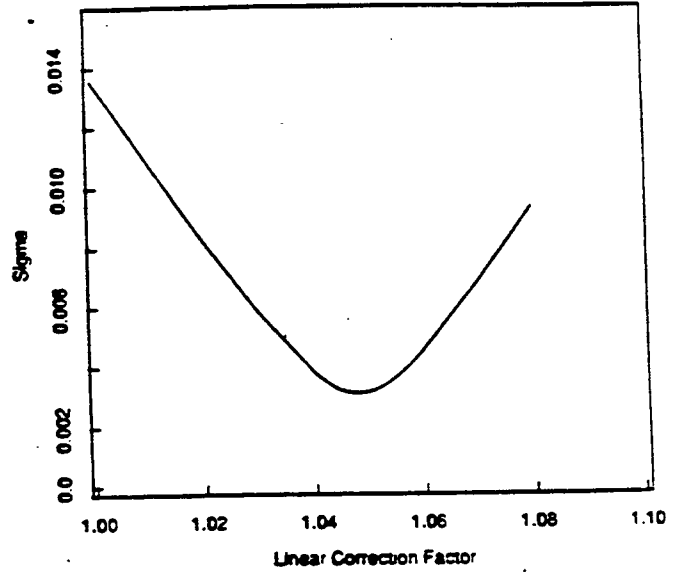
Figure 10: Standard Deviation in the Spatial Error vs. The Linear Correction Factor

We can further improve the fine position algorithm by combining a linear plus a quadratic correction factors.

$$X_{quadraticfine\,(3)} \;=\; A \;*\; X^2_{fine\,(3)} \;+\; B \;*\; X_{fine\,(3)}$$

Figure [11] shows the residual errors over a tap region using this algorithm. The σ has now been reduced to .0004 tap (1.14 μm) over the region.

Figure 11: Relative Spatial Error With a Quadratic Correction Factor vs. Tap Position

8. Actual Charge Cloud Distribution Function
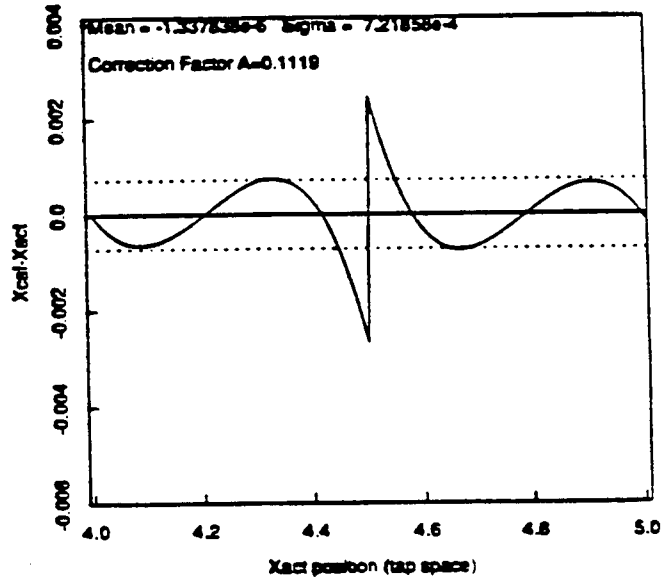
In order to measure the exit charge distribution, the X-ray beam was colliminated such that the region of exposure was centered on a single tap. Our detector system has the capability of measuring the collected charge on 8 taps centered on about the coarse position tap. For our detector configuration, the charge distribution was best fit by a Lorentzian function as shown in Figure [12a-b]. The shape of the charge cloud remained roughly constant for any position across the detector.

MCP Charge Distribution x-axis

Lorentz Fit Parameters
A = 217.8534
Xo = 4.0099
Γ = 0.4047

Tap Number

MCP Charge Distribution y-axis

Lorentz Fit Parameters
A = 269.1207
Xo = 4.0122
Γ = 0.617

Tap Number
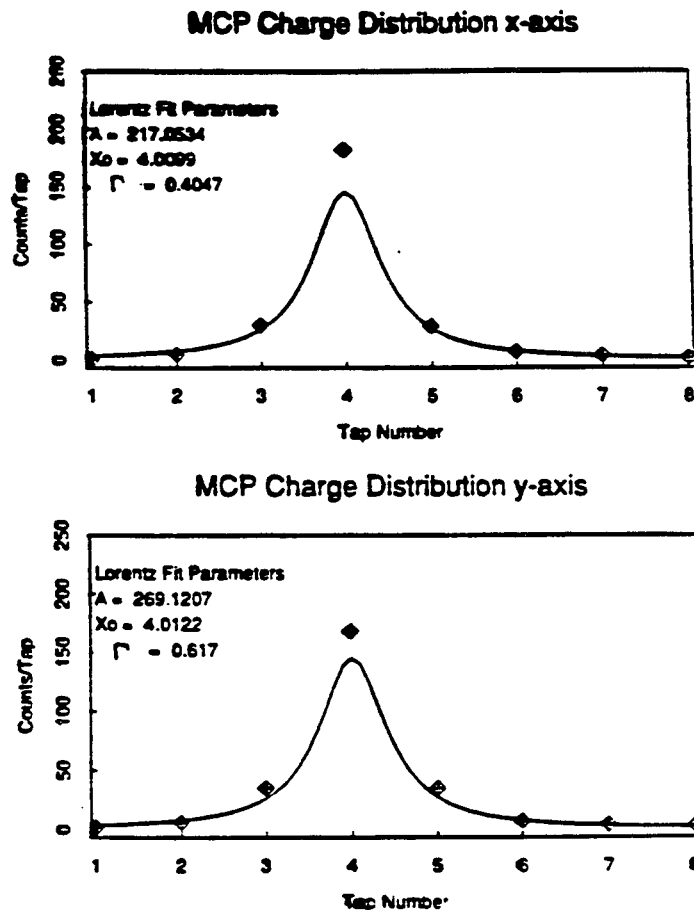
Figure 12: Measured Charge Cloud Distribution Function vs. Tap Position

9. Actual Position Calculations

The next step was to compare the modeling results using this best fit distribution function with the actual detector performance. Figure [13] shows a projection of a modeled flat field X-ray image using a Lorentzian distribution function with an uncorrected three tap algorithm to calculate the photon positions. The model predicts a gap width of ~60 pixels. Figure [14] shows a projection of an actual flat field X-ray image using an uncorrected three tap algorithm to calculate the photon positions. In this data set, the gap with is ~63 pixels. Using a mask of an array of pinholes we have verified that the linear plus quadratic correction factors do indeed correct the image distortions as predicted (Reference[1]).
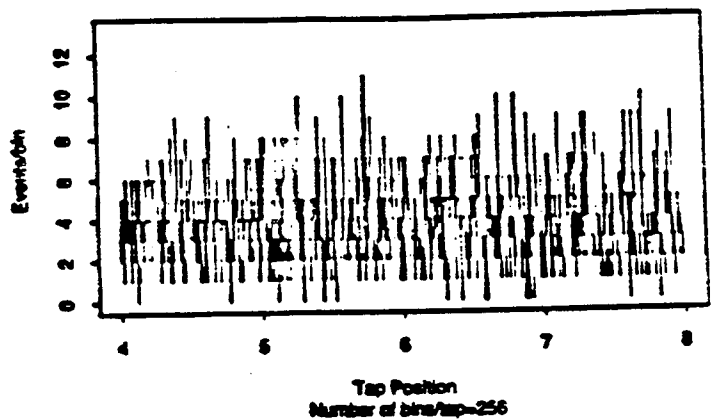
Calculated Event Distribution
Total number of events=4000
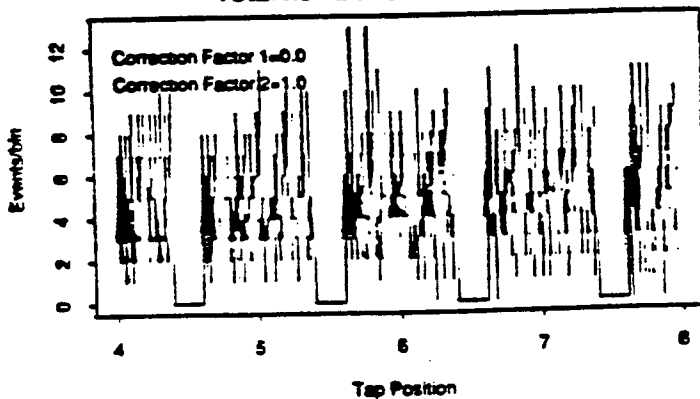
Figure 13: Modeled Data: a) Actual Input Projection vs. Tap Position.
b) Calculated Position Projections vs. Tap Position
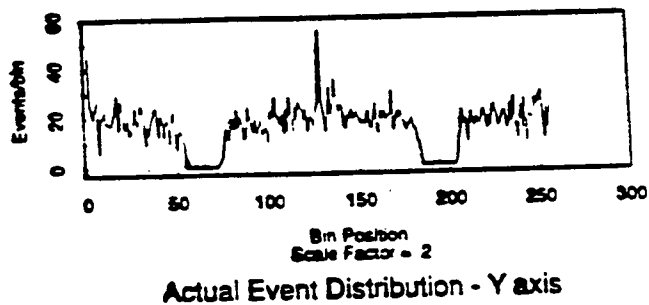
Actual Event Distribution - Y axis
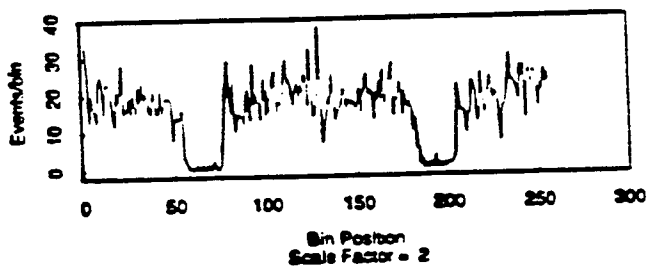
Figure 14: Measured Data: Calculated Position Projections vs. Tap Position

10. Modeling Results - Position Calculation vs. Amplifier Gain Variations

In the above idealized model, there were no assumptions made with respect to a real electronic charge collection system. The next task is to incorporate amplifier gain variations at each tap position. Figure [15] depcits a normalized amplifier gain map. The gain of the amplifier at tap position 6 is set 2% higher than the other amplifiers. Figure [16] shows the spatial distortions produced by this single amplifier gain variation. The positions effected range from tap 4.5 thru 7.5. To insure spatial uniformity over the 100 cm^2 detecting area, we have found it necessary to keep the amplifier gain variations below the 2% level.
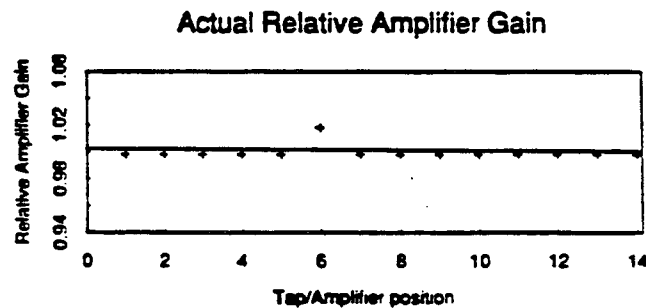
Figure 15: Relative Amplifier Gain Map vs. Tap Position
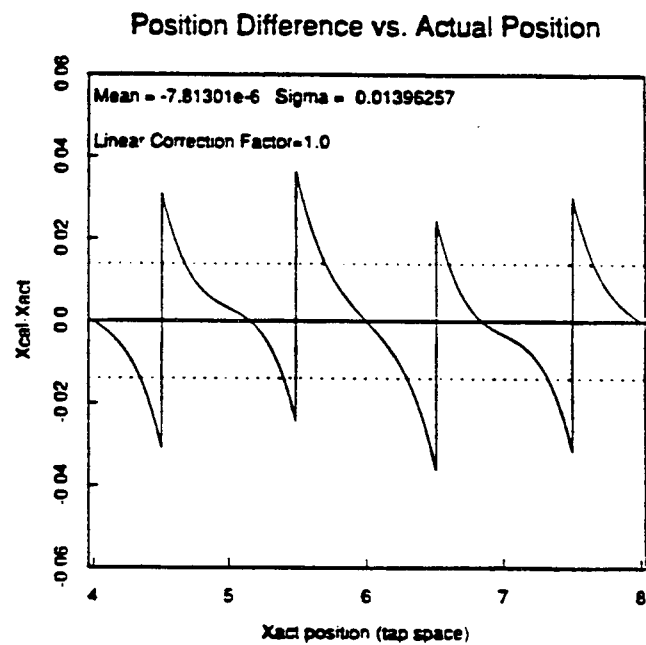
Figure 16: Relative Spatial Error vs. Tap Position

11. Conclusions

We have constructed a position model that correctly predicts the behavior of our coarse/fine resistive readout system. As a result of the modeling we have observed the following:

- The modeling results indicate that the three tap position aligorithm correctly predicts the centroid position of the charge cloud when the total charge of the event is used in the calculation. The standard three tap algorithm incorrectly calculates the position when the charge cloud extends beyond the three tap boundary. An artifact of operating in this invalid range produces "gaps" in the calculated positions.

- We have constructed and verified simple modifications to the three tap algorithm that correct the position calculations.

- The modeling results indicated that the position calculations are insensitive to symmetric charge cloud distribution functions.

- We have modeled and verified the effects of amplifier gain variation on position calculations.

- When using the measured exiting charge cloud distribution from the MCP, the model correctly predicts the behavior of our imaging system.

References

[1] S.S. Murray and J.H. Chappell SPIE Vol. 982, X-ray Instrumentation in Astronomy II (1988)

10   Appendix I

1. Imaging Performance

Imaging performance of a detector is generally characterized in three ways: spatial resolution, distortion or differential nonlinearity, and uniformity of efficiency. The most general of these characteristics is resolution, because distortion and non uniform efficiency can both affect the resolution. Also, distortion and non-uniform efficiency can be calibrated out to desired accuracy.

2. Uniformity of Efficiency

The uniformity of efficiency can be affected by factors such as the uniformity of the photocathode coating. To measure the uniformity, the detector is illuminated by a uniform X-ray beam. A histogram of the number of pixels against the counts per pixel yields a dispersion which can be compared with that expected from the counting statistics to estimate the degree of nonuniformity. An example is shown in Figure 2.

3. Resolution

One way that resolution is determined is by measuring the detector's response to bar patterns in a test mask. The effect is deconvolved with the slit width to obtain a numerical estimate of the resolution under the assumption that the point spread function is a one-dimensional Gaussian. More complex two-dimensional resolution determinations can be made using pinholes and deconvolving with two-dimensional Gaussians. For ease of analysis, and because the cgcd is basically two one-dimensional detectors, we use the simple one-dimensional measures in each of the x and y directions. Measured resolutions are shown in Table 1.

TABLE 1
Measured MCP Resolutions

Instrument	FWHM (μm)
Einstein	33
ROSAT	20
HRC prototype	<25

Spatial resolution limitations can be divided into two categories (Lapington):

1. Those which impose an uncertainty, or noise on the signal without altering its mean value (statistical errors).

2. Those which produce a geometrical distortion of the image (systematic errors).

Included in the first category are true noise contributions (*e.g.,* signal variations, electronic noise, etc.), and background events as well. These will be discussed in some detail below. Included in the second category are such contributions as the MCP pore structure and those things which directly affect the determination of the charge cloud centroid such as cgcd wire uniformity and resistor uniformity. Those terms specific to geometrical distortions are characterized by one of the remaining image quality tests, that of differential nonlinearity.

Consider first those resolution limitations which impose an uncertainty on the signal without altering its mean value. These terms are broadly called "noise", although in the literature the terms "noise" and "background" are frequently interchanged. Under ordinary flight conditions, the background is derived from three components: (1) diffuse X-rays, (2) externally induced events from cosmic and gamma rays and surrounding radioactivity, and (3) internally generated signals from the MCPs or the internal MCP noise. In the context of modeling, the issue of diffuse X-rays is not a factor. Cosmic rays account for about 0.015 counts/cm^{2}s of the background (excluding diffuse X-rays). The HRC anticoincidence shield can be expected to detect more than 99% of all ionizing particles, reducing this component of background. About 3% of gamma rays passing through the detector will cause a detectable interaction. The electrons produced by them largely generate low amplitude events that can be discriminated out by appropriately setting the event threshold high enough. (In the laboratory environment, less than 5% of the background is caused by cosmic rays or other forms of natural (external) radioactivity.) The last component to consider is the internal microchannel plate background. Its count rate is about 0.2 counts/cm^{2}s at sea level, independent of X-ray bandwidth. Experiments have shown that the background is not predominantly thermionic emission. Sources of this background, therefore, are presumably residual ion feedback, defects in the tubes (*i.e.,* cracks and whiskers) that are emitting electrons via field emission, and internal radioactivity. Most MCP glass contains about 5% by weight of potassium. It has been found that ^{40}K emission accounts for both the observed count rate and pulse height shape of Fig. 3, so that internal radioactivity dominates ($\geq 90\%$) the internal background of the MCP operated at pressures below 10^{-6} mbar. HRC expects to employ MCPs made with low radioactivity glass, reducing the internal background by at least a factor of ten.

The remaining noise components that affect resolution are related to the anode and readout. In particular, the full width half maximum spatial resolution (Δx) can be given as the quadratic sum of several terms (adapted from Fraser, eqn 3.2).

$$\Delta x = [2.35\{\sigma_a^2 + \sigma_d^2 + \sigma_e^2 + w_f\sigma_f^2 + \sigma_{g1}^2 + \sigma_{g2}^2 + \sigma_p^2\} + D^2]^{\frac{1}{2}}$$

where

a:	noise arising from the grid	
d:	digitization of the position signals in the ADCs, or finite resolution in the signal processing chain	
e:	noise arising in the preamplifiers	
p:	partition noise resulting from the Poisson statistics on counting a finite number of electrons on a small number of discrete electrodes	
f:	transverse displacement of activated channels from the original positions of X-ray interaction on the interchannel web, where w_f is the fraction of all events originating on the interchannel web.	
g1:	jitter in the charge cloud centroid arising in the interplate gap	
g2:	jitter in the charge cloud centroid arising in the MCP-readout gap	
D:	channel diameter	
σ_i	rms position error introduced by factor i	

Four of these terms (a,d,e,p) are of the first type, imposing an uncertainty on the signal without changing its mean value. Of these four, all are effectively included in the modeling studies as noise. The others terms in the equation are of the type that contribute to a geometrical distortion of the image, or affect the centroid determination. No matter what type of readout is used, the fundamental limit to resolution is the channel diameter. In this equation, it is not clear where distortion-type contributions from the electronics are included. However, distortion contributed by the electronics at each tap is explicitly considered in the modeling. For convenience, we may simply divide the terms into two types; systematic errors, which we can correct for, and statistical errors, which we cannot.

4. Distortion

Distortion in the image can arise in the MCPs or in the electronic processor. Distortion in the MCPs arises generally from packing defects. Electronic distortion is directly studied by the modeling. As will be seen, it can be caused by factors such as mismatched preamplifier gain. To measure the distortion, an image of a mesh pattern or uniform field of holes is obtained. The rms deviation of the measured spacing relative to the expected position gives the distortion or differential nonlinearity. As shown in Figure 3, tests on the HRC prototype showed a differential nonlinearity of less than 1% (less than 2.5 μm) using a single linear correction factor in the position algorithm (which is needed to correct for "gaps" as described in Section 4.2).

To: File
From: J. Gomes
Subject: Estimated Hybrid Preamp performance w/ low noise plates
Date: 7/29/94

The paragraphs below represent a "back of the envelope" calculation of expected imaging performance of the hybrid preamplifiers operating with the low noise (and low gain) channel plates. The result of this calculation shows that the CEI spatial resolution requirements would be met using the hybrid preamplifiers now under development with the low noise channel plates.

The now familiar algorithm for the HRC fine position is

$$FP = (C-A)/(A+B+C)$$

where A, B, and C are the signals at three consecutive taps. When expressed in this form, the units of FP are taps, and the allowable range of FP is from -1/2 tap to +1/2 tap. In the HRC, the tap to tap distance is 0.0648 inches, or 1645.9 microns.

The HRC CEI specification paragraph 3.2.1.2 specifies that the HRC shall have a spatial resolution of 25 microns or less FWHM. For purposes of determining the amount of allowable electronic noise, it will be assumed that the electronic noise is responsible for the full 25 microns of signal spreading. Although this assumption cannot be entirely true, test experience suggests that that the electronic noise is at least dominant, so this assumption is likely to produce a reasonable result.

The spatial resolution is primarily a result of the electronic signal to noise ratio of the electronic system. The higher the signal level, the smaller the degradation of the resolution due to the noise. On the ROSAT program, the channel plates were operated at a gain of 3 to 5 X 10^7 electrons, which is also the approximate operating point for the standard HRC channel plates. On the other hand, HRC may opt to fly "low noise" channel plates, which have low dark current. These plates have the side effect of having a gain of only about 1.25 X10^7, which may increase the resolution of the instrument for the lowest pulse heights. The following development is an effort to estimate the noise performance of the HRC using the low noise plates.

With noise sources shown for each of the three channels in the algorithm, the fine position is expressed as

$$FP = ((C+n_c) - (A+n_a))/((A+n_a) + (B+n_b) + (C+n_c))$$

Since the sum of A+B+C is in the order of 6.25×10^6 electrons for each grid using the low noise plates, the lowest signals expected (about 25% of the peak) would be about 1.5×10^6 electrons. When the noise sources are added in quadrature (because they are independent), the total denominator noise is in the order of 1×10^4, which is negligible when compared to the denominator signal, and can be neglected. The overall pertubation due to noise can then be estimated as

$$nFP \sim 1645.9 * 1.414 n / (A+B+C) \text{ microns}$$

where n represents the noise on any of the identical, independent channels. Rearranging, n can be solved for.

$$n \sim (nFP * (A+B+C)) / (1645.9 * 1.414) \text{ electrons}$$

From the CEI, nFP=25 microns FWHM, and for a minimum signal of 1.5×10^6 electrons at the grids,

$$n \sim (25 * 1.5 \times 10^6) / (1645.9 * 1.414)$$

$$\sim 16113 \text{ electrons FWHM}$$

or $\quad = 6856 \text{ electrons rms}$

This figure represents the maximum allowable noise for image resolution within the CEI specification limits for the smallest signals of interest for channel plates having a nominal gain of 1.25×10^7.

Given the maturity of the hybrid design, and the experience of having tested more than 30 preamplifiers and having extensively modelled the preamp noise performance in SPICE, it is likely that all of the flight hybrids will perform well below their specified noise maximum, and close to the observed 4700 electrons rms level (when connected to simulated detector impedances) observed in laboratory testing.

This conservative analysis shows that the hybrid preamplifiers will perform well within the CEI resolution limits when operated with channel plates having 1.25×10^7 gain.

MEMORANDUM

To: Distribution
From: Jack Gomes
Subject: Justification for the HRC ADC size
Date: 4/11/94

The number of bits that the on-board A/D converters must have in order to be capable of addressing all pixels over the full dynamic range of pulse heights is estimated below:

Assumptions:

1. The HRC 3 tap algorithm has a range of +1/2 to -1/2 coarse positions, which is further subdivided into 256 pixels by ground based software. Each pixel is approximately 6 microns in size.

2. The algorithm is described by

$$Position = (a-c)/(a+b+c)$$

where a, b, and c are the three tap outputs to be centroided.

3. The dynamic range of pulse height required is less than or equal to 32:1, which should be reasonable for the HRC plates. (the EINSTEIN and ROSAT HRI instruments were 20:1)

The numerator of the algorithm must consist of at least 256 integers in order to fill each of the 256 pixels at a fixed signal pulse height. It should be noted that the "a" term is completely dominant at one end of the algorithm range, and the "c" term at the other. As an approximation, then, "a" and "c" each will have an ADC range of 128 pixels (or 7 bits) to cover the range of the algorithm at the assumed single pulse height, which would be the minimum pulse height for the system. For a pulse amplitude range of 32:1, an additional 5 bits of ADC range is required, making the total requirement 12 bits.

The current HRC design calls for A/D converters of 14 bits (implemented as 12 bit devices with 2 bits of prescaling). The design margin of 2 bits is accounted for as follows:

    1. HRC will employ converters with no missing codes over temperature, age, and device radiation life. This will require the budgeting of one of the spare bits.

    2. Based on the orbital aging effects of the ROSAT channel plates (20% in 2 years), the HRC budget for this effect is set at 1 bit (50% in 5 years).

Note:

The gain of the particular set of plates to be flown may not
be known sufficiently in advance of preamplifier delivery in
order to optimize the electronic gain at the preamplifier
level. Any changes in the required electronic gain will be
accomplished by adjusting the prescaling in front of the
A/D converters, therefore no bit budget is required to mathc
the particular plate set to the electronics.

Summary:

Baseline performance:	7 bits
ADC differential nonlinearity:	1 bit
MCP gain variations in flight:	1 bit
Dynamic Range of signal:	<5 bits
TOTAL	<14 bits

Conclusion:

1. The 14 bit ADC design being implemented in the HRC is
adequate, and includes adequate margin for forseeable preflight
and in-flight variations.

Comment: The above describes what is required to perform
adequately at the one pixel, or 6 micron level. It should be
noted that the imaging specification for the HRC is 25 microns
FWHM.

MEMORANDUM

To: File
From: J. Gomes
Subject: On-Board Test Pulse Generator
Date: 3/8/95

The HRC has an on board test pulse generator whose purpose is to
verify the gain, offset, and linearity of each channel of signal,
from the detector through to the point at which it becomes the
final digital data to be transmitted to the ground.

The test generator itself is operated using serial digital
commands for the on/off function, and to set the amplitude of the
pulses to any of 256 levels (8 bits). Serial digital commands
are also used to connect each amplification channel, in sequence,
to the on-board A/D converters.

The on-board pulse generator utilizes an D/A converter to set the
pulse amplitude required. It should be mentioned that drifts in
the absolute value of the pulse generator are of secondary
importance since the pulses applied to all channels experience
the same drift, and the position algorithm is amplitude
independent. What is important is ability to monitor the offsets
in each channel, which can cause image shifts at low signal
amplitudes, and gain differences among the channels, which can
cause image distortion.

The pulse generator is capable of producing output which can be
used to determine both gain and offset. The accuracy with which
this can be determined depends on the stability of the pulse
generator itself, which is an Analog Devices DAC-08, which has a
specified typical drift of 10 ppm/°C. Over the anticipated
temperature range of 25°C ± 25°C, the error for a typical device
would be ±250 ppm, which is the equivalent of 12 bit accuracy
(referred to full scale), or approximately 1:4000. During
instrument fabrication, DAC devices will be screened for low
temperature drift, and their outputs will be completely
characterized.

For proper imaging, the gain of a channel should be known to
better than 1%, or 1:100. Measurement of this parameter is
therefore not a problem with this system.

The offset of a channel can be determined by extrapolating the
data from many points toward the origin. It is expected that
this process would yield a result close to the 1:4000 mentioned
above. Since the offset specification for a channel is 1:667,
this method is expected to yield an accurate knowledge of this
parameter.

Offset Budget   JG 10/5/94

No matter what the gain is, we will set it to 20% of full scale.
This is from a science request to put the peak at channel 50 out
of 250.

A minimum signal for processing is then at about 20% of that peak
(from Almus Kenter, 10/5/94), or 4% of full scale.

Assume each of two adjacent amplifiers have essentially all of
the signal at 4% of full scale each, or 400mv each. The
denominator of the algorithm fraction is then 800mv.

The question is...how much numerator perturbance is required to
displace the event by a) one pixel, and b) to the CEI limit. The
numerator offset is due to 2 amplifiers, therefore the
perturbance voltage calculated will be twice the allowable offset
for a single amplifier channel.

or..

   For 1 pixel:

    2 X offset /800 = 1/256   (6.25 um)

       offset(max) = 800/(2*256) = 1.56 mv

   For CEI limit:

    2 X offset /800 = 4/256   (25 um)

       offset(max) = (800*4)/(2*256) = 6.25 mv

Given an overall budget of 1.5 mv, a reasonable assignment of the
error budget is as follows:

Hybrid preamplifiers .... 0.50 mv
Fast sample/hold .... 0.25 mv
S/H, ADC uncertainty *................ 0.25 mv
Contingency ....0.56 mv

* This uncertainty relates to offset only, and should not be
confused with round-off noise. In the minimum signal range, the
round-off noise has a peak to peak value of 0.61 mv per channel,
or 1.22 mv on the algorithm. This is less than one pixel.